Measuring and modelling soil erosion in agricultural systems: Evaluating the application of UAVs and SfM-MVS for soil erosion research

by

Benjamin U. Meinen

A thesis

presented to the University of Waterloo

in fulfilment of the

thesis requirement for the degree of

Doctor of Philosophy

in

Geography

Waterloo, Ontario, Canada, 2021

Examining Committee Membership

The following served on the Examining Committee for this thesis. The decision of the Examining Committee is by majority vote.

External Examiner: Dr. Todd Walter, Professor, Department of Biological and Environmental Engineering, Cornell

Supervisor: Dr. Derek T. Robinson, Associate Professor, Department of Geography and Environmental Management, University of Waterloo

Internal Member: Dr. Merrin Macrae, Professor, Department of Geography and Environmental Management, University of Waterloo

Internal Member: Dr. Richard Kelly, Professor and Chair, Department of Geography and Environmental Management, University of Waterloo

Internal-external Member: Dr. Nandita Basu, Associate Professor, Department of Earth and Environmental Sciences, University of Waterloo

Author's Declaration

This thesis consists of material all of which I authored or co-authored: see Statement of Contributions included in the thesis. This is a true copy of the thesis, including any required final revisions, as accepted by my examiners.

I understand that my thesis may be made electronically available to the public.

Statement of Contributions

This thesis has been structured according to the manuscript option. Chapters 2, 3, and 4 have been published in peer-reviewed journals. The chapters presented in this dissertation may have minor differences with their published counterparts due to edits for clarity. Since each published chapter represents a standalone work, there is some minor overlap in the materials and methods section of each chapter.

For all chapters in this dissertation, Benjamin U. Meinen was the lead author. Dr. Derek T. Robinson was the academic advisor for this thesis, and Benjamin U. Meinen and Dr. Derek T. Robinson collectively worked together on the conceptualization of each chapter, experimental design, and field research. Benjamin U. Meinen conducted all the data analysis, data curation, and wrote each chapter. Dr. Derek T. Robinson provided edits and proofed each chapter before publication. Specific author contributions are outlined in each peer-reviewed journal publication where applicable.

Chapter 2 is published as: Meinen, B. U., & Robinson, D. T. (2020). Mapping erosion and deposition in an agricultural landscape: Optimization of UAV image acquisition schemes for SfM-MVS. Remote Sensing of Environment, 239, 111666. Doi: 10.1016/j.rse.2020.111666

Chapter 3 is published as: Meinen, B. U., & Robinson, D. T. (2020). Where did the soil go? Quantifying one year of soil erosion on a steep tile-drained agricultural field. Science of The Total Environment, 729, 138320. Doi: 10.1016/j.scitotenv.2020.138320

Chapter 4 is published as: Meinen, B. U., & Robinson, D. T. (2021). Agricultural erosion modelling: Evaluating USLE and WEPP field-scale erosion estimates using UAV time-series data. Environmental Modelling & Software, 137, 104962. Doi: 10.1016/j.envsoft.2021.104962

Chapters 5 has not yet been submitted for review.

Chapter 6 has been accepted for publication in Environmental Modelling & Software.

Abstract

Soil erosion in agricultural systems is a pressing issue for agricultural sustainability. Accelerated rates of soil erosion from conventional agricultural practices continues to outpace the rate of natural soil regeneration, and the continued expansion of agriculture into highly erodible landscapes coupled with the threat of more intense precipitation events from a warming climate indicate that soil erosion will continue to be a serious environmental problem throughout the 21st century. While the processes driving soil erosion are well understood, the distributed and small-scale nature of erosional processes makes it difficult to quantify the severity of the erosion problem. Conventional measurement methodologies lack the spatial and temporal resolution to characterize soil erosion events at the farm-field scale. Our inability to accurately measure soil erosion events has resulted in soil erosion estimates being primarily based on modelling without field-based evidence to evaluate and validate modelling outcomes. To address this research gap, we explore a new state-of-the-art workflow for measuring distributed erosion processes using automated photogrammetric workflows (i.e., Structure-from-Motion Multi-View Stereo [SfM-MVS]) and optical imagery from an unmanned aerial vehicle (UAV). We experientially investigated the accuracy of the UAV SfM-MVS workflow for recreating the topography of an agricultural field using different aerial surveying techniques. Our results demonstrated that for a standard parallel-axis nadir UAV image acquisition, an RTK-GNSS ground control survey, a sufficiently dense deployment of ground control points, and the use of a self-calibrating bundle adjustment in an SfM-MVS software application, the vertical accuracy (RMSE) of pointclouds converges on 2–3× the ground-sampling-distance of the optical imagery with a practical upper limit of 0.01 m. Our nadir aerial surveys had ground-sampling-distances of between 0.011 – 0.018 m, which resulted in pointclouds with a range in vertical accuracies of 0.021 – 0.039 m. This vertical accuracy constrained our workflow to measuring deep rill erosion, ephemeral gully erosion, and depositional zones; small-scale sheet and rill erosion processes could not be directly measured with our presented workflow. Applying the UAV SfM-MVS workflow to an agricultural field in Ontario, Canada, we were able to measure semi-distributed soil erosion processes using down-slope depositional zones as a proxy for up-slope erosion processes. Over the course of one year, 159.52 t of sediment was deposited down-slope, corresponding to an erosion rate of 18.83 t ha^{-1} yr^{-1}; 86% of the total volume of eroded material was a result of intense storms during the corn growing season, with the majority of erosion associated with spring storms immediately following cultivation. During the winter months, despite the soil surface being barren after a moldboard plow, very little sediment was deposited down-slope. Soil erosion measurements collected using the UAV SfM-MVS workflow were then used to evaluate the predictions of the Universal Soil Loss

Equation (USLE) and Water Erosion Prediction Project (WEPP). Model evaluations demonstrated that the WEPP had more accurate short-term predictions (i.e., 1-year annual and sub-annual) for a year of corn production. Long-term modelling with the WEPP for our agricultural study site predicted an average of 6.4 days per year with soil erosion events and 14.1 days per year with runoff events. Winter events and snowmelt constituted 70% of the average long-term runoff but winter runoff events were rarely associated with soil loss, which matched our in-situ observations and measurements. To further explore the spatial variability in distributed erosion processes, we used a series of very-high resolution DEMs derived from the UAV SfM-MVS workflow and a simple hydrology model to explore the impact of microtopography on surface runoff. Modelling results demonstrated that the orientation of tillage lines, surface slope, and maximum depression storage, all had a statistically significant impact on surface runoff. Our agricultural study site was at the highest risk of surface runoff and soil loss in the spring immediately following cultivation since the smoothed soil surface facilitated a high degree of landscape connectivity. Based on these results, we used our experiential knowledge of field-scale hydrology and erosion processes to additionally explore an up-scaled model implementation of the USLE for the entire watershed in which our agricultural study site was situated. We evaluated how different model user's design choices and spatial conceptualizations of an agricultural systems affect predictions of soil erosion. We found a high degree of variability in soil erosion estimates at the watershed-scale, e.g., changing the implementation of a single USLE factor led to a range in model outcomes from 3.04 to 11.02 t ha^{-1} yr^{-1}. This variability exemplifies the uncertainty associated with watershed-scale implementations of erosion models in the absence of a standardized and accredited model setup.

Acknowledgements

I would like to acknowledge first and foremost, my advisor, Dr. Derek T. Robinson, since I would never have completed my PhD without him. Thanks for giving me the opportunity to complete graduate school with you as my supervisor and providing me with the opportunity to work on numerous different projects throughout my time here. Thanks for the feedback, edits, comments, and critiques on all my chapters. Thanks for always having confidence in me and for giving me the skillset I needed to excel in graduate school.

I would like to thank my committee members: Dr. Merrin Macrae, Dr. Richard Kelly, and Dr. Nandita Basu for taking the time to read over my dissertation and critiquing my work.

Thanks to my fellow lab members: Collin Branton, Bo Sun, Tanya Iljas, Alex Smith, Jenny Ridge, Erin Menzies Pluer and Omar Dzinic. A special thanks to Omar Dzinic for helping me with field work, data processing, and answering all my GIS questions; on the non-academic side of things, thanks for the countless squash matches and for the annual visit to the UW gym.

Thanks to our farming partners for allowing us access to their farm for conducting two years of field research.

I would also like to thank Rachel Meinen, my loving wife, for supporting me through my 4-years of graduate school. Thanks for listening to me talk about my dissertation and for reading over my chapters after I insisted they were interesting and worth a read. Thanks for always believing in me and the support you gave me through all these years.

Table of Contents

List of Figures

List of Tables

List of abbreviations

Abbreviation	Term
AGL	Above-ground-level
BA	Bundle adjustment
DEM	Digital elevation model
GCP	Ground control point
GSD	Ground-sampling-distance
GIS	Geographic information system
NSE	Nash-Sutcliffe efficiency
RPAS	Remotely piloted aircraft system
RTK-GNSS	Real-time Kinematic Global Navigation Satellite System
SDR	Sediment delivery ratio
SfM-MVS	Structure-from-Motion Multi-view Stereo
TLS	Terrestrial laser scanner
UAV	Unmanned aerial vehicle
USLE	Universal Soil Loss Equation
WEPP	Water Erosion Prediction Project

Chapter 1. Introduction

Soil erosion, the detachment and transport of the upper layer of soil, is a natural process that has been accelerated by agricultural land management activities. Conventional agricultural practices (e.g., moldboard plowing) can result in soil erosion rates up to an order of magnitude greater than the rate of natural soil regeneration (Montgomery 2007) and is one of the leading causes of soil degradation in agricultural systems (FAO 2015; Montanarella 2015). Nutrient-rich topsoil eroded from agricultural fields negatively impacts on-site productivity (den Biggelaar et al. 2001) and is responsible for a number of off-site water quality issues such as sedimentation of waterways (Holmes 1988), increased turbidity (Henley et al. 2000), hypoxia (Ryan 1991), and eutrophication (Michalak et al. 2013). Long term trends in agriculture of increased fertilizer use (500% increase in 50 years; Foley et al. 2011), agricultural expansion into highly erodible landscapes (e.g., forested tropics; Foley et al. 2011), and an increasing demand for agricultural goods (Tilman et al. 2011), coupled with long term climatic trends (i.e., more intense precipitation events; Groisman et al. 2005) could be a harbinger of future environmental problems from agricultural soil erosion.

In an effort to ameliorate the impacts of agricultural soil erosion, erosion models have been developed to formalize and improve upon our understanding of how different natural processes and land management activities can exacerbate or mitigate soil erosion. Since the seminal publication of the first widely used erosion model, the Universal Soil Loss Equation (USLE; Wischmeier and Smith 1978), a large suite of erosion models have been developed: Erosion-Productivity Impact Calculator (EPIC; Williams 1989), Water Erosion Prediction Project (WEPP; Laflen et al. 1991), Soil and Water Assessment Tool (SWAT; Arnold 1994), Limburg Soil Erosion Model (LISEM; De Roo et al. 1996), Revised USLE (RUSLE; Renard et al. 1997), European Soil Erosion Model (EUROSEM; Morgan et al. 1998), among many others. While many of these models have been successfully applied to different agricultural systems, modelling the process of soil erosion across different geographic and social domains is difficult (Boardman 2006) and erosion models often fail to reproduce the hydrologic and sedimentologic response of the system they are modelling.

The challenges in modelling soil erosion are due to the complexity and variability of human-natural systems; soil erosion in agricultural systems is a function of human-decision making (e.g., soil compaction, tillage), land use (e.g., crop type), soil properties (e.g., hydraulic conductivity), climate (e.g., rainfall intensity), and topography (e.g., slope). Adding to this complexity is the stochastic nature of environmental processes; seemingly identical agricultural systems can have vastly different hydrologic responses and rates of soil erosion (Wendt et al.

1986; Nearing et al. 1999), indicating that there is a practical upper limit on the accuracy of a deterministic erosion model. Since the input variables needed to parameterize soil erosion models can be difficult to measure and due to the inherent stochastic nature of environmental processes, field-based evidence needs to be coalesced with erosion models to ensure the models are behavioral and for validating model outcomes.

Small-scale distributed measurements of the three most common process domains, i.e., sheet (also known as interrill), rill, and ephemeral gully erosion, are necessary for validating the outcomes of an erosion model. Despite a wide range of tools available for measuring distributed rates of soil erosion such as isotopic tracer methods (e.g., ceasium-137; Walling et al. 2003), field-based methods (e.g., measuring rills and gullies; Takken et al. 1999), or proxies for erosion (e.g., sediment yield; Borrelli et al. 2014), there is a considerable amount of uncertainty associated with each technique (Stroosnijder 2005), and each method is constrained by either spatial scale, accuracy, or repeatability of measurements. The needed outcomes of achieving a cost-effective measurement technique at the farm-field scale has not yet been attained, and accurate measurements of soil erosion have been constrained to the plot scale.

The lack of tools for measuring distributed soil erosion, and the challenges with existing tools, has resulted in most soil-erosion-modelling studies being conducted in the absence of a formal model evaluation (Jetten et al. 2003; Morgan and Nearing 2011). In the absence of these distributed soil erosion measurements, models are typically evaluated against the outlet response of a system (e.g., basin or watershed outlet), which can often lead to an incorrect representation of the internal dynamics of the system. As a general trend, process-based erosion and hydrology models have become increasingly complex and the large number of degrees of freedom associated with these models have led to issues with equifinality (Beven, 2006). This problem is exemplified in the erosion modelling literature when sediment yield data is used for model evaluations, i.e., an evaluation dataset that cannot determine if the model is behavioral in the system it is modelling (agricultural fields). Field-scale measurements of soil erosion are required to combat challenges of equifinality and evaluate modelling results.

The democratization of unmanned aerial vehicles (UAVs; also known as remotely piloted aircraft systems [RPAS]) and automated photogrammetric workflows (i.e., Structure-from-Motion Multi-view Stereo [SfM-MVS]) herald a new advancement in remote sensing technology for measuring distributed soil erosion rates. While field-scale studies using UAVs to quantify agricultural erosion are few, the UAV SfM-MVS workflow has been used to quantify gully erosion (e.g., d'Oleire-Oltmanns et al. 2012), rill erosion (e.g., Eltner et al. 2015), and other distributed

erosion processes (e.g., gorge erosion; Cook 2017). While other remote sensing platforms such as airborne LiDAR, satellites, and mid-altitude aerial photography have a sufficient spatial resolution for observing the consequences of erosion, mass movements, and gully erosion (e.g., Quickbird; Desprats et al. 2013), they lack the spatial and temporal resolution to characterize or quantify soil erosion on individual agricultural fields (Fig 1.1). UAV platforms have the potential to allow for new insights into field-scale erosion research, since they have a sufficient resolution for qualitatively identifying all erosional landforms and have the potential to quantitatively map small-scale erosion processes (e.g., Pineux et al. 2017). The application of UAV technology has emerged in the remote sensing literature over the past decade, but the UAV SfM-MVS workflow has yet to be used for measuring field-scale erosion processes, testing erosion models (Batista et al. 2019), or for parameterizing erosion models (e.g., very-high resolution DEMs).

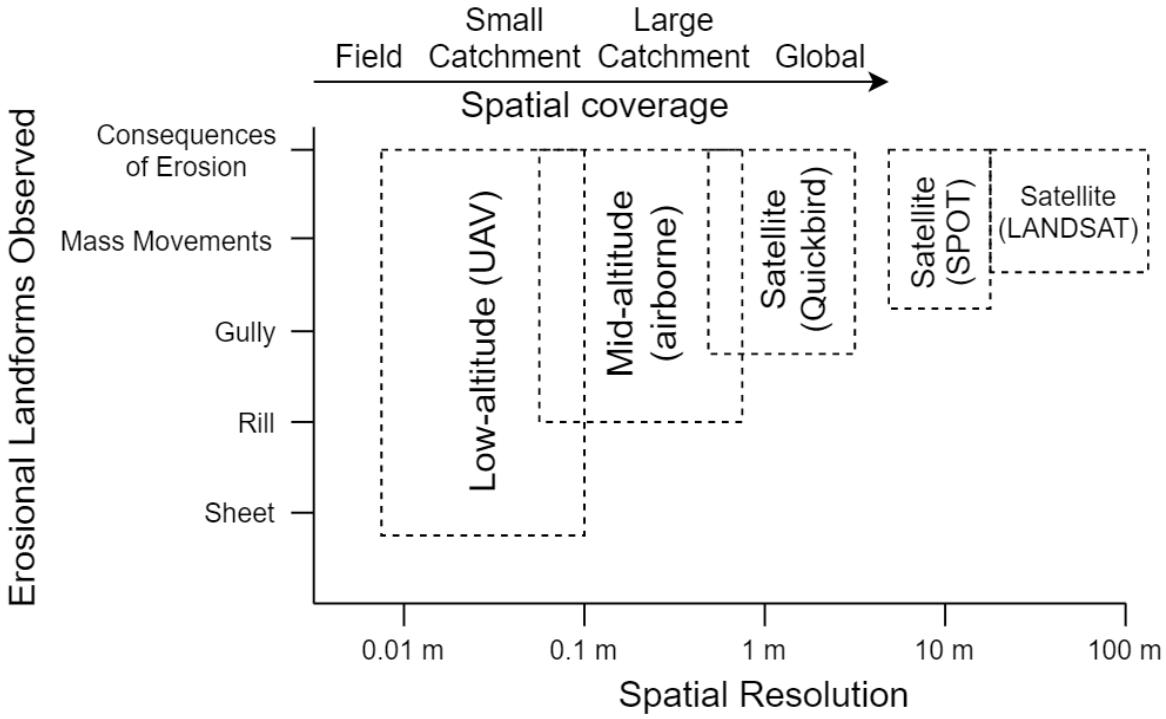

Fig. 1.1. Application of UAVs for soil erosion research.

1.1. Research Objectives and Thesis Organization

A research gap exists in the agricultural erosion modelling literature, not in the development of new erosion models, but in the evaluation of existing models, and the application of new UAV remote sensing techniques for agricultural soil erosion research. To address this research gap, this thesis has five research objectives:

(1) Experientially investigate the accuracy of using the UAV SfM-MVS workflow for modelling surface change-detection in an agricultural system.

(2) Demonstrate the application of the UAV SfM-MVS workflow for measuring distributed soil erosion rates at the farm-field scale.

(3) Evaluate the soil erosion predictions of the Universal Soil Loss Equation (USLE) and Water Erosion Prediction Project (WEPP) using semi-distributed soil erosion measurements at the farm-field scale.

(4) Quantify the effects that microtopography has on surface runoff and landscape connectivity using very-high resolution DEMs.

(5) Conduct a critical review on how model user's design choices and spatial conceptualizations of an agricultural system influence variability in model outcomes.

To meet the five outlined research objectives, this thesis is organized into seven chapters. Chapters 2 – 4 are a comprehensive evaluation on the UAV SfM-MVS workflow on an agricultural study site and fulfill Research Objectives 1, 2, and 3. Chapters 5 and 6 fulfill Research Objectives 4 and 5, respectively, and focus on a more general outlook on erosion modelling in agricultural systems.

To experientially investigate the accuracy of the UAV SfM-MVS workflow, Chapter 2 focusses on the effects that UAV image orientation has on the accuracy of camera self-calibration. We tested four different UAV image acquisition schemes that incorporated both nadir and oblique imagery of a 15.9-ha agricultural field: 26 nadir imaging strips [N], 13 east-facing oblique +13 west-facing oblique imaging strips (i.e., convergent imaging scheme [C]), 26 nadir +5 east-facing oblique +5 west-facing oblique imaging strips [NC_5], and 4) 26 nadir +26 east-facing oblique +26 west-facing oblique imaging strips [NC_{26}]. To quantify the accuracy of camera self-calibration for each image acquisition scheme, we calculated the checkpoint accuracy of control points that were not used in the calibration. The accuracy of each checkpoint provided a metric indicative of the overall quality of the resultant pointcloud. We conducted a total of four tests per field campaign on each of the four image sets by incorporating a different number of GCPs into the self-calibrating bundle adjustment: 1) No GCPs, 2) 13 normative GCPs, 3) 17 normative GCPs, and 4) 21 normative GCPs.

Chapter 3 expands on the experiential knowledge gained from Chapter 2 and provides a comprehensive evaluation of the UAV SfM-MVS workflow using the most reliable image

acquisition scheme selected from Chapter 2. The accuracy of each UAV image acquisition scheme was evaluated for a variety of different ground control surveys, ground-sampling-distances, and field conditions. Based on these metrics, we determined the minimum level of change-detection possible with the UAV SfM-MVS workflow and used this workflow to measure the annual distributed erosion rate of our agricultural study site.

Chapter 4 uses the erosion dataset collected in Chapter 3 to evaluate the annual and sub-annual erosion predictions of the Universal Soil Loss Equation (USLE) and Water Erosion Prediction Project (WEPP). Using a semi-distributed approach, we compared the predictions of the USLE and WEPP to the measured erosion rate of six unique basins on our agricultural study site. The erosion model that performed better at the sub-annual scale was used to evaluate how a shift in long term management practices, i.e., types of tillage, could ameliorate accelerated rates of soil erosion, and to gain insights into the long-term temporal distribution of erosion and runoff events.

Chapter 5 uses the very-high resolution DEMs created with the UAV SfM-MVS workflow in Chapter 3 to conduct a case study on field-scale hydrology, with an emphasis on how the partitioning of rainfall can be used to differentiate between soil erosion and soil loss. We focussed on the relationship between modelled surface runoff values and three factors that describe the microtopography of the landscape (i.e., random roughness, slope, maximum depression storage), two land management practices that influence the spatial variability of microtopography (i.e., tillage orientation, tillage implements), and two environmental variables (i.e., storm intensity, antecedent moisture conditions). We calculated surface runoff across 144 plot-scale and 18 hillslope-scale hydrology simulations using a simple fully distributed hydrology model. Surface runoff values were compared across hydrology simulations to look for patterns and trends in the partitioning of rainfall across each surface.

Chapter 6 provides a generalized outlook on the current state of erosion modelling literature with a focus on critiquing applications of the de-facto standard for erosion modelling, the USLE. While the USLE has a strong empirical basis, extending the USLE outside of its intended design space, i.e., predicting soil loss from planar hillslopes, to predicting distributed soil erosion rates at large spatial extents introduces uncertainty in model outcomes. Since there is no standardized and accredited setup for up-scaling the USLE in space and time, model users implement a wide variety of different methodologies for model up-scaling. Each design choice for up-scaling the USLE comes with an implicit set of assumptions and simplifications. Chapter 6 uses a watershed-scale case study to demonstrate the uncertainty associated with a variety of

different design choices for up-scaling the USLE by comparing the variability in soil erosion rates across each modelling approach.

Chapter 7 is a synthesis of the findings of this dissertation, providing concluding remarks and future research directions for agricultural soil erosion research.

Chapter 2. Mapping erosion and deposition in an agricultural landscape: Optimization of UAV image acquisition schemes for SfM-MVS

As published in Remote Sensing of Environment: Meinen, B. U., & Robinson, D. T. (2020). Mapping erosion and deposition in an agricultural landscape: Optimization of UAV image acquisition schemes for SfM-MVS. Remote Sensing of Environment, 239, 111666. Doi: 10.1016/j.rse.2020.111666

2.1. Introduction

Structure-from-Motion (SfM) is a photogrammetric technique used to generate a 3D pointcloud from a collection of overlapping 2D images (Carrivick et al., 2016). The SfM process starts with feature detection, which involves identifying unique features on an image (e.g., using scale-invariant feature transform; Lowe, 2004) and matching homologous features (i.e., keypoints) across overlapping images to generate image correspondences. Given a set of corresponding features, 3D coordinates of matched features (i.e., a sparse pointcloud) can be generated using an iterative bundle adjustment (BA). The BA is a least-squares optimization that simultaneously estimates the 3D positions of a scene and camera poses (Eltner et al., 2016; Triggs et al., 2000). The camera's intrinsic parameters can be included as an unknown in the BA (i.e., a self-calibrating BA). Following the BA, a Multi-view Stereo (MVS) algorithm is then used to generate additional points to create a dense pointcloud; the entire workflow is referred to as SfM-MVS (Smith et al., 2016).

The geosciences have been adopting the SfM-MVS workflow to model complex landscapes using images collected from terrestrial (e.g., Stumpf et al., 2015) and airborne platforms (e.g., unmanned aerial vehicles [UAVs]; Meinen and Robinson, 2020a). Applications of UAV SfM-MVS include monitoring landslides (e.g., Turner et al., 2015; Lucieer et al., 2014a; Niethammer et al., 2012), quantifying soil erosion (e.g., d'Oleire-Oltmanns et al., 2012; Eltner et al., 2013; Peter et al., 2014; Stöcker et al., 2015; Pineux et al., 2017), mapping snow depth (e.g., Nolan et al., 2015; Harder et al., 2016), and monitoring glacial dynamics (e.g., Bash et al., 2018; Immerzeel et al., 2014; Ryan et al., 2015). Study scales range from close-range UAV photography used to generate sub-cm spatial resolutions (e.g., flying height of 8–10 m; Eltner et al., 2013) to high-altitude UAV flights generating decimeter-level spatial resolutions (e.g., flying height of 500 m; d'Oleire-Oltmanns et al., 2012).

Since each study utilizing UAV SfM-MVS differs in its spatial scale and intended application, it can be difficult to infer what the best practices are for UAV survey design in different

landscapes. One commonality among UAV SfM-MVS surveys is the method used for camera calibration. Pre-calibration of cameras (e.g., using an independent image set to derive camera intrinsics) is rarely used in most geoscience research and instead a self-calibrating BA is most frequently used. When using a self-calibrating BA, the UAV survey design should reflect this choice; UAV surveys that are composed of exclusively parallel-axis nadir imagery can lead to an incorrect camera model (e.g., incorrect radial distortion terms; Harwin et al., 2015; James and Robson, 2014). If the self-calibration fails to accurately calculate radial distortion terms the resultant 3D model may have a high degree of surface deformation, exhibiting a doming effect (James and Robson, 2014). Despite SfM being most effective with images taken from a variety of locations and perspectives, typical UAV surveys only capture imagery from one perspective (i.e., nadir). The inclusion of oblique imagery and a strong network of ground control points (GCPs) should lead to a more accurate self-calibration.

A cross comparison of accuracy results among existing UAV SfM-MVS surface models in the literature is difficult. Most UAV surveys use nadir-only imagery and do not report the image orientation or incorporate oblique imagery into their survey. Reported accuracies vary widely in horizontal and vertical directions (from centimeters to decimeters) and are difficult to compare due to a lack of standard reporting protocol. For example, literature may report only GCP error metrics (e.g., d'Oleire-Oltmanns et al., 2012), checkpoint error metrics (e.g., Tamminga et al., 2015), comparison with a terrestrial laser scanner (e.g., Eltner et al., 2015), GCP/checkpoint error metrics and evaluation of invariant topography (Lucieer et al., 2014a), or GCP error metrics and comparison with LiDAR (Cook, 2017). The lack of standard reporting protocol for SfM-MVS accuracy assessments and unique challenges associated with modelling different landscapes necessitates an independent evaluation of UAV survey designs for different landscapes.

Agricultural landscapes (i.e., croplands and pastures) constitute the dominant land-use on Earth's surface (i.e., 38%; Foley et al., 2011) but no farm field-scale scale (i.e., >1 ha) accuracy assessments of agricultural SfM-MVS exist; existing UAV surveys are either plot-scale (e.g., Eltner et al., 2013; Stöcker et al., 2015) or have no rigorous accuracy assessment (e.g., d'Oleire-Oltmanns et al., 2012; Peter et al., 2014; Pineux et al., 2017). Agricultural landscapes present a unique challenge for the SfM-MVS workflow due to homogeneous soil textures, vegetation, and minimal variations in topographic relief. To identify the optimal survey design for a self-calibrating BA for agricultural landscapes, we assessed the accuracy of 3D surface reconstructions of a 15.9-hectare field using four different image acquisition schemes: nadir, oblique, and two different combinations of nadir and oblique. We used our 3D surface reconstructions to answer two

questions: 1) when using a self-calibrating BA, does the addition of oblique imagery improve the relative accuracy of 3D surface models: a) in the absence of ground control points (GCPs), and b) with a normative distribution of GCPs (i.e., capturing edges and having a comprehensive spatial coverage), and 2) how accurately can sequential UAV surveys detect small-scale erosional processes relative to terrestrial laser scanning? To answer these questions, three field campaigns were conducted over the course of one month. Each campaign consisted of three UAV flights over an agricultural field using parallel-axis flight lines to capture: nadir imagery, west-facing oblique imagery, and east-facing oblique imagery. Ground truth data for accuracy assessments were taken from a network of 27 GCPs.

2.2. Study site

Our study site is located in the upper-Nith river basin in southwestern Ontario. The Nith River is a tributary to the Grand River, which flows into the northern basin of Lake Erie, draining an area of 1130 km^2. The upper-Nith river basin has a mosaic of land cover comprising 84% agriculture, 6% forest, 6% wetland, and 4% urban cover (Loomer and Cooke, 2011). This predominantly agricultural basin is geologically composed of silty tills with an extensive tile-drainage network (Loomer and Cooke, 2011). The combination of agricultural land use and silty tills along the upper-Nith River contribute a large amount of suspended sediments and phosphorus into the Nith River. Water quality issues are kept in check partly by the Waterloo Moraine in the lower-Nith basin, but the Nith basin is one of the top contributors of sediments to the Grand River (Loomer and Cooke, 2011).

The study site is a 15.9 ha (~40 acre) agricultural field bordering on the south side of the Nith River. The field is a mosaic of landform elements and topographic variation; the southern portion is relatively homogeneous and flat whereas the northern portion is characterized by steep slopes descending into a forested riparian zone (Fig. 2.1). Subsurface tile drainage was installed prior to the initial survey with soil berms and surface inlets (i.e., catch basins) installed at six locations to prevent overland flow from directly draining into the Nith River.

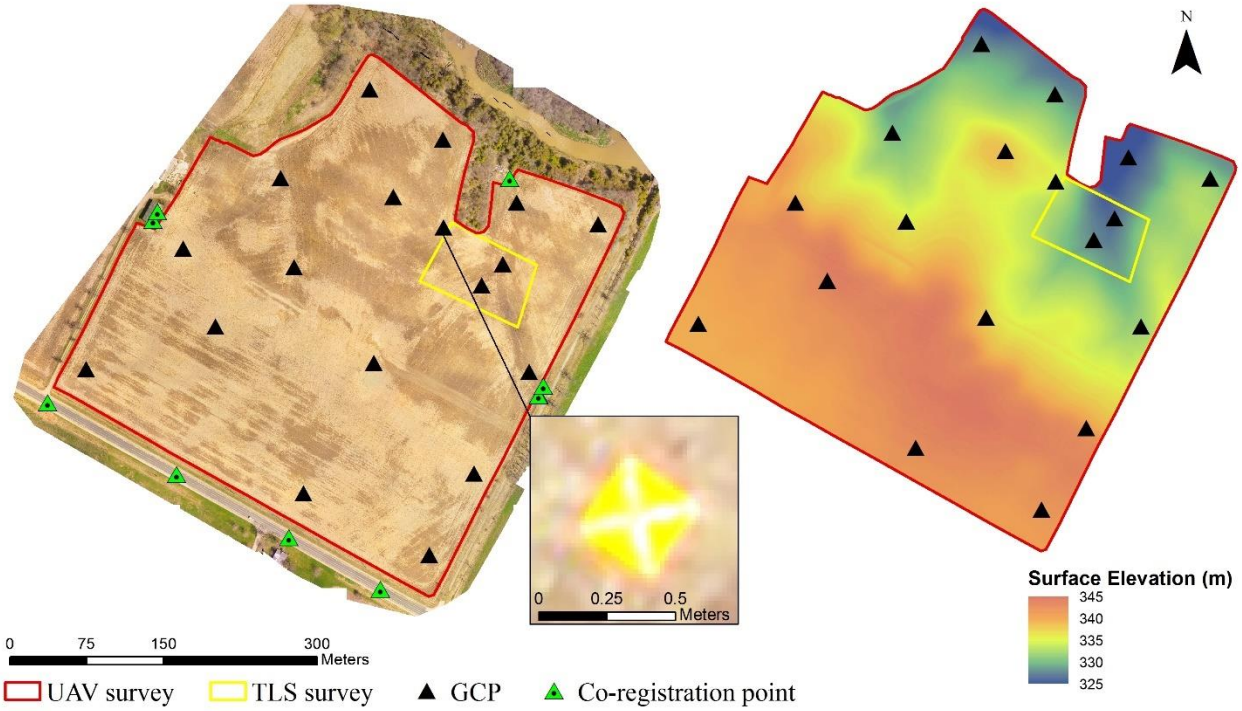

Fig. 2.1. Orthomosaic of the study site captured by the UAV (left), a ground control point (GCP) as visualized in the aerial imagery (center), and surface elevation in meters above-sea-level (ASL) (right).

2.3. Materials and methods

A FLIR Systems R60 SkyRanger UAV was used to collect aerial imagery (Fig. 2.2a). The R60 Skyranger is a vertical take-off and landing quadcopter weighing 2.8 kg with 40 min flight times. FLIR Systems Mission Control Station (MCS) software is used to automate parallel-axis flight lines across the field. The SR-3SHD payload was used for image acquisitions which acquires 15 MP RGB 4608 × 3288 resolution images (.jpg file format). The SR-3SHD has a 3-axis gimbal that compensates for the yaw, pitch, and roll of the UAV. The payload has a field of view of 46 degrees, 7.5 mm focal length, 6.45 × 4.60 mm sensor, and uses a rolling shutter. The UAV is equipped with a GPS receiver which geotags acquired images.

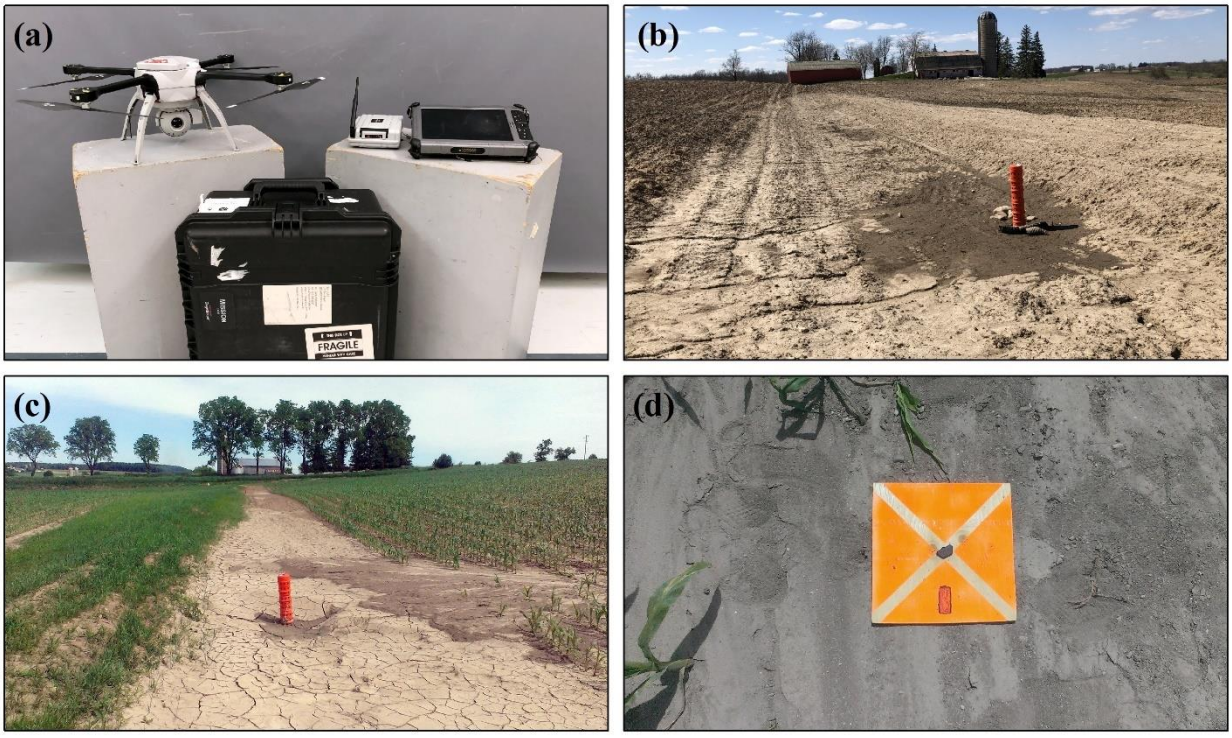

Fig. 2.2. (a) Skyranger UAV system with tablet and base station, (b) south-west surface inlet and catch basin (May 7, Campaign 1; image facing west), (c) sediment plume approaching the south-east surface inlet and catch basin (June 15, Campaign 3; image facing east), (d) ground control point.

A total of 18 ground control points (GCPs; Fig. 2.1) were distributed across the study site. GCPs were placed to capture the image edges, slopes, and the topographic highs and lows. The GCPs were 12 × 12 in. plywood squares painted fluorescent orange with a distinctive “X” pattern. Each GCP had a small hole in the center where a twelve-inch plastic tent peg was driven into the ground to secure the plywood square to the ground. GCPs were measured using SmartNet's network Real-time Kinematic Global Navigation Satellite System (RTK-GNSS) with a Leica Viva GS14 and Leica Viva CS15 field controller. The network RTK produced an average accuracy of 0.01 m horizontally and 0.02 m vertically. An additional 9 ground controls were located outside the study area and were used as invariant co-registration control points. These co-registration points were stable features (e.g., painted roadway lines) that were invariant during the study period.

Three field campaigns were conducted on May 7 (Campaign 1), May 17 (Campaign 2), and June 15 (Campaign 3). The study site was tilled on May 12, which enabled us to compare the field pre and post tillage. Several rainstorms occurred between Campaign 2 and Campaign 3, allowing us to demonstrate the viability of UAV SfM-MVS in detecting small-scale erosional

processes. For each field campaign, 18 GCPs were distributed across the field (Fig. 2.1) and removed after the UAV flights. The 9 co-registration control points were measured once during Campaign 1 and incorporated into each subsequent survey to co-register surface models. Each field campaign consisted of three UAV flights with three different camera orientations: 1) nadir, 2) east-facing oblique, and 3) west-facing oblique. Flights were flown at 90 m above-ground-level and had parallel-axis flight lines with a 70% frontlap and sidelap and a ground-sampling-distance of 0.017 m. The UAV was flown at approximately 4 m s^{-1}. All oblique photos were taken at a 15-degree angle relative to nadir. Flights covered an area of 24 ha to ensure the entire field was captured during each campaign. A Leica Multistation MS50 (a terrestrial laser scanner; TLS) was simultaneously used to scan a small sub-section of the field (indicated in yellow on Fig. 2.1) to quantify the accuracy of UAV-based surface change-detection.

2.3.1. SfM-MVS surface processing

To determine if the addition of oblique imagery improved the relative accuracy of 3D surface models, we generated four surface models based on four different image sets (Fig. 2.3): 1) 26 nadir imaging strips [N], 2) 13 east-facing oblique +13 west-facing oblique imaging strips (i.e., convergent imaging scheme [C]), 3) 26 nadir +5 east-facing oblique +5 west-facing oblique imaging strips [NC_5], and 4) 26 nadir +26 east-facing oblique +26 west-facing oblique imaging strips [NC_{26}], which comprised all data collected during a single field campaign. The [N] image set had a uniform 70% overlap between images, while the [C], [NC_5], and [NC_{26}] image sets had variable levels of image overlap.

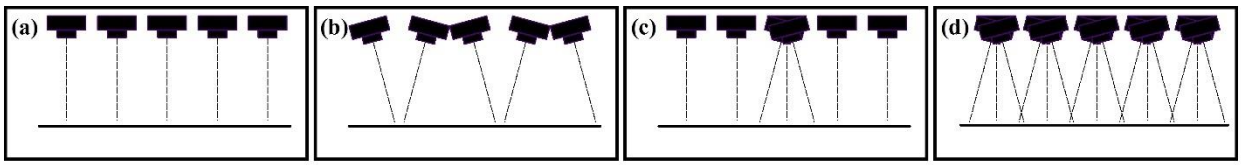

Fig. 2.3. Orientation of camera poses for each image set: (a) 26 nadir imaging strips [N], (b) 13 east-facing oblique +13 west-facing oblique imaging strips [C], (c) 26 nadir +5 east-facing oblique +5 west-facing oblique imaging strips [NC_5], (d) 26 nadir +26 east-facing oblique +26 west-facing oblique imaging strips [NC_{26}]. Dotted lines indicate image center.

Pointcloud surface models were created for each of the four image sets using Pix4D (Pix4D SA, Switzerland; Table 2.1). Image geolocation from the UAV GPS receiver was used to initially locate all the images and to speed up processing time. Overexposed and blurry images were removed before processing. Processing options for each surface were: keypoint image scale of 1, automatic targeted number of keypoints, standard calibration method, and all camera optimizations. Pointcloud densification was conducted using: optimal point density (i.e.,

computing a 3D point for every 4 pixels), full image scale (i.e., original image size is used to compute additional 3D points), and with 3D points only being generated if they were correctly re-projected in at least 4 images. All GCPs and co-registration points (i.e., 27 GCPs) were used in a self-calibrating BA. If any surface had its average root-mean-square-error exceed 0.010 m for the GCPs, the project was checked for GCP marking error and reprocessed. The data were processed on a Dell Precision Workstation 5810 Tower with Intel Xeon CPU E5-1620 v3 @ 3.5 GHz with quad-core, 64 GB RAM, 8 processors, NVIDIA Quadro K4200 graphics card, and operating on Windows 7 64-bit (Fig. 2.4).

Table 2.1. Processing results from four image sets averaged across three campaigns. Camera self-calibration results for Campaign 1 (P_x, P_y are the [x,y] principal points; R_1, R_2, R_3 are radial distortion coefficients; T_1, T_2 are tangential distortion coefficients).

Processing Results (All Campaigns):	[N]	[C]	[NC_5]	[NC_{26}]
Number of Images	530	503	679	1545
GCP $RMSE_X$ [m]	0.009	0.008	0.009	0.009
GCP $RMSE_Y$ [m]	0.008	0.006	0.007	0.007
GCP $RMSE_Z$ [m]	0.008	0.010	0.008	0.008
Densification Processing Time	4h 11m	4h 13m	7h 09m	20h 56m
Generated Points (million)	189	178	216	391
Camera Self-calibration (Campaign 1) :				
Focal Length (mm)	7.59	7.58	7.60	7.58
Principal Point (P_x) (mm)	3.43	3.44	3.44	3.44
Principal Point (P_y) (mm)	2.24	2.24	2.23	2.24
R_1	-0.100	-0.101	-0.100	-0.100
R_2	0.071	0.083	0.074	0.077
R_3	0.068	0.036	0.061	0.058
T_1	-0.001	-0.001	-0.001	-0.001
T_2	-0.001	-0.001	-0.001	-0.001

Pix4D Camera Model:

$$\begin{pmatrix} x_{hd} \\ y_{hd} \end{pmatrix} = \begin{pmatrix} (1 + R_1 r^2 + R_2 r^4 + R_3 r^6) x_h + 2T_1 x_h y_h + T_2 \, (r^2 + 2(x_h)^2) \\ (1 + R_1 r^2 + R_2 r^4 + R_3 r^6) y_h + 2T_2 x_h y_h + T_1 \, (r^2 + 2(y_h)^2) \end{pmatrix}$$

Fig. 2.4. 3D rendering of pointclouds centered on the north-east surface inlet and catch basin: (a) Campaign 1, (b) Campaign 2, and (c) Campaign 3. Illumination conditions were bright for Campaign 2 and 3.

2.3.2. SfM-MVS surface processing for accuracy assessments

To identify the optimal survey design for use with a self-calibrating bundle adjustment (BA), we conducted a total of four tests per field campaign on each image set by incorporating a different number of GCPs in the BA: 1) No GCPs, 2) 13 normative GCPs, 3) 17 normative GCPs, and 4) 21 normative GCPs. For each test, the 9 co-registration points were always used, and supplemented by 4, 8, and 12 of our distributed GCPs respectively. The surfaces generated without GCPs were later georeferenced using all 27 GCPs in CloudCompare (https://www.danielgm.net/cc/) with the align tool using a fixed scale. All GCPs not used in the BA were used as checkpoints to calculate surface error metrics, expressed as absolute vertical and horizontal checkpoint error.

2.3.3. Surface model co-registration procedure for change-detection

Since each pointcloud was processed independently with a unique set of GCPs, small measurement errors (i.e., ±0.02 m vertically) led to vertical misalignments between subsequent pointclouds. To ensure an effective co-registration of surface models we applied an additional alignment technique (for change-detection calculations only). We iteratively edited GCP elevation values (±0.02 m maximum change; i.e., same vertical error as RTK-GNSS) and recreated surface models that minimized change in areas of invariant topography (e.g., roadways, edge of field) and areas that exhibited obvious surface deformation (i.e., doming). As the self-calibration ties the surface model closely to GCPs, it is more logical to edit GCPs within the threshold of their accuracy rather than do a global translation after the surface has been processed. A global translation, while potentially enabling an effective co-registration, can also shift areas of topography that are correctly reconstructed (see Table 2.2 results). While our approach was both computationally intensive and time consuming, it mitigated deformation in the surface models, allowing for a higher confidence in the accuracy of the change-detection procedures.

2.3.4. Change-detection calculation

Change-detection is most commonly calculated by DEM differencing. While efficient, DEM differencing can only be performed on gridded meshes on a per pixel-basis (i.e., not on pointclouds). Another common technique involves using cloud-to-cloud (C2C) distances, which is a computationally efficient algorithm that calculates the nearest-neighbor distance between point-pairs, but is not always indicative of the true distance between clouds, most notably for low density and noisy clouds. A novel change-detection procedure, the M3C2 algorithm (Lague et al., 2013), offers a more robust change-detection procedure that can be used directly on pointclouds. The M3C2 algorithm calculates a normal vector for each point and fits a cylinder of a specified radius in the direction of the normal vector. Surface change is calculated as the average distance between the two pointclouds in the cylinder, making the M3C2 algorithm less sensitive to surface noise. For a more precise calculation of volumetric change, we used M3C2 distance calculations with vertical normals and a 0.15 m diameter projection.

The M3C2 algorithm was used to compute change-detection results for UAV SfM-MVS surface models between Campaigns 1 and 2, and between Campaigns 2 and 3. To verify the accuracy of our change-detection calculations, UAV-derived change detection results were compared against TLS change-detection results at the north-east surface inlet of our study site.

2.4. Results

2.4.1. Surface model accuracy assessments

Four surface models were generated from our four images sets ([N], [C], [NC_5], and [NC_{26}]) without using any GCPs in the bundle adjustment (BA). These four surface models had their vertical accuracies assessed by a comparison to the [N] surface model processed with all 27 GCPs for Campaign 1 (Fig. 2.5). The [N] surface model generated without GCPs had a characteristic surface doming (Fig. 2.5a) as is commonly seen with nadir-only image sets. The [C] surface model had a complex pattern of error, with error propagating from two radial centers (Fig. 2.5b). The two other surface models processed without GCPs (i.e., [NC_5] and [NC_{26}]) had lower overall surface error thanks to the coupling of nadir and oblique imagery but contained a different distribution of error; both surface models had a “half-pipe” effect (Fig. 2.5c and d), with negative error towards the east/west edges of the surface and positive error along the centerline of the model.

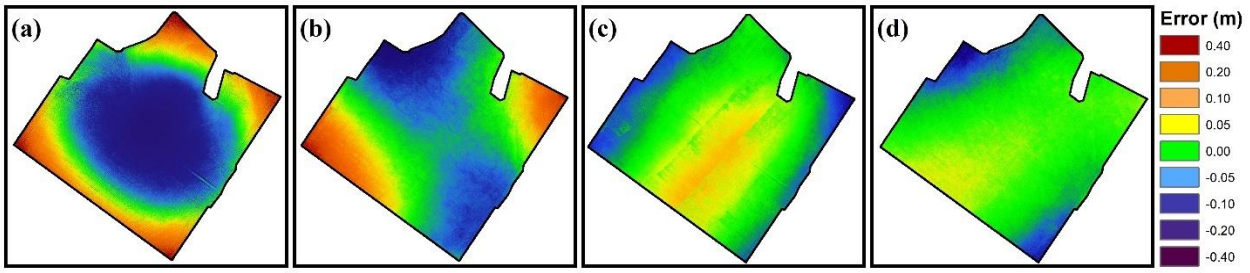

Fig. 2.5. Distribution of vertical surface error for each image set processed without GCPs for Campaign 1: (a) 26 nadir imaging strips [N] (RMSE 0.150 m), (b) 13 east-facing oblique +13 west-facing oblique imaging strips [C] (RMSE 0.099 m), (c) 26 nadir +5 east-facing oblique +5 west-facing oblique imaging strips [NC_5] (RMSE 0.049 m), (d) 26 nadir +26 east-facing oblique +26 west-facing oblique imaging strips [NC_{26}] (RMSE 0.041 m).

When GCPs were not incorporated into the BA, the [NC_{26}] image set produced the most accurate surface models across all field campaigns (checkpoint error; vertical RMSE: 0.047 m, horizontal RMSE: 0.019 m), with the [NC_5] image set following closely behind (vertical RMSE: 0.061 m, horizontal RMSE: 0.025 m). Due to the large amounts of radial doming in the [N] surface models, all [N] surfaces had poor vertical and horizontal accuracies (vertical RMSE: 0.151 m, horizontal RMSE: 0.226 m). While this amount of horizontal inaccuracy was not expected with the [N] image set, the vertical doming was so prominent towards the surface edges of the study site that several checkpoints had very poor alignments. The [C] surface models had significantly better horizontal accuracies than the [N] surface models and better vertical accuracies (vertical RMSE: 0.124 m, horizontal RMSE: 0.037 m).

When GCPs were incorporated into the self-calibrating BA for each field campaign, the coupling of nadir and oblique imagery consistently led to the highest checkpoint accuracy; most notably when a sparse distribution of GCPs were used (Fig. 2.6). The [N] image set improved by the greatest amount as GCPs were incorporated into the self-calibration (vertical checkpoint RMSE values; no GCPS: 0.151 m, 13 GCPs: 0.052 m, 17 GCPs: 0.040 m, 21 GCPS: 0.028 m). These results contrast with the [NC_{26}] image set which experienced a small improvement and possibly reached a maximum accuracy around 0.028 m (vertical checkpoint RMSE values; no GCPS: 0.047 m, 13 GCPs: 0.029 m, 17 GCPs: 0.029 m, 21 GCPS: 0.028 m). The [N], [NC_5], and [NC_{26}] image sets converged towards a similar vertical error metric at 21 GCPs of approximately 0.028 m which is expected based on our RTK-GNSS vertical inaccuracy of ±0.02 m. Horizontal accuracies were very similar between all image sets at 21 GCPs (RMSE range: 0.013 to 0.018 m). The [C] image set had slightly lower horizontal and vertical accuracies for each GCP test due to a large number of outliers.

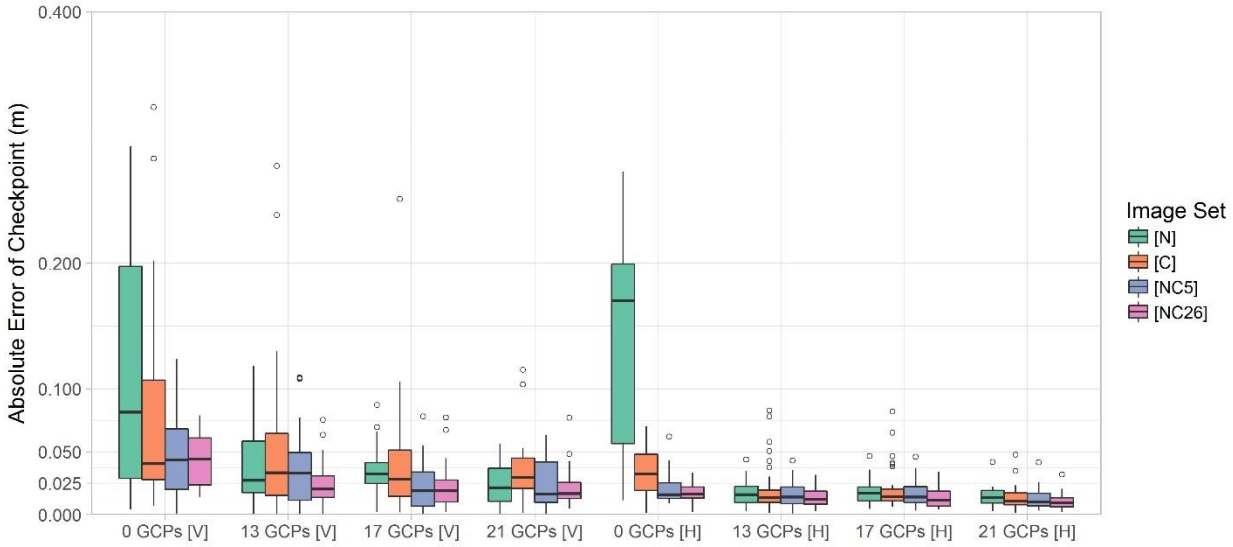

Fig. 2.6. Boxplots depicting the absolute vertical [V] and horizontal [H] error of checkpoints across all three field campaigns for all four image sets (i.e., [N], [C], [NC_5], and [NC_{26}]). Vertical and horizontal RMSE accuracy metrics at 21 GCPs [V, H]: [N] 0.028 m, 0.017 m, [C] 0.048 m, 0.018 m, [NC_5] 0.032 m, 0.016 m, [NC_{26}] 0.028 m, 0.013 m.

2.4.2. Quality of surface model reconstructions

Despite the highly accurate results obtained from the incorporation of oblique imagery into our UAV surveys (most notably the [NC_{26}] image set), the use of oblique imagery proved to be a significant detriment to the generation of certain surface models. The [C] surface models had gaps due to insufficient keypoint matches between image pairs and contained large amounts of vertical noise. Both the [NC_5] and [NC_{26}] image sets had poor homologous keypoint matching between oblique and nadir imagery leading to: 1) the pointcloud being processed as 2–3 independent blocks (Campaign 3; [NC_{26}]), 2) migrating vertical error when the nadir image network was tied to the oblique image network at a single image (Campaign 2; [NC_5] [NC_{26}]), and 3) a large amount of vertical noise (Campaign 2 & 3; [NC_5] [NC_{26}]). These errors were the most pronounced for Campaign 2 when the surface texture and coloration of the field was homogeneous and the lighting conditions were bright (no cloud cover). The Campaign 1 surface model for the [NC_5] and [NC_{26}] image sets had excellent matching between nadir and oblique imagery and did not experience keypoint matching issues.

2.4.3. Topographic change-detection: erosion and deposition

The [N] surface model processed with all 27 GCPs was chosen for topographic change-detection of our study site. While we initially wanted to test all four different image sets, this was not possible due to large amounts of vertical noise in the surface models constructed using oblique imagery. Each campaign's (1–3) [N] surface model underwent our coregistration procedure (i.e., GCP

elevations were iteratively edited by ±0.02 m to minimize changes in areas of invariant topography) before change-detection results were calculated. The coregistration procedure significantly reduced surface coregistration error in the southern portion of the study site where the GCP network was sparse.

Between Campaign 1 (May 7) and Campaign 2 (May 17) the study site was tilled (May 12) and one erosive rainstorm occurred on May 15 with a total precipitation amount of 8.4 mm. Change-detection results using the M3C2 algorithm (vertical normal, 0.15 m projection) between Campaign 1 and 2 calculated a mean surface change of +0.010 m. A mean surface change of this magnitude is within our margin of error and indicates that no detectable mean surface-change occurred. Tillage lines, wheel tracks, infilled gullies, and areas where sediment was manually dug out from around the surface inlets are clearly visible in the change-detection map (Fig. 2.7c, d, e). Surface-change due to tillage and water erosion cannot be differentiated on this change-detection map.

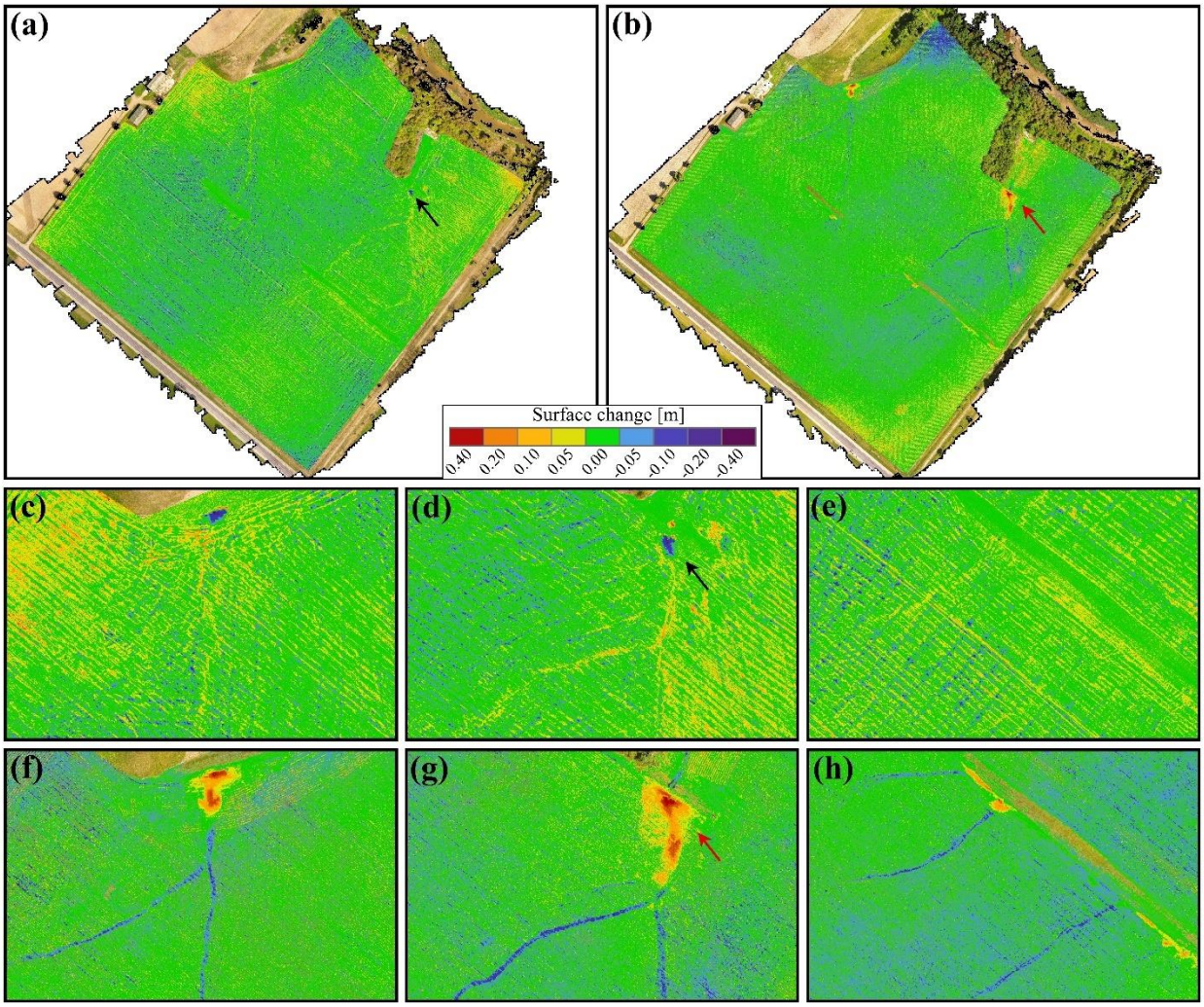

Fig. 2.7. [N] Surface model M3C2 difference: (a) Campaign 1 to 2 (tillage; mean surface change +0.010 m), (b) Campaign 2 to 3 (erosion; mean surface change −0.020 m), (c, d, e) Campaign 1 to 2 catch basins, and (f, g, h) Campaign 2 to 3 catch basins. Arrows indicate the north-east catch basin used for comparison with terrestrial laser scanner results, whereby black corresponds to difference between Campaign 1 and 2 (a, d) and red corresponds to difference between Campaign 2 and 3 (b, g).

Between Campaign 2 (May 17) and Campaign 3 (June 15) three precipitation events with moderate intensity occurred (i.e., exceeded 5 mm hr^{-1}): May 20 (16 mm), May 31 (19.6 mm), and June 3 (8.8 mm). The cumulative precipitation between Campaign 2 and 3 totaled 56.4 mm. Our M3C2 change-detection results identified that two major depositional plumes formed in the two northern catch basins (Fig. 2.7f, g) and several minor depositional plumes formed at the southern catch basins (Fig. 2.7h). The presence of depositional plumes were validated by field observations (e.g., Fig. 2c) and accuracy assessed against terrestrial laser scanner (TLS) results (Table 2.2; north-east catch basin). Preferential pathways for flow, ephemeral gullies, and rills (Fig. 2.7f, g, h) are depicted in our change-detection results leading up to depositional zones. The M3C2

change-detection algorithm calculated a mean surface change of −0.020 m between Campaign 2 and 3, which once again indicates that no detectable amount of sediment was lost from the field (i.e., mean surface-change is still within our margin of error).

To determine how accurately sequential UAV surveys can detect small-scale erosional processes (i.e., change-detection), surface models derived from UAV collected data were compared against data collected from a TLS at each campaign for the north-east catch basin (located in the yellow box in Fig. 2.1). Between Campaign 1 and 2 sediment was manually removed from the north-east catch basin (Fig. 2.7d); between Campaign 2 and 3 several erosive rainstorms redistributed sediment across the field with a large depositional plume forming at the north-east catch basin (Fig. 2.7g). The volumetric change between Campaign 1 and 2, for the north-east catch basin, was ~5% different between [N] (−3.02 m^3) and TLS (−2.88 m^3) surface models. The difference between UAV and TLS volumetric change quantification widened to ~25% between Campaign 2 and 3. The [N] surface model calculated the volume of the depositional plume at +33.44 m^3 and the TLS calculated +26.72 m^3. While the [N] surface model over predicted the magnitude of volumetric change, the results are within a 95% confidence interval (using the approach by Lane et al., 2003) for each campaign (i.e. surface change of ±0.040 m). It is important to note that this confidence interval is based on our accuracy assessment with 21 GCPs and 6 checkpoints. The confidence interval is theoretically narrower in areas close to GCPs and confidence in results will decrease as distance from the nearest GCP increases.

The UAV change-detection results of the north-east catch basin were additionally compared to the TLS dataset using the original [N] surface model (i.e., that underwent no additional coregistration procedure) and the [N] surface models that underwent a global elevation shift of ±0.02 m (i.e., a global coregistration procedure; Table 2.2). This allowed for a cross-comparison of accuracies with our unique coregistration procedure (i.e., iteratively shifting GCP elevation values by ±0.02 m). Both the global shift and GCP shift resulted in reasonable alignments in areas of invariant topography, but the global shift resulted in decreased accuracies in areas where the surface reconstruction was already accurate (e.g., north-east catch basin; Table 2.2). The original [N] surface model had poor alignments in the southern portion of the study site where the GCP network was sparse, and minor surface deformation was shown in the change-detection map. Our co-registration procedure (i.e., vertical GCP shift of ±0.02 m before processing) ensured areas with a correct reconstruction were not altered and the shift minimized visible coregistration error in the southern portion of the study site.

Table 2.2. Volumetric surface change of the north-east catch basin with a 95% confidence interval. Surface change calculated using the M3C2 algorithm for: [TLS] surface models, [N] surface models with a ± 0.02 m GCP elevation shift, original [N] surface models, [N] surface models with a ± 0.02 m global elevation shift.

Dataset	Campaign 1 to 2 Volumetric Change	Campaign 2 to 3 Volumetric Change
[TLS]	-2.88 m^3 ± 0.58	+26.72 m^3 ± 5.63
UAV [N] GCP shift*	-3.02 m^3 ± 1.03	+33.44 m^3 ± 10.66
UAV [N] Original	-3.26 m^3 ± 1.09	+33.76 m^3 ± 10.37
UAV [N] Global shift	-3.58 m^3 ± 1.09	+37.64 m^3 ± 10.37

*used for all SfM-MVS change-detection calculations and figures

2.5. Discussion

2.5.1. Surface model accuracy

While the use of SfM-MVS for the production of orthomosaics is becoming ubiquitous, the presented methods and results demonstrate the challenges associated with the use of UAV SfM-MVS for 3D surface reconstructions of agricultural landscapes. Our results demonstrate that in the absence of GCPs, the coupling of nadir and oblique imagery led to the highest checkpoint accuracy in both the vertical and horizontal dimensions (e.g., [NC_{26}] checkpoint error; vertical RMSE: 0.047 m, horizontal RMSE: 0.019 m). The addition of oblique imagery eliminated the doming effect of the [N] surface model but both the [NC_5] and [NC_{26}] surface models still exhibited some surface deformation (Fig. 2.5). When GCPs were incorporated into the self-calibrating BA, the [N], [NC_5], and [NC_{26}] surface models all converged towards similar vertical (21 GCPs; RMSE 0.028 m to 0.032 m) and horizontal checkpoint accuracies (21 GCPs; RMSE 0.013 m to 0.018 m). All surface models had at least one outlying checkpoint error when 21 GCPs were used in the BA, indicating that a denser GCP network was needed to combat surface deformation for all image sets. While the [NC_5] and [NC_{26}] surface models performed well across all checkpoint accuracy assessments, the addition of oblique imagery did not provide any notable advantage over the [N] surface models when 21 GCPs were used in the BA.

The addition of oblique imagery with the [NC_{26}] image set caused a threefold increase in aerial surveying times and a fivefold increase in processing times in Pix4D (Table 2.1). While other studies recognize the benefits of oblique imagery (e.g., Harwin et al., 2015; James and Robson, 2014), we found that in our agricultural system, with both bare ground and vegetated conditions, that our [C], [NC_5], and [NC_{26}] image sets poorly reconstructed the observed 3D surface. Our agricultural study site is a very difficult environment for SfM-MVS due to low amounts

of image content (i.e., only soil; Campaign 1 & 2) and vegetated surfaces (i.e., rows of corn; Campaign 3). Low amounts of image content led to very poor homologous keypoint matches between nadir and oblique image blocks, creating broad-scale vertical noise across surface models. Despite performing well across checkpoint tests, we would not recommend supplementing flight plans with oblique imagery in agricultural landscapes. The benefits of using oblique imaging angles in SfM-MVS is realized in environments where either GCPs cannot be used or when only a sparse distribution of GCPs can be deployed (e.g., when surveying glacial retreat, coastal cliff erosion, or water erosion in complex landscapes); these environments must also have a high amount of image content to facilitate homologous keypoint matching across oblique imagery. For environments that lack image content, using a UAV platform with built-in RTK-GNSS (e.g., DJI Phantom 4 RTK; Matrice 210 RTK V2) is a promising alternative approach for ensuring high quality 3D surface reconstructions.

Across all landscapes, the incorporation of more GCPs into the BA will result in a reduction in surface error, albeit with diminishing returns as more GCPs are used (e.g., Agüera-Vega et al., 2017; James et al., 2017; Sanz-Ablanedo et al., 2018). Based on our findings in agricultural landscapes, when we used 1.3 GCPs per hectare (i.e., 21 GCPs, 6 checkpoints), the [N] image set (0.017 m resolution) had an average vertical RMSE of 0.028 m across three field campaigns with maximum checkpoint vertical errors of 0.056 m, 0.042 m, and 0.042 m. Our final [N] surface models processed with all 27 GCPs contained some surface deformations with similar maximum vertical errors (estimated ±0.04 m), most notably in the southern half of the study site where the GCP network was sparse. This indicates that 1.7 GCPs per hectare (i.e., 27 GCPs) was not entirely sufficient to combat surface doming; a higher density of GCPs (e.g., 2 to 2.5 GCPs per hectare for 0.017 m ground-sampling-distances) is recommended to combat SfM surface deformation in a nadir image acquisition.

Besides an insufficient GCP network, the other two main bottlenecks (i.e., limiting factor) to UAV SfM-MVS accuracy in our study were RTK-GNSS accuracy (± 0.02 m vertical, ± 0.01 m horizontal) and our ground-sampling-distance. When possible, we would recommend deploying a stable GCP network throughout the study site and on the periphery. Only authors that utilized permanent GCPs throughout their study were able to achieve sub-centimeter accuracy for change-detection (e.g., Eltner et al., 2015). Stable GCPs allow for both a precise co-registration of surface models and remove RTK-GNSS accuracy constraints. For our study, the use of permanent ground controls were only possible outside the study site, which we used as additional GCPs in the BA. Ground sampling-distance was the second bottleneck to our accuracy. While

the relationship between ground-sampling-distance and surface model accuracy is difficult to quantify, the quality of surface reconstructions will degrade as the UAV takes images from higher altitudes (Eltner et al., 2016; Smith et al., 2016) or uses sensors with lower spatial resolutions. Pix4D documentation indicates an expected relative vertical accuracy of 1–3× the ground-sampling-distance, and an in-depth study by James and Robson (2012) found a relative vertical precision of ~1:1000 (measurement precision: observation distance). Based on our maximum vertical errors from checkpoint tests, our vertical accuracy was 3× the ground-sampling-distance and the vertical precision was ~1:2000. Lowering the flying altitude from 90 m to 60 m, to allow for cm-level pixels, could have helped ensure we reached our maximum achievable accuracy. Additional error may have been introduced from our parallel-axis data collection scheme. While it has been shown that using additional flight lines from different directions (i.e., orthogonal flight plans) does not always result in significant improvements in 3D surface reconstructions (e.g., James and Robson, 2014), several SfM software applications (e.g., Pix4D) strongly suggest including orthogonal flight lines for higher quality 3D surface reconstructions. The degree to which our parallel-axis data collection contributed to the observed surface errors is unknown. Other sources of error that are difficult to quantify include error marking the precise center points of GCPs, overexposed imagery, and the use of a rolling shutter.

2.5.2. Agricultural erosion modelling

Agricultural erosion comes with a substantial annual economic cost (e.g., United States $37.6 billion [Uri, 2000]), caused by both on-site and off-site effects. Agricultural erosion is a significant source of excess nitrogen and phosphorus in aquatic ecosystems contributing to eutrophication in freshwater lakes, estuaries and coastal environments (Bennett et al., 2001; Daniel et al., 1998; Foley et al., 2011). On-site redistribution of soil leads to an imbalance of nutrients for plant growth and lower yields. Despite the economic significance of agricultural erosion, spatial and volumetric predictions are mediocre at best (Morgan and Nearing, 2011) and direct measurements of distributed erosion rates are rare.

The most common approach for calculating the magnitude of agricultural soil erosion is employing the use of an erosion model. Researchers will employ either a simple statistical model (e.g., Universal Soil Loss Equation; Wischmeier and Smith, 1978) or a more complex distributed process-based model (e.g., Water Erosion Prediction Project; Flanagan et al., 2001). Newer process-based models allow for both a spatial and volumetric calculation of soil erosion at either the field-scale or watershed-scale by computing runoff and modelling the detachment, transport, and deposition of sediments. Despite large advancements in process-based erosion modelling

over the past decades and a new suite of models, these newer process-based distributed models often fail to outperform older statistical models (e.g., Tiwari et al., 2000).

There exists a need to spatially validate both simple statistical models and process-based models at field and catchment scales. However, sources of reliable input data that describe the heterogeneity of the landscape are few and challenging to acquire. Distributed erosion models are typically calibrated and validated to outlet sedigraphs and hydrographs (i.e., data outside the area of interest). However, not all eroded sediment will be converted to sediment yield at a catchment outlet, which is why outlet sedigraphs are a poor proxy for catchment erosion processes (Syvitski et al., 2005; Morgan and Nearing, 2011); sediment redistribution can occur without making its way into the hydrological network. The use of catchment outlet data to calibrate or validate distributed erosion models is not always a valid approach (Morgan and Nearing, 2011). The challenges associated with model calibration and validation can be further exemplified when dealing with process-based models that tend to have an almost infinite number of degrees or freedom leading to issues with spatial equifinality (Morgan and Nearing, 2011). Without field-scale spatial validation data, it has to be assumed that the model is spatially accurate and models the correct process domains (e.g., rill and sheet erosion processes dominate, ephemeral gully erosion is negligible). It must also logically follow that the correct parameter set has been chosen by the modeler (i.e., no issues with equifinality). Given the economic costs associated with agricultural soil erosion and the corresponding ecological impacts, we need to use the type of data presented in this paper to remove our modelling assumptions. Furthermore, spatial predictions of erosion need to be tested at the scale of the decision-maker (i.e., farm field-scale), which is where erosion mitigation strategies take place.

The analysis of agricultural fields with the UAV SfM-MVS workflow is a promising approach that can provide input, calibration, and validation data for erosion models. While sheet erosion and small-scale rill erosion cannot be detected with this approach (change-detection at the 95% confidence interval was > 0.040 m), larger process domains such as deep rill and gully erosion can be spatially quantified. It is potentially possible to detect smaller erosional processes by: 1) using stable GCPs, 2) employing a denser GCP network, and 3) increasing the ground-sampling-distance. The methodology in this presented research can also be used a priori to inform models of dominant flow paths and depositional zones, allowing for a more accurate description of the connectivity of the landscape, and can be used to assess the predictive capabilities of erosion models at the field and small-catchment scale.

2.6. Conclusions

We presented a comprehensive accuracy assessment of four different UAV survey designs for use with a self-calibrating bundle adjustment in an agricultural landscape. Our findings demonstrate that the coupling of nadir and oblique (15 degree) imagery (i.e., [NC_5], [NC_{26}]) improves the relative accuracy of agricultural 3D surface models in the absence of GCPs and with a sparse distribution of GCPs. With a more dense distribution of ground controls (i.e., 21 GCPs), the nadir-only [N] surface model had similar vertical checkpoint error metrics (RMSE 0.028 m) to both the [NC_5] (RMSE: 0.032 m) and [NC_{26}] (RMSE: 0.028 m) surface models, and all surface models had similar horizontal checkpoint error metrics (RMSE 0.013 m to 0.018 m). Surfaces generated from image sets that included oblique imagery had poor homologous keypoint matches and were subject to large amounts of systematic noise when feature content on the imagery was low, which is typical in agricultural systems. Processing and survey times were inefficient, costly, and unnecessary with the [NC_{26}] image set given that the [N] image set had similar accuracy metrics with a dense deployment of GCPs. Subsequent [N] surface models were used to reliably identify erosive and depositional processes >0.040 m in depth (i.e., deep rill/gully erosion, and depositional zones). Small-scale erosion processes, such as sheet erosion, are not detectable with the presented UAV SfM-MVS methodology. Relative to a TLS, our sequential UAV surveys over predicted the volumetric change of a sediment plume by 5% and 25% for respective field campaigns. Due to RTK-GNSS accuracy constraints, our results verge on the maximum possible achievable accuracy. In an agricultural landscape, we recommend the use of nadir-only imagery for subsequent UAV surveys with a comprehensive ground control network to combat surface deformation and for use as checkpoints (i.e., 2–2.5 GCPs per hectare when flying at 90 m above-ground-level). Where possible, stable ground controls should be deployed in the study site for surface co-registration and to avoid the accuracy constraints of RTK-GNSS. Caution should be taken when interpreting SfM studies that do not include a comprehensive accuracy assessment of their 3D surface model. Future research should be aimed at the application of UAV SfM-MVS in agricultural settings for studying field-scale erosional patterns, calibrating and validating erosion models, and assessing the hydrologic connectivity of the landscape.

Chapter 3. Where did the soil go? Quantifying one year of soil erosion on a steep tile-drained agricultural field

As published in Science of the Total Environment: Meinen, B. U., & Robinson, D. T. (2020). Where did the soil go? Quantifying one year of soil erosion on a steep tile-drained agricultural field. Science of The Total Environment, 729, 138320. Doi: 10.1016/j.scitotenv.2020.138320

3.1. Introduction

The impacts of soil erosion in agricultural systems continues to be an issue of societal (Pimentel 2006) and scientific (e.g., erosion modelling; Morgan and Nearing 2011) importance. Estimates of the annual economic impacts of soil erosion range from €0.7 to 14 billion in the European Union (13 countries, 150 million ha; Montanarella 2007) to $37.6 billion in the United States (Uri 2000) and $400 billion globally (ELD Initiative, 2015). Due to the combined economic and environmental impact of erosion, a considerable amount of scientific effort has focused on assessing how best management practices affect soil erosion; best management practices include different tillage techniques (e.g., no-till; Lal et al. 2007; Lal 1991), tile drainage (e.g., Uusitalo et al. 2001), cover crops (e.g., Kaspar et al. 2001), crop residue management (e.g., Wilson et al. 2004), and riparian buffer strips (e.g., Uusi-Kämppä and Yläranta 1996; Mander et al. 1997). However, with the rate of soil loss due to erosion (median 18 t ha^{-1} yr^{-1} from conventional agriculture; Montgomery 2007) grossly outstripping the natural rate of soil generation (<1 t ha^{-1} yr^{-1}; Wakatsuki and Rasyidin 1992; Troeh and Thompson 2005; Montgomery 2007), the erosion problem is far from solved.

A critical challenge in reducing erosion rates in agricultural systems involves the manipulation of the hydrological and sedimentological connectivity of the landscape. More specifically, soil erosion rates are reduced by slowing the velocity of overland flow and limiting the transport of detached sediments. While only a small portion of eroded sediments and nutrients from an agricultural system typically reach their hydrologic catchment outlet (Walling 1983), the cumulative impacts off-site can cause eutrophication (Bennett et al. 2001), harm to aquatic life (Richter et al. 1997), and degradation of water quality (Parry 1998). Therefore, agricultural best management practices need to be designed and installed to impede the movement of sediments and nutrients from fields to waterways. Despite the wide application of best management practices to reduce soil erosion (e.g., adoption of no-till; Derpsch et al. 2010), there exists a paucity of distributed data at the field-scale that quantifies their effectiveness and instead their success is typically evaluated aspatially.

Part of the reason the effectiveness of best management practices at reducing soil erosion rates is not typically quantified at the field-scale is due to the challenges associated with the collection of distributed erosion data. Current data collection techniques are either qualitative (e.g., mapping erosional features on airborne imagery, Desprats et al. 2013; social surveys on erosional indicators, Okoba and De Graaff, 2005), limited to small spatial extents (e.g., erosion pins, Keay-Bright and Boardman 2009; terrestrial laser scanners [TLS], Eltner et al. 2013; terrestrial Structure-from-Motion [SfM], Kaiser et al. 2014), or have a coarse spatial resolution (e.g., caesium-137 patterns, Walling et al., 2003; in-situ measurements of rill depth and root collar heights, Napoli et al. 2016). While each of the aforementioned field methods excels in one area, the needed outcomes of achieving a high spatial resolution and covering a large spatial extent have been mutually exclusive. Therefore, we have yet to quantify and understand the hydrological flow and subsequent movement of soil and nutrients at meso scales (i.e., farm and field) that are relevant to agricultural decision makers.

Recent advances in unmanned aerial vehicles (UAVs; also known as remotely piloted aircraft systems [RPAS]), and the software and algorithms used for generating 2.5D and 3D surfaces from the imagery they collect (i.e., Structure-from-Motion and Multi-view Stereo algorithms; SfM-MVS), provide a conduit to collect very-high resolution data at meso scales that can be used to quantify soil erosion and deposition (Chapter 2; Meinen and Robinson 2020b). While field-scale studies using UAVs to quantify agricultural erosion are few, UAVs and SfM-MVS have been able to quantify gully erosion (e.g., d'Oleire-Oltmanns et al. 2012), rill erosion (e.g., Eltner et al. 2015), badland erosion (e.g., Smith and Vericat 2015; Neugirg et al. 2016), gorge erosion (e.g., Cook 2017), and landslides (e.g., Turner et al. 2015). The high spatial and temporal resolution of UAV imagery combined with SfM-MVS enables the assessment of volumetric change, which offers a novel opportunity to quantify and evaluate the effects of best management practices on reducing soil erosion at the scale of an individual farm field.

Since agricultural landscapes have become the largest anthropogenic biome, occupying 38% of the earth's terrestrial surface (Foley et al. 2011), it is important to consider how new technologies, like UAVs, can be used to further our understanding of agricultural systems. In this study we use UAV imagery and SfM-MVS to answer the following questions: 1) what is the annual erosion rate of a steep tile-drained moldboard-plowed agricultural field, 2) how much sediment is prevented from being transported off-site from the installation of soil berms and surface inlets (i.e., catch basins), 3) how accurate are UAV SfM-MVS surveys with respect to a TLS, and 4) what are

the controlling factors on the variability in crop yields? To answer these questions, we conducted nine comprehensive UAV surveys over the course of a year.

3.2. Materials and methods

3.2.1. Study site

Our study site is situated within the Grand River Watershed, adjacent to the Nith River, in southern Ontario, Canada. The Nith River has been identified as containing a high volume of sediment and nutrients, which is potentially contributing to the eutrophication of Lake Erie (i.e., elevated levels of total phosphorus; Loomer and Cooke 2011). The Nith River is largely influenced by snow melt and spring storms, with flows adjacent to our study site averaging 9.3 m^3 s^{-1} during the spring (i.e., March/April), that drop down to 3.1 m^3 s^{-1} in the summer months (July to September). An extensive tile-drainage network covering 56% of the upper-Nith River basin contributes to these high spring discharges. The Nith Watershed is composed of silty tills, covers an area of 1130 km^2, and is predominantly an agricultural system (~80% of total land area) with row cropping of soybeans and corn. Within this context, an agricultural study site was chosen in the upper-Nith River basin that held variable topography and is a size suitable for sampling (15.9 ha, ~ 40 acres) and standard across much of Midwestern Canada and the United States (i.e., a sixteenth of a Section).

The study site is divided into six drainage basins that flow into catch basins with surface inlets (Fig. 3.1; labels A - F) that are used for soil erosion and deposition calculations. These six distinct drainage basins were created when tile drainage was installed in the winter of 2017/2018; soil berms were placed behind six surface inlets to form catch basins to collect surface runoff and eroded soils. The six drainage basins cover an area of 8.5 ha and are representative of average agricultural conditions in the region; the basins are tile drained, comprised of loam and sandy loam soils, under corn production, and have an average slope of 8.2%. The remaining portion of our study is flat and non-contributing or drains directly into a riparian zone.

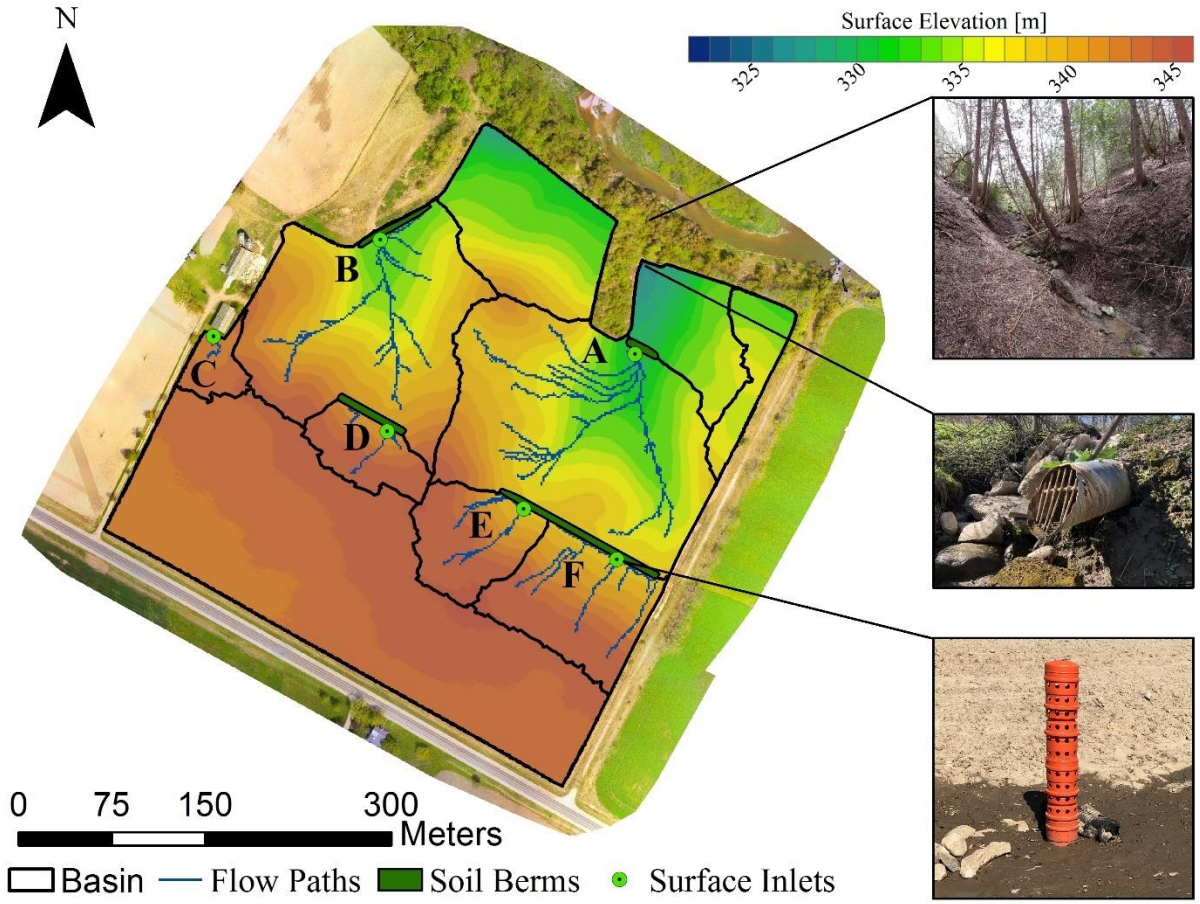

Fig. 3.1. Digital elevation model produced using UAV imagery and SfM-MVS on May 17, 2018, Catch Basins A, B, C, D, E, and F used for soil deposition calculations, D8 flow paths in catch basins after soil berm installation (left), a gully incised through the riparian zone (top right), a tile drain outlet (middle right), and a surface inlet (bottom right).

A total of nine surveys were conducted over a one-year period from May 7, 2018 to June 14, 2019. The field was tilled on May 12, 2018 (cultivator, 2 passes) and corn was planted the following day on May 13, 2018. The corn was harvested on November 11, 2018 followed by a tillage on December 10, 2018 (moldboard, 1 pass). The surveying year was broken into two study periods: May 17, 2018 to September 19, 2018 (4 surveys; Study Period One) and December 18, 2018 to May 16, 2019 (3 surveys; Study Period Two). The two study periods are based on when UAV surveying was possible (i.e., when the soil surface wasn't completely obscured); a surveying gap exists between September 19, 2018 and December 18, 2018 where corn or corn residue completely obscured the surface of the field. Cumulative precipitation totaled 376.4 mm (rainfall) during Study Period One and 387.6 mm (mixed precipitation) over Study Period Two. Mean daily air temperatures ± one standard deviation collected from a local meteorological station were 19.6 ± 3.5° Celsius during Study Period One and − 1.3 ± 7.7° Celsius during Study Period Two.

Soil deposition was measured at Catch Basins A, B, C, D, E, and F (adjacent to the surface inlets) a total of three times during Study Period One and twice during Study Period Two using UAV SfM-MVS change-detection. Each field survey consisted of an aerial image acquisition with a UAV, a real-time kinematic global navigation satellite system (RTK-GNSS) ground control point (GCP) survey, and a TLS survey. Soils that had built up in catch basins were manually removed before each study period and redistributed along the flow paths within the study site; the study site was then tilled.

3.2.2. Unmanned aerial vehicle (UAV) survey

The R60 SkyRanger UAV, acquired from FLIR Systems, was used for all image acquisitions. A SR-3SHD payload was mounted to the UAV system which captures 15 MP RGB 4608 × 3288 resolution images with a 46-degree field of view. The payload has a 6.45 × 4.60 mm electro-optical sensor with a 7.5 mm focal length and is attached to a 3-axis gimbal for image stabilization during flight. The UAV flight was automated using FLIR System's Mission Control software to capture nadir imagery using parallel-axis flight lines with a 70% frontlap and sidelap. The initial five UAV surveys were flown at 90 m above-ground-level (AGL; 0.016 to 0.018 m ground-sampling-distance [GSD]), while the next three UAV surveys were flown at 50–60 m AGL (0.011 to 0.014 m GSD; Table 3.1). The flying height was reduced since it was difficult to identify rills in the 90 m AGL orthomosaics. The UAV was flown at 4 m s^{-1} at 90 m AGL and 3 m s^{-1} at 50–60 m AGL to prevent motion blur.

Table 3.1. UAV survey details. Processing settings in Pix4D: keypoint image scale of 1, standard calibration, all camera optimizations, optimal image scale (1/2), optimal point density (i.e., one point generated for every 8 pixels). GCP and checkpoint RMSE is expressed as horizontal (H) and vertical (V) accuracy.

Survey date	Number of images	UAV height (m)	GCPs	GSD (m)	GCP RMSE [H,V] (m)	Checkpoint RMSE [H,V] (m)
2018-05-07	585	90	27	0.016	0.009, 0.008	0.012, 0.029
2018-05-17	485	90	27	0.017	0.010, 0.010	0.011, 0.026
2018-06-15	508	90	28	0.017	0.008, 0.006	0.019, 0.031
2018-07-14	554	90	31	0.018	0.009, 0.009	N/A
2018-09-19	601	90	32	0.017	0.011, 0.007	N/A
2018-12-18	1266	60	33	0.011	0.007, 0.008	0.010, 0.039
2019-04-25	1295	60	54	0.011	0.008, 0.010	0.009, 0.021
2019-05-16	N/A*					
2019-06-14	557**	50	69	0.014	0.012, 0.017	0.015, 0.025

*A TLS survey was done in lieu of a UAV survey for all six catch basins **2019-06-14 survey was conducted with FLIR System's HDZoom30 camera (specifications: 20 MP RGB 5184 x 3888 resolution images, 68.6-degree field of view)

Before each UAV survey, GCPs were distributed across the study site and measured with SmartNet's network RTK-GNSS using a Leica Viva GS14 and Leica Viva CS15 field controller. Our GCPs are 12 × 12 in. plywood squares painted a bright fluorescent orange in the shape of an "X" for aerial identification. The number of GCPs used and their spatial locations varied between campaigns due to differing aerial visibilities and for accuracy assessments (see Fig. 3.2). All campaigns had at least one GCP placed close to each surface inlet to ensure accurate topographic-change could be measured with the UAV SfM-MVS workflow. The field campaign on April 25, 2019 had the most ideal distribution of GCPs (54 GCPs, UAV 60 m AGL); Meinen and Robinson (2020b; Chapter 2) demonstrate that this dense network of GCPs is necessary to minimize 'surface doming' as is commonly seen in SfM-MVS with nadir only imagery (James and Robson 2014). Minor vertical surface deformation (i.e., ~ 0.04 m) was present in all our SfM-MVS surface models which made topographic change-detection in areas without GCPs difficult to interpret. The 90 m AGL surface models (with 27–32 GCPs) had estimated global accuracies (root-mean-square-error [RMSE]) of 0.028 m (vertical) and 0.014 m (horizontal), while the 60 m AGL surface model (with 54 GCPs) had an estimated global accuracy (RMSE) of 0.021 m (vertical) and 0.009 m (horizontal). The June 14, 2019 survey with 69 GCPs had an unexpectedly high checkpoint RMSE (Table 3.1) due to using a different camera (FLIR System's HDZoom30)

which has an additional uncalibrated glass lens used to protect the camera lens. These accuracy metrics are based on checkpoint error; each surface model was iteratively reprocessed with one GCP removed and used as a checkpoint (i.e., always X – 1 GCPs and 1 checkpoint). Once all the processing was complete, the top 5% of checkpoints with the highest error were removed and the remaining 95% of checkpoints were used to calculate accuracy metrics. This checkpoint error is used to generate a conservative estimate on the global accuracy of each surface model. For all surface models, areas close to GCPs should be constrained to a maximum error of 0.02 m (i.e., RTK-GNSS vertical accuracy); UAV SfM-MVS accuracy is constrained by both GSD, camera orientation, and ground control accuracy and density.

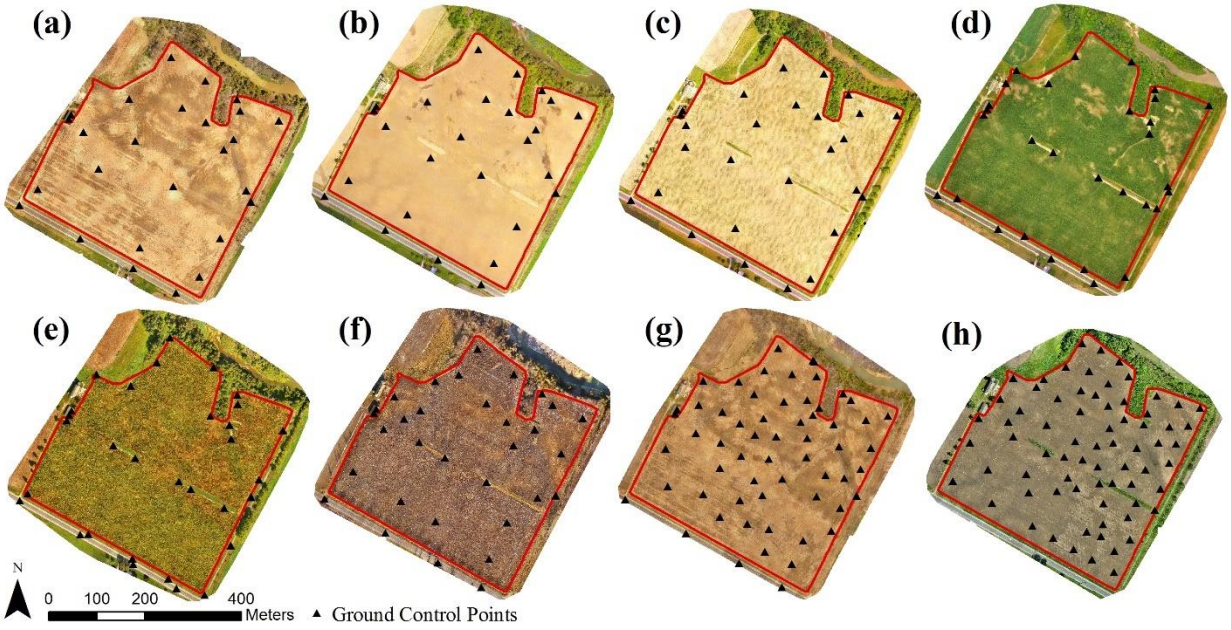

Fig. 3.2. UAV orthomosaics and GCP positions (black triangles) for each field campaign: (a) May 7, 2018, (b) May 17, 2018, (c) June 15, 2018, (d) July 14, 2018, (e) September 19, 2018, (f) December 18, 2018, (g) April 25, 2019, (h) June 14, 2019. The UAV was not available for the May 16, 2019 field campaign.

3.2.3. SfM-MVS image processing details

All UAV imagery was processed in Pix4D (Pix4D SA, Switzerland) for 3D pointcloud and orthomosaic generation. Overexposed images were removed from image sets before each dataset was processed; the June 15, 2018 survey contained a high number (~30) of overexposed images due to flights being conducted at solar noon. A self-calibrating bundle adjustment was used which incorporated all the GCPs (i.e., no GCPs were used as checkpoints in the final pointclouds). All datasets were processed on a Dell Precision Workstation 5810 Tower operating on Windows 7 64-bit with Intel Xeon CPU E5–1620 v3 @ 3.5203 GHz with quad-core, 8

processors, 64 GB RAM, and NVIDIA Quadro K4200 graphics card. The full Pix4D workflow took between 2 and 3 h for 90 m AGL UAV flights and between 8 and 10 h for 60 m AGL UAV flights, with an additional 1–2 h per campaign to mark GCPs in imagery. CloudCompare v2.9.1 (https://www.danielgm.net/cc/) was used for data filtering (i.e., removing spurious points and vegetation).

3.2.4. Terrestrial laser scanner (TLS) survey

TLS surveys were conducted in Catch Basin A using a Leica Multistation MS50 and were used to benchmark UAV SfM-MVS change-detection calculations. Each survey covered an area of 1 ha and was clipped to the depositional plume in Catch Basin A (40 × 40 m). Three different scan positions were used to capture the 3D geometry around the catch basin; total scanning time was approximately 2 h per campaign. The TLS collected an average of 2.9 million points per field campaign (GSD of 0.01 m on the depositional plume). Leica Infinity v3.0.0.3068 was used for filtering the TLS pointclouds.

3.2.5. Change-detection: Deposition calculations

Topographic change-detection was calculated using the M3C2 algorithm (Lague et al. 2013) in CloudCompare v2.9.1 (https://www.danielgm.net/cc/) at each of the six catch basins. The M3C2 algorithm is a robust way to detect change on noisy SfM-MVS pointclouds; a cylinder is fitted to a vertical normal which calculates the average distance between points in the cylinder. For M3C2 change-detection calculations we used a 0.15 m projection with vertical normals; volumetric change was calculated by resampling and rasterizing the resultant M3C2 pointcloud to a 0.05 m raster and multiplying vertical differences by the horizontal surface area. Topographic change at each catch basin was considered significant, i.e., real topographic change, if the depositional plume exceeded 0.04 m in depth on the UAV SfM-MVS pointcloud or 0.02 m in depth on the TLS pointcloud (based on Meinen and Robinson 2020b; Chapter 2).

3.2.6. Soil survey

Bulk density surveys were conducted across the study site to convert the volume of depositional plumes (m^3) to a weight (tonnes). Soil samples were taken once during each Study Period (September 19, 2018; April 25, 2019) at each catch basin (i.e., Catch Basin A - F) if deposition occurred. A bulk density ring was used to extract two samples at a depth of 15 cm from the depositional plumes in each catch basin; a total of 16 samples were collected. Soil samples were dried for 24 h in a conventional oven at 105° Celsius and weighed to determine bulk density. Depositional plumes consisted primarily of clay with an average bulk density of 1.32 g/cm^3.

Soil texture surveys were conducted in Basin A to determine if soil texture was the primary controlling factor on crop yield. A total of 27 aggregated soil samples were collected for textural classification on September 3, 2019. A sieve and hydrometer analysis was conducted on each soil sample; soils were classified as a mix of sandy loam and loam with an average clay content of ~13%. ArcGIS v10.6.1 was used to rasterize the 27 soil samples into a 1 m raster using ordinary kriging.

3.2.7. Landform element classification

To determine if topographic position, slope, or profile curvature were controlling factors on the variabilities in crop yield, the study site was sub-divided into four topographic landform elements: 1) flats, 2) shoulders, 3) backslopes, and 4) footslopes. The landform element classification is based on an aggregated version of Branton and Robinson's (2019) classification scheme. Landform elements with linear profile curvatures are classified as flat if they have slopes <3° and classified as backslopes if they have slopes >3°. Shoulders are defined as having a convex profile curvature and footslopes are defined as having a concave profile curvature. All landform element classifications are based on a 3.2 m digital elevation model (DEM); higher resolution DEMs masked the trends in the macro-topography. The study site landform element classification consists of: 36.3% flat, 19.4% shoulders, 15.9% footslopes, and 28.5% backslopes.

3.2.8. Crop yield survey

Crop yield data were collected during harvesting on November 11 using a John Deere 9770 STS. The harvester calculated crop yield at 15.5% moisture every 1.5 m and generated a shapefile of average yield per point. A total of 189 t (7441 bushels) of corn were harvested from 15.63 ha (38.62 acres) of workable land, resulting in an average yield of 12.09 t ha^{-1} (192.65 bu. ac^{-1}). ArcGIS v10.6.1 was used to rasterize the crop yield shapefile into a 1 m raster using ordinary kriging for statistical comparisons.

3.2.9. Statistical analysis

To examine the relative influence of topography, hydrology, and soil on crop yield variability, we compared average corn yields with our landform element classification (i.e., shoulder, backslope, flat, footslope), water erosion, and soil textural classification. We additionally compared water erosion rates to rainfall amount and rainfall intensity to see if precipitation was the controlling factor on the variability in erosion rates. All comparisons were made using R v3.3.3 with the ‘raster’, ‘sp’, and ‘rgdal’ libraries. Pearson correlation coefficients were used to determine the

strength of relationships between variables and statistical correlations were considered significant for $p < .01$.

3.3. Results

3.3.1. UAV SfM-MVS change-detection

A total of 376.4 mm of rainfall fell during Study Period One and 387.6 mm of mixed precipitation fell during Study Period Two (Fig. 3.3). The cumulative total of 764 mm of precipitation that fell over these two study periods was highly variable in intensity; 12 rainfall events had rainfall intensities exceed 5 mm hr^{-1} in Study Period One while only 5 rainfall events during Study Period Two exceeded 5 mm hr^{-1}. The combined impacts of high rainfall intensities, warm air temperatures (average daily air temperature of 19.6 °C for Study Period One) and loose cultivated soils following the May 12, 2018 tillage resulted in 57% of the annual erosion occurring during Measurement #1 (May 17, 2018 to June 15, 2018) and 86% of the total annual erosion occurring during Study Period One (Fig. 3.3). We speculate that low rainfall intensities coupled with frozen soil (average daily air temperature of −1.3 °C) during Study Period Two mediated the degree of erosion that happened over the winter months (Fig. 3.3); however, there was no statistically significant correlation between rainfall intensity and rainfall amount with water erosion over the study year.

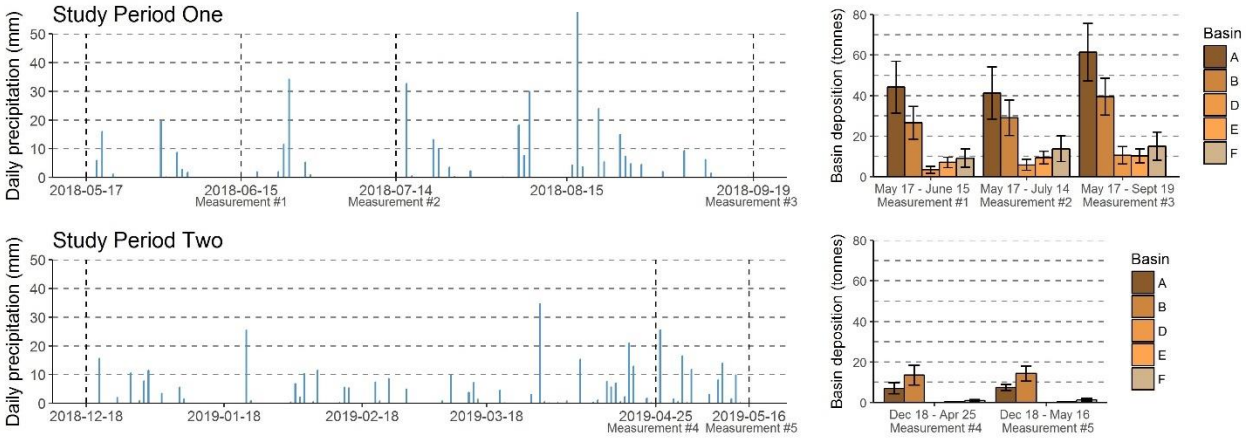

Fig. 3.3. Daily precipitation totals and cumulative UAV SfM-MVS soil deposition measurements for Study Period One (May 17, 2018 to September 19, 2018) and Study Period Two (December 18, 2018 to May 16, 2019) in each catch basin. Precipitation was rainfall in Study Period One and mixed precipitation in Study Period Two. Soil deposition values are calculated in each catch basin with ±0.04 m confidence intervals.

UAV SfM-MVS change-detection procedures calculated that an annual cumulative total of 120.85 m^3 of sediment was deposited across all six catch basins, corresponding to 159.52 t of sediment (average bulk density of 1.32 g/cm^3). The measured erosion rate (i.e., soil loss to catch

basins per unit area) in Catch Basins A, B, C, D, E, and F, were 20.95 t ha^{-1} yr^{-1}, 20.09 t ha^{-1} yr^{-1}, 0 t ha^{-1} yr^{-1}, 21.92 t ha^{-1} yr^{-1}, 14.33 t ha^{-1} yr^{-1}, and 14.86 t ha^{-1} yr^{-1}, respectively. The combined annual erosion rate of all six steep tile-drained agricultural basins was 18.83 t ha^{-1} yr^{-1}.

During Study Period One (May 17, 2018 to September 19, 2018), 136.40 t of sediment was eroded and transported to all six catch basins (Fig. 3.3; Measurement #3). The majority of soil erosion occurred between May 17 and June 15 (Fig. 3.3; Measurement #1); 56.4 mm of rainfall fell, with 3 storms exceeding 5 mm hr^{-1}, resulting in the transport and deposition of 90.26 t of sediment to catch basins. Seven ephemeral gullies formed across the study site (Fig. 3.4) which provided preferential flow pathways for the transport of sediment to the six catch basins. The gullies were wide and shallow (e.g., largest ephemeral gully in Basin A was 2 m wide and 0.15 m deep). Deeply incised rills developed later in the growing season (i.e., August/September); rills formed primarily on hillslopes between rows of corn. Basin A and B experienced the highest volume of water erosion and had the largest depositional plumes in catch basins (Fig. 3.5).

Fig. 3.4. (a) Ephemeral gully in Basin A where the topography converges at a low point (June 15, 2018), (b) sidewall of a shallow ephemeral gully in Basin A cutting through sandy soil (June 15, 2018), and (c) deeply incised rills on a hillslope in Basin A (September 19, 2018).

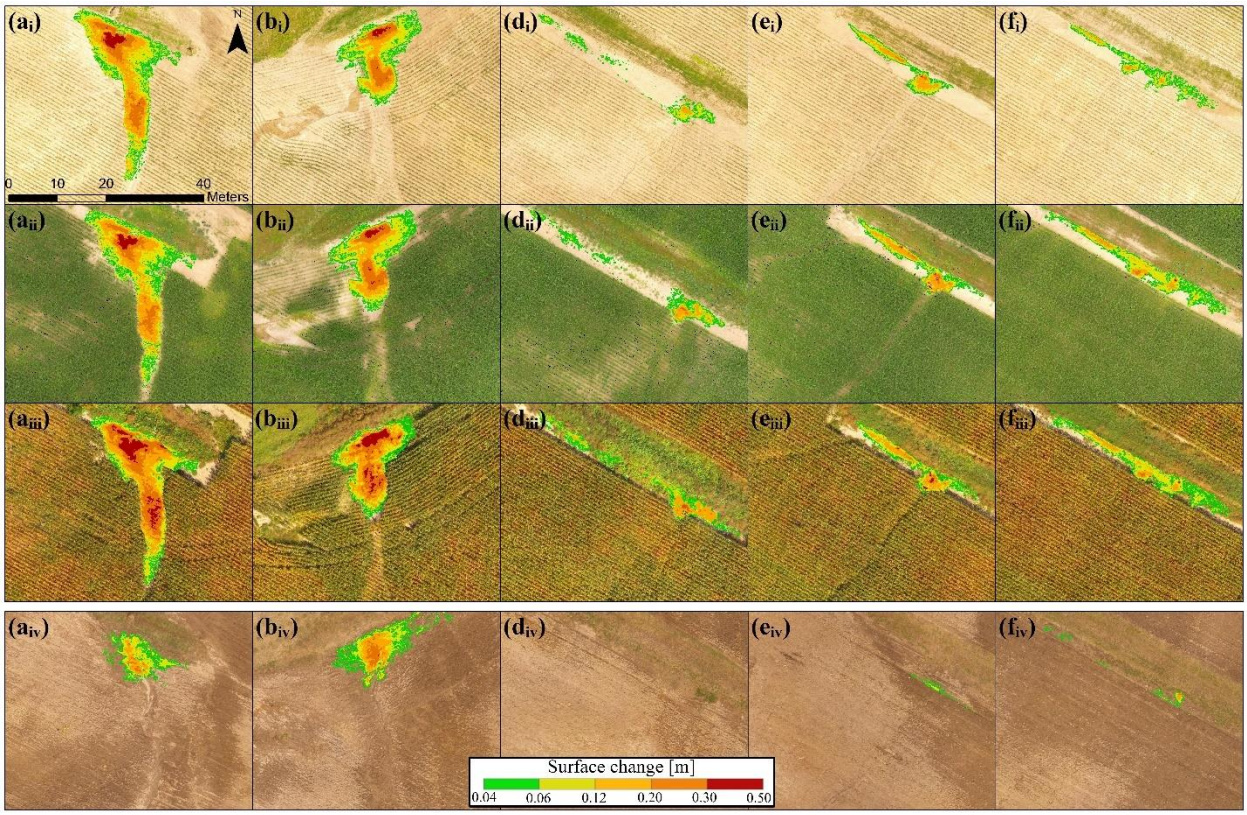

Fig. 3.5. Depositional plumes at Catch Basin A, B, D, E, and F from UAV SfM-MVS M3C2 calculations: (a) Basin A, (b) Basin B, (d) Basin D, (e) Basin E, and (f) Basin F; (i) Measurement #1; May 17 to June 15, (ii) Measurement #2; May 17 to July 14, (iii) Measurement #3; May 17 to September 19, and (iv) Measurement #4; December 18 to April 25. No orthomosaic was available for Measurement #5; UAV equipment was unavailable.

During Study Period Two (December 18, 2018 to May 16, 2019), 23.13 t of sediment was eroded and transported to catch basins (Fig. 3.3; Measurement #5). A site inspection in March showed that no preferential flow paths to the catch basins had formed; the tillage in December before Study Period Two filled in all ephemeral gullies and they were not yet re-established. Rainfall and snowmelt pooled at their points of inception and did not flow towards catch basins. From late March onwards several large spring storms started to re-establish small ephemeral gullies in Basins A and B that enabled the transport of sediments to catch basins. Basin's A and B had moderately large depositional plumes approaching the surface inlets (Fig. 3.5), but they were substantially smaller than the depositional plumes in Study Period One. The remaining basins had little to no deposition around surface inlets (i.e., < 1 t of sediment), due in part to smaller contributing areas and more gradual slopes.

To verify the reliability of our UAV SfM-MVS change-detection calculations we compared our results against a TLS benchmark for Catch Basin A (Table 3.2). Across six comparisons, the

UAV SfM-MVS change-detection results had an average error of 4.23 t; Measurement #1 had the largest error of 8.87 t. Volumetric estimations were most accurate where the depositional plume was deeper and could be detected more reliably with UAV SfM-MVS change-detection. All UAV surveys were within the bounds of the TLS surveys when using a conservative ±0.04 m confidence interval on UAV SfM-MVS change-detection calculations.

Table 3.2. Cumulative soil deposition from water erosion (Measurement #1–5) and mechanical soil removal at Catch Basin A for both UAV SfM-MVS and TLS datasets. Measurements #1–3 were conducted in Study Period One and Measurements #4–5 were conducted in Study Period Two.

Date and Measurements	Precipitation (mm)	Precipitation events >5 mm hr^{-1}	Tonnes of soil (UAV)	Tonnes of soil (TLS)
Mechanical soil removal				
2018-05-10	N/A	N/A	-3.99 ± 1.36	-3.80 ± 0.76
Measurement #1-3				
2018-05-17 to 2018-06-15	56.4	3	44.14 ± 12.79	35.27 ± 7.43
2018-05-17 to 2018-07-14	112.6	4	41.24 ± 12.82	44.09 ± 8.95
2018-05-17 to 2019-09-19	376.4	12	61.32 ± 14.18	68.59 ± 9.85
Mechanical soil removal				
2018-12-10	N/A	N/A	-49.18 ± 9.18	-45.13 ± 6.88
Measurement #4-5				
2018-12-18 to 2019-04-25	294.2	3	6.95 ± 2.78	4.82 ± 1.25
2019-12-18 to 2019-05-16	387.6	5	Not measured	7.38 ± 1.49

3.3.2. Controlling factors on crop yield variability

The total crop yield from the 2018 corn harvest was 189 t (15.5% moisture) across 15.63 ha of workable land (12.09 ± 2.19 t ha^{-1}; 192.65 ± 32.52 bu. ac^{-1}). The southern portion of the study site had high average yields with low variability (12.42 ± 0.84 t ha^{-1}), contrasted by the northern basins which had highly variable corn yields (e.g., Basin B: 12.02 ± 2.54 t ha^{-1}). Topographic landform elements classified as shoulders had the lowest corn yields (11.34 ± 2.06 t ha^{-1}) while backslopes had the highest yields (12.50 ± 1.92 t ha^{-1}; Table 3.4). Differences between landform elements are further exemplified when looking at differences in crop growth; shoulders had the most stunted corn growth at maturity (mean ± one standard deviation: 1.92 ± 0.24 m) while backslopes had the tallest corn at maturity (mean ± one standard deviation: 2.12 ± 0.26 m). Basin

A was chosen for a more in-depth analysis on the relative influence of topography, hydrology, and soil on crop yields due to its variable topography and high volume of water erosion.

Basin A had a below field-average crop yield of 11.92 ± 2.33 t ha^{-1} (Table 3.3; Fig. 3.6). The four primary controls on crop yield (i.e., highest statistically significant correlations; $p < .01$) in Basin A were: silt, sand, water erosion, and shoulder landform elements. Crop yields had a moderate positive correlation with silt content (correlation coefficient: 0.31) and a moderate negative correlation with sand content (correlation coefficient: −0.30). Topographic shoulders, which had poor soil structure (i.e., high sand content, lower silt and clay content), were negatively correlated with crop yields (correlation coefficient: −0.28). Backslopes had significantly healthier soil structures than shoulders (i.e., lower sand content, higher silt and clay content); however, backslopes were not correlated with increasing crop yields in Basin A. Soils were texturally classified as sandy loam on upslope shoulder positions and loam across the other landform elements (Table 3.4). High rates of deposition from water erosion around catch basins were negatively correlated with crop yields (correlation coefficient: −0.32).

Table 3.3. Average crop yield calculated across all basins. Crop yield calculations are ± one standard deviation.

Basins	**A**	**B**	**C**	**D**	**E**	**F**	**North**	**South**
Crop yield (t ha^{-1})	11.92 ±2.33	12.02 ±2.54	N/A	12.23 ±1.33	11.99 ±1.09	11.59 ±0.97	12.08 ±2.67	12.42 ±0.84

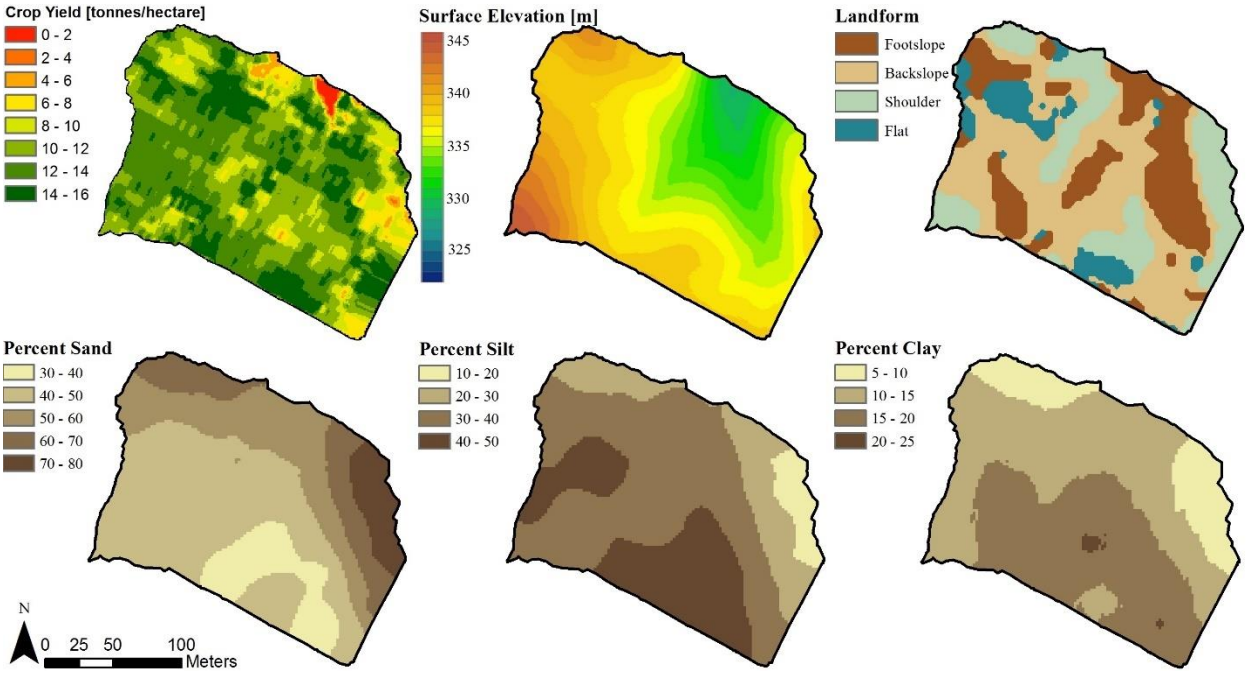

Fig. 3.6. Interpolated raster layers in Basin A: crop yield, surface elevation, landform elements, and soil textural classifications.

Table 3.4. Average soil texture classification in Basin A and average crop yields across the full study site calculated from topographic landform elements. Crop yield calculations are ± one standard deviation.

Landform Elements	Shoulder	Footslope	Flat	Backslope
Slope (degrees)	> 0	> 0	< 3	> 3
Profile curvature	Convex	Concave	Linear	Linear
Sand (%)	58.12	52.73	50.44	46.72
Silt (%)	31.54	34.21	37.26	35.98
Clay (%)	10.34	13.06	12.30	17.30
Crop yield (t ha^{-1})	11.34 ± 2.06	11.72 ± 2.93	12.42 ± 0.84	12.50 ± 1.92

3.4. Discussion

3.4.1. UAV SfM-MVS surface change-detection

Accuracy assessments of UAV SfM-MVS pointclouds are necessary for understanding the efficacy of UAVs for mapping out agricultural erosion and deposition patterns. Given a standard nadir UAV image acquisition, an RTK-GNSS ground control survey, and the use of a self-calibrating bundle adjustment in an SfM-MVS software application, we expect the vertical accuracy (RMSE) of pointclouds to be 2–3× the GSD with a practical upper limit of 0.01 m. Five

out of six of our UAV SfM-MVS surface models had vertical accuracies that were 2× the GSD (Table 3.1 checkpoint error), while one campaign (December 18, 2018) had a more adverse error of 3.5× the GSD. This adverse error was the result of an insufficient ground control network due to the lower flying altitude; as GSD increases, the field-of-view of the camera is constrained to a smaller area and a larger number of GCPs are required to avoid adverse surface error. The reported vertical checkpoint errors (i.e., RMSE) of 0.021–0.039 m indicate that the outlined methodology is best suited towards change-detection of ephemeral gullies, deeply incised rills, and depositional zones.

The presented accuracy metrics of our UAV SfM-MVS pointclouds (i.e., vertical accuracies of 2× GSD) are corroborated across other SfM geoscience literature (e.g., vertical accuracies 0.01 to 0.06 m; Lucieer et al., 2014a, Lucieer et al., 2014b; Stöcker et al., 2015; Gonçalves and Henriques 2015; Harwin et al. 2015; James et al. 2017 [Taroudant]). The constraints of ground control survey accuracy (i.e., GPS, RTK-GNSS) limit the maximum SfM-MVS survey accuracy (i.e., vertical RMSE) to 0.01 m; sub-cm accuracies are only achieved if the reference system is stable (e.g., Eltner et al. 2015) or more accurate than conventional RTK-GNSS (e.g., Harwin et al. 2015). SfM-MVS studies with more adverse vertical error of ~0.10 m (e.g., Pineux et al. 2017; Sanz-Ablanedo et al. 2018) held to the general trend of vertical accuracies being 2–3× the GSD, converging to 2× the GSD given a sufficiently dense network of GCPs (Sanz-Ablanedo et al. 2018). UAV SfM-MVS studies that had vertical errors exceed 2–3× the GSD (e.g., ~0.30 m; Niethammer et al. 2012; Cook 2017) were a result of modelling complex geometry (e.g., cliff overhangs) and vegetated surfaces (e.g., grasses, shrubs) which made bare-earth elevation values difficult to derive.

3.4.2. Land management and soil erosion

Using UAV SfM-MVS change-detection on our 15.9-ha agricultural study site, we were able to spatially quantify the deposition of 159.52 t of sediment across six catch basins; corresponding to an erosion rate of 18.83 t ha^{-1} yr^{-1} across the six studied basins. This rate of erosion was surprisingly high considering tile-drained landscapes are typically less susceptible to erosion via overland flow. In the absence of the installed catch basins these rates of erosion would be unsustainable, outstripping the rate of natural soil regeneration (Montgomery 2007) by an order of magnitude. While erosion rates were unsustainable in the six studied basins, the southernmost basin experienced no visible water erosion (estimated erosion rate of <1 t ha^{-1} yr^{-1}) and had no sedimentological connectivity with waterways; erosion rates were manageable in the flat southern basin without the use of best management practices.

Evaluating agricultural sustainability and the efficacy of agricultural best management practices is difficult since erosion rates are spatially and temporally diverse. For example, our first study interval of May 17 to June 15 (i.e., Measurement #1) was the most significant for soil erosion and deposition processes (Fig. 3.3); 56.4 mm of precipitation resulted in 90.26 t of sediment being eroded and transported to catch basins. This is sharply contrasted by the winter months where 387.6 mm of mixed precipitation resulted in 23.13 t of sediment being transported to catch basins. In this context, planting a winter wheat cover crop followed by no-till soybeans could be very effective at reducing high rates of erosion in the spring (i.e., due to adequate soil cover during spring storms), but winter cover crops that only provide protection until seedbed preparation (i.e., tillage) in the spring may be ineffective at reducing erosion rates (i.e., since the field will be susceptible to soil erosion from spring storms).

On our study site, the installation of catch basins was an effective management practice that significantly reduced soil export via overland flow across all seasons. Before the berm and tile installation, it is estimated that 10.78 ha of the field drained through a riparian zone and into the Nith River; after the installation it is estimated that only 2.51 ha of the field was contributing surface runoff to the Nith River. This equates to a 77% decrease in direct surface flow towards the Nith River and a 32% decrease in the maximum length of concentrated overland flow. However, despite the significant reduction of soil loss from overland flow, the installation of surface tile inlets may have facilitated a preferential flow path for dissolved nutrients to the Nith River. Combining reduced tillage practices (i.e., shallow till, strip till, or no till) with the catch basin installation would likely ameliorate high rates of water erosion and the associated soil and nutrient losses.

3.4.3. Crop yield

Average corn yields across southwestern Ontario were 11.49 t ha^{-1} in 2018, with a 10-year production insurance average of 10.67 t ha^{-1} (Agricorp 2018). Our study site had an average corn yield in 2018 of 12.09 t ha^{-1}, with the majority of the study site having corn yields well above the provincial average; topographic shoulders were the only landform elements to have below average corn yields (11.34 t ha^{-1}). Soil quality was heavily degraded in upslope shoulder positions in Basin A (texturally sandy loams; Table 3.4), while more uniform loam was observed across the other three landform elements. The degraded soil structures on shoulders was likely a result of tillage erosion; east-west tillage patterns resulted in soil loss on shoulders immediately preceded by backslopes. While downslope tillage practices on our study site are pragmatic, care should be taken when tilling fields that are characterized by undulating topography and steep slopes.

Downslope tillage patterns can result in uneven distributions of topsoil leading to lower crop yields in upslope positions. While unaffected by tillage erosion, footslopes had the second lowest crop yield across the study site due to high rates of water erosion. Large areas of washout and ephemeral gullies hindered seedling development at points of topographic convergence. The topographically flat southern region of the study site, which experienced little to no water or tillage erosion, had the most consistently high yields (12.42 ± 0.84 t ha^{-1}).

3.4.4. Best management practices: Water quality

Water erosion facilitates the off-site export of sediments and associated agro-chemicals to waterways via overland flow. Agricultural catchments contribute large loads of bioavailable phosphorus to freshwater systems which has led to recurring problems of eutrophication (e.g., Lake Erie; Michalak et al. 2013). Our results highlight the need for implementing best management practices in the agricultural mosaic of southwestern Ontario. The Nith River Watershed has ~90,000 ha of land devoted to agricultural use and exports 15,820 t of sediment per year into the Grand River (Cooke 2006). This is the largest amount of sediment contributed from any tributary into the Grand River, and the sediment is thought to be coming primarily from diffuse non-point agricultural sources.

As a gross simplification of the erosion problem (i.e., ignoring river transport, depositional mechanisms, and other erosion sources), only 100 replicate fields of our study site would be needed to produce the 15,820 t of sediment that the Nith exports (i.e., 159.52 t × 100 fields). This is important to consider from a policy standpoint; only 2% of all agricultural land in the Nith Watershed (i.e., 1595 of 90,000 ha; 100 replicate fields) could be needed to match the Nith Rivers annual sediment export budget. While it is expected that >2% of agricultural land would contribute to elevated levels of suspended sediments, the tail end of this distribution likely contributes the majority of the pollutants. The agricultural fields of concern are those with direct hydrologic connectivity with waterways, steep topography, and poor riparian vegetation. The Canadian Farm Environmental Management Survey (2011) highlights that 41% of Canadian farms have a waterway passing through their property; the subset of these 41% of farms that do not have any best management practices implemented are of particular interest for targeting grants and subsidies. Across Canada, 35% of farms have developed an environmental farm plan (EFP) of which 95% have implemented the best management practices outlined in their EFP. The main rationale for not developing an EFP and using best management practices was economic pressures (Statistics Canada 2011); studies in the United States also highlight that one of the largest barriers to the adoption of best management practices is economic cost (e.g., Rodriguez

et al. 2009). Removing economic pressures by fully subsidizing the costs of specific best management practices is an important step forward for cost-effectively improving surface water quality.

3.5. Conclusions

The presented research was conducted to determine 1) what is the annual erosion rate of a steep tile-drained agricultural field, 2) how much sediment is prevented from being transported off-site from the installation of soil berms and surface inlets (i.e., catch basins), 3) how accurate are UAV SfM-MVS surveys with respect to a TLS, and 4) what are the controlling factors on the variability in crop yields? We calculated the annual erosion rate of our steep tile-drained agricultural field using UAV SfM-MVS change-detection; the average erosion rate was 18.83 t ha^{-1} yr^{-1} with the majority of erosion being associated with spring storms after the corn planting. Our results highlight that our UAV SfM-MVS surveys were accurate and able to reliably match the accuracy of TLS-derived surface reconstructions when using a ± 0.04 m confidence interval. Upslope areas were less suitable for crop growth due to high rates of tillage erosion and poor soil structure with the lowest corn yields in topographic shoulders and highest corn yields on backslopes and flats. Footslopes had the most variable crop yields due to high rates of water erosion; ephemeral gullies and large depositional plumes hindered seedling development at points of topographic convergence and at catch basins.

While we offer a novel approach using very-high resolution UAV imagery and SfM-MVS to estimate soil erosion and assess the effectiveness of catch basins, similar research is needed pre and post application of tile drainage, surface inlets, and other best management practices. These efforts would enable the quantification of how effective individual best management practices perform at reducing soil erosion and improving water quality compared to sites without any management practices. Future research needs to provide a holistic evaluation of these agricultural management practices by quantifying both sediment and agro-chemical export (e.g., phosphorus) via overland flow and subsurface drainage. Quantifying the relative impacts of different best management practices is not only of scientific interest, but also plays a critical role in management decisions and the generation of policy and incentivizing its adoption. In this study we demonstrated that the simple installation of soil berms at field-edge can effectively eliminate the overland connectivity of eroded sediments from waterways and offers a practical and effective action towards improving water quality in the region.

Chapter 4. Agricultural erosion modelling: Evaluating USLE and WEPP field-scale erosion estimates using UAV time-series data

As published in Environmental Modelling & Software: Meinen, B. U., & Robinson, D. T. (2021). Agricultural erosion modelling: Evaluating USLE and WEPP field-scale erosion estimates using UAV time-series data. Environmental Modelling & Software, 137, 104962. Doi: 10.1016/j.envsoft.2021.104962

4.1. Introduction

Soil erosion in agricultural systems is a pressing issue for water quality (Bennett et al., 2001; Michalak et al., 2013) and agricultural sustainability (Pimentel 2006; FAO 2015; Montanarella 2015). Soil erosion accounts for 75 billion tons of soil loss annually from arable land (ELD Initiative, 2015) resulting in a median productivity loss of 0.3% of crop yield per year (FAO 2015) with an estimated global economic impact of 400 billion USD per year (ELD Initiative, 2015). These trends are likely to be exacerbated as the demand for agricultural products continues to increase (Tilman et al., 2011) while highly productive cropland is lost to urban growth (estimated 1.8–2.4% by 2030; d'Amour et al., 2017) and accelerated soil erosion processes from conventional agriculture (n = 448, median 18 t ha^{-1} yr^{-1}; Montgomery 2007) continue to degrade arable land. Limited space for agricultural expansion has resulted in the expansion of agricultural cropland into marginal and highly erodible landscapes (e.g., forested tropics; Foley et al., 2011), re-expansion into erodible agricultural landscapes that were previously taken out of production (e.g., conservation reserve program in the United States; Bigelow et al., 2020), and the conversion of less productive land (e.g., summer fallow, pasture) into cropland (e.g., Canada; Statistics Canada 2017). Between 1985 and 2005 there was a global net increase of 2.41% of cropland area into these highly erodible landscapes (Foley et al., 2011). Within this context of agricultural land scarcity and the demand for agricultural products estimated to double by 2050 (Foley, 2011), soil erosion, agricultural production, and sustainable land management will continue to be a critical global issue throughout the 21st century.

Predicting the magnitude of soil loss in agricultural systems is a difficult environmental modelling problem. Part of this difficulty resides in the fact that an agricultural system is a coupled human-natural system, whereby both systems are highly heterogeneous (e.g., natural – weather, soil; human – cropping practices, land management) and interactive. Given this complexity, some have conceptually described agricultural systems as being stochastic since seemingly identical agricultural systems can have widely different hydrologic responses (e.g., variability in replicate plots; Wendt et al., 1986; Nearing et al., 1999). Even when agricultural systems produce a similar

hydrologic response, sediment delivery is mediated by highly heterogeneous parameters (e.g., microtopography from tillage, tile drainage, riparian buffer strips), leading to a poor relationship between erosion rates, soil loss from fields, and sediment yield in waterways. Despite continued improvements in our understanding of edaphic processes and computational modelling, decades of research continue to note that the predictive capabilities of soil erosion models are often quite poor (Takken et al., 1999; Favis-Mortlock et al., 2001; Jetten et al., 2003; Evans and Brazier 2005; Morgan and Nearing 2011; Evans 2013) and that “erosion modelling is very error prone” (Jetten et al., 1999, p. 537). This high degree of error and the inherent complexity of these human-natural systems necessitates the need for testing and validating model predictions.

The advent of process-based erosion models has increased the potential for modelling soil erosion in any agricultural system without rigorous calibration and validation. However, both empirical and process-based models rely on statistical relationships that need to be tested and validated against in-situ soil erosion measurements. Testing the predictions of erosion models can be difficult when you consider that soil erosion measurements have a considerable amount of uncertainty associated with them (Stroosnijder 2005) and that the scales of measurement rarely correspond to the scales of natural and human processes driving erosion. It is unlikely that the process domains driving erosion can be elucidated using aspatial outlet-based measurements (e.g., sediment yield; Borrelli et al., 2014) or with spatially-distributed isotopic tracer measurements (e.g., caesium-137; Walling et al., 2003). Remote sensing (e.g., airborne imagery; Fischer et al., 2018) and field-based methods (e.g., measuring rills and gullies; Takken et al., 1999) provide some understanding of the dominant process domains contributing to soil erosion, but they are constrained by spatial scale, accuracy, and the repeatability of measurements.

The disconnect between process domains that are measured and modelled is one of the biggest obstacles for testing and validating model predictions of soil erosion. For example, consider an outlet-based method of measuring sediment yield for evaluating model predictions of soil loss. The sediment yield subsumes all processes in a catchment (i.e., all sediment sources and delivery mechanisms) to produce a single aspatial number. Even if the modelled results accurately predict sediment yield at the catchment outlet, the issue of equifinality cannot be addressed: are the models getting the right answer for the right reasons? Without a spatial component included in the evaluation process, the model may have a completely erroneous representation of the internal catchment dynamics while still producing a correct outlet response (Van Oost et al., 2005). The challenges of equifinality can only begin to be addressed if distributed data is used to ensure the model is behavioral (Jetten et al., 2003). Unfortunately, spatial

measurements of soil erosion are labor intensive, expensive, and time consuming; as such, they are seldom used for evaluating models (Morgan and Nearing 2011). Stroosnijder (2005) concludes a critical review on soil erosion measurements stating there is a “crisis in erosion measurements” (p. 172) due to poor empirical data and no new developments in technology for measuring soil erosion.

The democratization of unmanned aerial vehicles (UAVs; also known as remotely piloted aircraft systems [RPAS]) and automated photogrammetric workflows (i.e., Structure-from-Motion [SfM]) herald a new advancement in remote sensing technology for measuring distributed soil erosion rates. The potential of these novel technologies to accurately measure soil erosion is recognized in literature but they have yet to be used for testing erosion models (Batista et al., 2019). The very-high resolution (<5 cm), frequent, and event-based quantitative measurements of distributed erosion from UAVs (Chapter 3; Meinen and Robinson 2020c) can be used to create a time series of erosion data at a spatial scale that has not been previously achievable. These data provide an opportunity to evaluate soil erosion models in a spatially distributed manner at the scale in which agricultural decisions take place (i.e., farm field). In addition to quantitative measurements, optical imagery of erosional features can be used as an additional ‘soft’ qualitative datapoint for model evaluation (Jetten et al., 1999). While there still remain challenges in creating high-fidelity data with SfM for change-detection measurements (Chapter 2; Meinen and Robinson 2020b), the combination of qualitative and quantitative erosion measurements provides a strong baseline for evaluating the performance of erosion models.

To advance the field of erosion modelling, we collected novel very-high resolution time-series data using a UAV for the purpose of quantifying semi-distributed rates of soil erosion over an entire year. We used these data to determine: what is the accuracy of an empirically-based (Universal Soil Loss Equation [USLE]; Wischmeier and Smith 1978) and a process-based (Water Erosion Prediction Project [WEPP]; Flanagan and Nearing 1995) erosion model at estimating soil erosion rates on an agricultural field in southwestern Ontario, Canada? The performance of the USLE and WEPP were evaluated on both an annual and sub-annual basis against UAV-based measurements of soil erosion.

4.2. Materials and methods

4.2.1. Study site

Our study site is an agricultural field located in the upper reaches of the Nith Watershed, Ontario, Canada. The Nith watershed spans an area of 1130 km^2 with 80% of its total land area devoted to agricultural production (Loomer and Cooke 2011). The Nith Watershed is characterized by high

rates of runoff and pollutant loading during the spring freshet (Loomer and Cooke 2011) with peak precipitation occurring in the latter half of the growing season. The Nith Watershed has been identified as a priority sub-watershed of the Grand River Watershed due to its large contribution of phosphorus, nitrogen, and suspended sediments to the Grand River (Holeton 2013). The Grand River flows southwards into Lake Erie, which continues to face the harmful effects of eutrophication and algae blooms caused by elevated levels of phosphorus originating from diffuse agricultural sources (Michalak et al., 2013).

The agricultural field used for measuring, modelling, and evaluating predictions of soil erosion is part of a heterogeneous agricultural system that is uniquely characterized by snowmelt and a dense tile-drainage network. The field is a steep 15.9-ha tile-drained agricultural field under a 3-year crop rotation of corn, soybean, and winter wheat (Fig. 4.1), which is a common rotation for southern Ontario. The chosen study year for field work spans from corn cultivation in 2018 to the spring of 2019. The field management regime consists of a fall moldboard plow following corn and oats, a spring cultivator for seedbed preparation for corn and soybeans, no-till winter wheat, and broadcast oats as a cover crop after winter wheat (Fig. 4.1). The study site had tile-drainage installed in the winter of 2017–2018; the tile installation was accompanied by an installation of soil berms and surface inlets at six locations that form catch basins to trap eroded sediments (Fig. 4.2). Soils on the study site are texturally classified as a mix of sandy loam and loam.

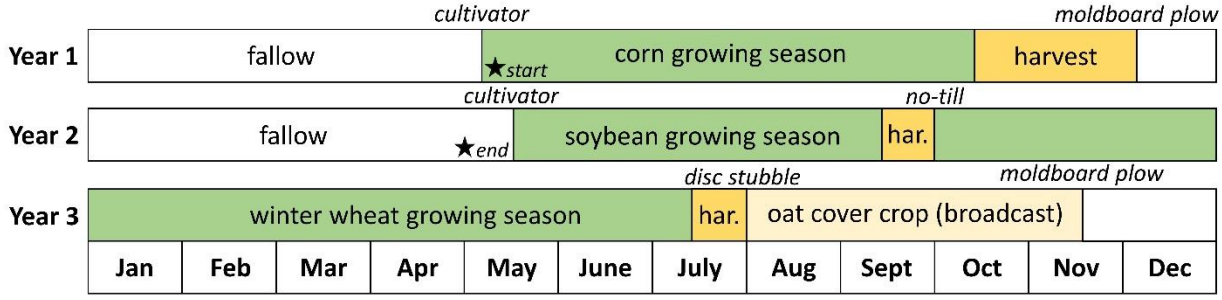

Fig. 4.1. Long-term management practices and crop rotations for the study site. Stars indicate the period in which soil erosion measurements were conducted for model evaluation (May 17, 2018 to May 16, 2019).

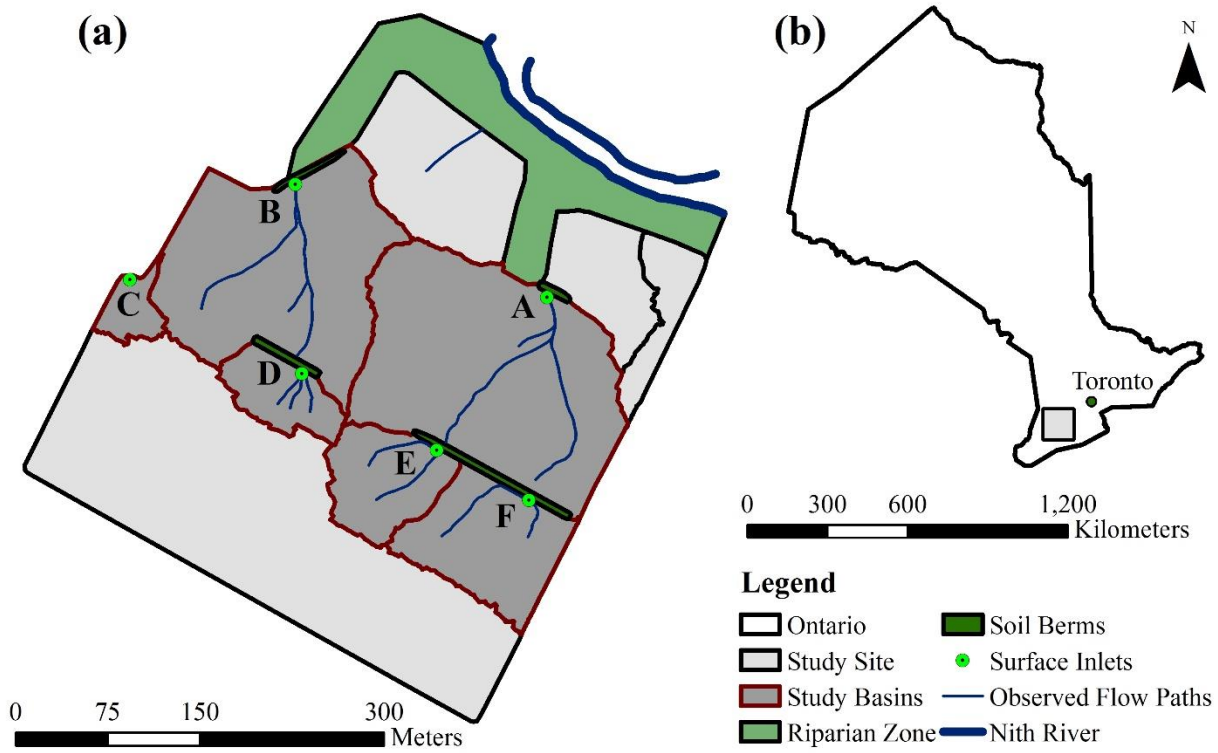

Fig. 4.2. (a) Agricultural study site, and (b) approximate location of study site in southwestern Ontario, Canada. Flow paths are mapped with UAV optical imagery based on the 2018 growing season.

4.2.2. Data

Our data collection is focused on six distinct drainage basins with soil berms and surface inlets (i.e., catch basins) outlined in Fig. 4.2 (i.e., Basins A, B, C, D, E, and F) for measuring and evaluating model estimates of soil loss by water erosion. All field work was carried out by Meinen and Robinson (2020c; Chapter 3) from May 17, 2018 to May 16, 2019 when the study site was under corn production. A comprehensive UAV surveying methodology for the study site can be found in Meinen and Robinson (2020c; Chapter 3) with a discussion on UAV flight design in Meinen and Robinson (2020b; Chapter 2).

4.2.2.1. Field work

The modelling of erosion in agricultural systems requires a representation of the following five factors: climate, soils, topography, vegetation, and land management. Our climate data consists of hourly precipitation data collected from a meteorological station (Wellesley Dam) located 7 km from the study site. Soil data included average soil texture, measured with a sieve and hydrometer analysis on 27 soil samples (15 cm depth; Menzies-Pluer et al., 2020), and bulk density, measured using bulk density rings on 16 soil samples (15 cm depth) that were dried in a conventional oven

at 105° Celsius for 24 h and weighed. Topographic data was calculated from a digital elevation model (DEM) created with optical imagery collected from a UAV and SfM. The raw data were collected at a resolution of 0.02 m and used to create a 0.02 m DEM, which was resampled to generate a 0.8 m DEM for catchment discretization and resampled to 3.2 m for calculating primary terrain variables (i.e., hillslope length, width, and slope). All topographic calculations were done using ArcGIS v10.6.1. Cropping and management practices were provided by the landowner (Fig. 4.1) and crop stages were determined from in-situ site surveys.

To model erosion using the USLE and WEPP, our six study basins (Fig. 4.2) were discretized into rectangular hillslopes (Table 4.1) and segmented into 3–5 overland flow elements to capture the hillslope shape. Rectangular hillslopes were segmented such that a hillslope constituted the point from where overland flow began to where either the slope gradient decreased such that deposition began or where the runoff entered a concentrated flow channel (e.g., an ephemeral gully).

Table 4.1. Six study basins and hillslope topographic attributes. Each hillslope is further divided into 3 - 5 overland flow elements.

Basin	Number of Hillslopes	Slope (percent)	Length (m)	Width (m)
A	3	9.00, 8.53, 8.63	58, 152, 113	149, 42, 157
B	3	8.57, 9.22, 9.97	76, 133, 72	170, 32, 135
C	1	3.70	56	37
D	1	6.68	48	97
E	1	6.46	85	88
F	1	6.71	102	106

4.2.2.2. UAV erosion measurements

The creation of a dataset for evaluating model estimates of soil erosion involved using a novel remote sensing approach to monitor surface change in each catch basin with optical imagery collected from a UAV and SfM (Chapter 3; Meinen and Robinson 2020c). Across the study year, a total of nine surveys were conducted to recreate the topography of each catch basin and to generate orthomosaics (Fig. 4.3). The M3C2 algorithm (Lague et al., 2013; 0.15 m projection, vertical normals) was used in CloudCompare v2.9.1 (https://www.danielgm.net/cc/) to calculate surface change (i.e., deposition) in each of the six catch basins using pointcloud data. Volumetric surface change was converted to a weight using an average measured soil bulk density of 1.32

g/cm3. Across the entire study year, a total of 159.52 tonnes of sediment was deposited across the six catch basins (Table 4.2), corresponding to an erosion rate of 18.83 t ha^{-1} yr^{-1}.

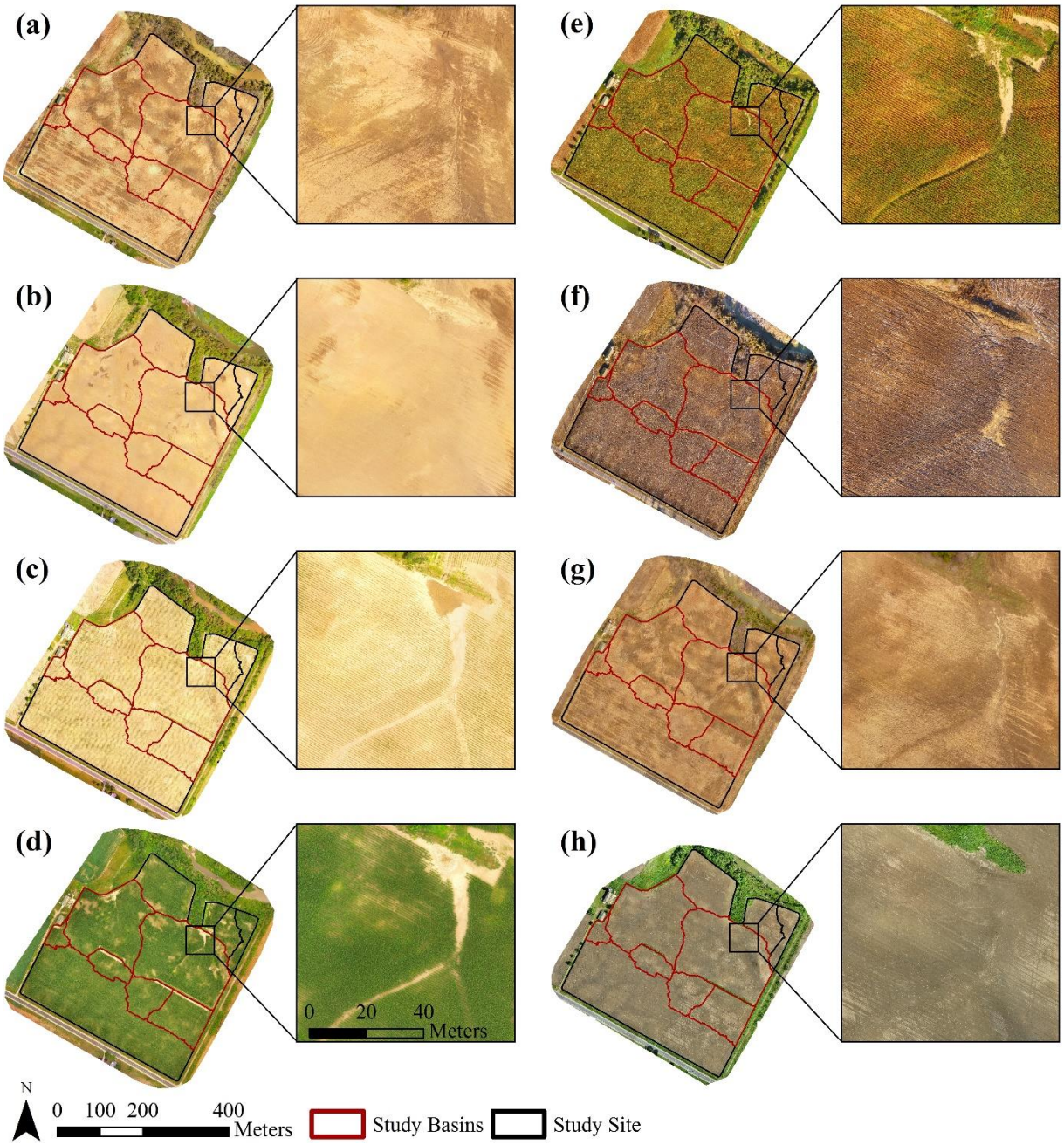

Fig. 4.3. UAV orthomosaics of the study site: (a) May 7, 2018, (b) May 17, 2018, (c) June 15, 2018, (d) July 14, 2018, (e) September 19, 2018, (f) December 18, 2018, (g) April 25, 2019, and (h) June 14, 2019. Zoomed in extent boxes are focused on Catch Basin A.

Table 4.2. UAV-based erosion measurements and associated climate data from May 17, 2018 to May 16, 2019 split into three time periods: growing season (GS), mature crop/stubble (MC, S), and fallow (F). Total precipitation includes both rainfall and the water equivalent of snowfall. Corn was planted on May 13, 2018, harvested on November 11, 2018, and the field was plowed on December 10, 2018.

Study Period	Total precipitation (mm)	Rainfall events >5 mm h^{-1}	Average daily air temperatures (°C)	Erosion (t)
May 17 to Sept 19 (GS)	376.4	12	19.6	136.40
Sept 20 to Dec 17 (MC, S)	234.8	3	4.1	0*
Dec 18 to May 16 (F)	387.6	5	-1.3	23.13
Totals:	998.8	20	7.3	159.52

*value is estimated, not measured; no UAV surveys were conducted. In-situ site observations indicated no erosion occurred

4.2.3. Erosion modelling

4.2.3.1. Universal Soil Loss Equation (USLE)

Research on soil erosion in North America began in the early 20th century (e.g., Zingg 1940; Smith 1941; Musgrave 1947) and was accelerated after Franklin Roosevelt helped pass the Soil Conservation Act of 1935 (Public Law 74–46). To fulfil the requirements of this act, the United States Department of Agriculture and the newly created Soil Conservation Services developed the Universal Soil Loss Equation (USLE) in the 1950's as a tool to predict soil loss and help farmers with conservation planning. The USLE is a lumped empirical field-scale model that predicts soil loss from rill and inter-rill erosion based on 10,000 plot years of erosion data. The USLE was originally published in Agricultural Handbook no. 282 (Wischmeier and Smith 1965) and adopted widely based on the superseding publication in Agricultural Handbook no. 537 (Wischmeier and Smith 1978). The USLE is expressed as:

$$A = \sum_{n=1}^{6} RKLSC_n P$$

where A is the soil loss per unit area (t ha^{-1} yr^{-1}), which is the sum of the products of six factors for six cropstages, n, whereby R is a rainfall and runoff factor (MJ mm ha^{-1} h^{-1} yr^{-1}), K is a soil erodibility factor (t ha h ha^{-1} MJ^{-1} mm^{-1}), L is a slope-length factor (unitless), S is a slope-steepness factor (unitless), C is a cover and management factor (unitless), and P is a supporting practice factor (unitless; Wischmeier and Smith 1978). These six factors combine human-decision making and the predominant natural processes contributing to soil loss in an agricultural landscape.

The USLE is the de-facto standard for erosion modelling due to its simplicity and ease-of-use. The USLE and its many derivations (e.g., revised USLE; Renard et al., 1991, modified USLE; Williams 1975) are incorporated into erosion estimates in a wide variety of models: Areal Nonpoint Source Watershed Environment Response Simulation (ANSWERS; Beasley et al., 1980), Field-scale Model for Chemicals, Runoff, and Erosion from Agricultural Management Systems (CREAMS; Knisel 1980), Erosion-productivity Impact Calculator (EPIC; Williams 1989), Agricultural non-point Source Model (AGNPS; Young et al., 1989), Soil and Water Assessment Tool (SWAT; Arnold 1994), Sediment Delivery Distributed Model (SEDD; Ferro and Porto 2000), and the Water and Tillage Erosion Model/Sediment Delivery Model (WATEM/SEDEM; Van Rompaey et al., 2001).

For this study, all USLE calculations are based on Agricultural Handbook no. 537 (Wischmeier and Smith 1978). The R factor was calculated using hourly-precipitation data from the Wellesley dam meteorological station using the follow equation (Wischmeier and Smith 1978):

$$R = \sum_{i=1}^{m} (EI_{30})_i$$

where EI_{30} is the rainfall erosivity of a single storm event (MJ mm ha^{-1} h^{-1}), i, calculated as the total kinetic storm energy (E; MJ ha^{-1}) times the maximum 30-min rainfall intensity (I30; mm h^{-1}) for all storms in a given year, m. Storms are only included in the calculation of R that exceed 12.7 mm of rainfall in a 6-hour period. An additional sub factor R_s can be included to account for the effects of winter runoff and snowmelt on soil loss; we chose to exclude R_s from our soil loss calculations since we observed in the previous year that snowmelt produced no observable amount of erosion (Fig. 4.3a). Since the USLE requires 30-min rainfall intensities for calculating the I30, our calculated R factor likely underpredicted storm intensity. To correct for this underprediction, we used a relationship developed by Panagos et al. (2015b) to convert from 60-min intensities to 30-min intensities by multiplying our R factor by 1.5597.

The K factor was calculated using field-based measurements of soil texture (i.e., 34.82% silt, 13.27% clay) and estimates of edaphic properties (i.e., 2% organic matter, b = 2, c = 3) based on the following equation for soils containing less than 70% silt and very fine sand (Wischmeier and Smith 1978):

$$100K = (2.1M^{1.14}(10^{-4})(12 - a) + 3.25(b - 2) + 2.5(c - 3)) \times 0.1317$$

where K is the soil erodibility factor (t ha h ha^{-1} MJ^{-1} mm^{-1}), M is the soil particle-size parameter (based on soil texture), a is percent organic matter, b is the soil-structure code, and c is the profile-permeability class. Organic matter in the topsoil on the study site was estimated to be lower than regional averages (~4%) due to a tile drainage installation in the previous winter which inverted a large portion of the soil column. The L and S factors are typically jointly calculated as the following (Wischmeier and Smith 1978):

$$LS = (\lambda/22.13)^{m}(65.41\ sin^2\ \theta +\ 4.56 \sin\theta + 0.065)$$

where LS is the slope length factor (unitless), λ is slope length (m), θ is the angle of the slope (degrees), and m is an exponent based on slope gradient (see Table 4.1 for hillslope topographic attributes). The C factor and corresponding soil loss ratios (SLRs) were calculated using the tables provided in Agricultural Handbook no. 537 for high productivity corn with a fall moldboard plow (Table 4.3). No additional management practices were represented on our study site, so the P value was initialized to a value of 1 (unitless), representing no net effect on soil erosion.

Table 4.3. USLE modelling parameters for the six study basins used for calculating soil loss from May 17, 2018 to May 16, 2019. SLR is the soil loss ratio for the corresponding cropstage. R value: 1881 MJ mm ha^{-1} h^{-1} yr^{-1}, K value: 0.026 t ha h ha^{-1} MJ^{-1} mm^{-1}, P value: 1, LS value: 1.80 (full site: 1.38), and C value: 0.310.

Start Date	Cropstage Period	Cover (%)	EI in period (%)	SLR	C value
May 13, 2018	(SB) Seedbed	0	2.5	0.65	0.016
May 27, 2018	(1) Establishment	10	7.3	0.53	0.039
July 4, 2018	(2) Development	50	22.1	0.38	0.084
July 31, 2018	(3) Maturing crop	>75	53.2	0.20	0.106
Nov 11, 2018	(4) Stubble	Variable	0.7	0.23	0.002
Dec 10, 2018	(F) Rough fallow	0	14.2	0.44	0.063

4.2.3.2. Water Erosion Prediction Project (WEPP)

In 1985, the United States Department of Agriculture started research on a process-based successor to the USLE, the Water Erosion Predict Project (WEPP; Laflen et al., 1991; Flanagan and Nearing 1995). The WEPP was developed using data from 50 experimental cropland (Laflen et al., 1991) and rangeland plots (Gilley et al., 1990) to accurately model the underlying hydrologic processes that contribute to soil erosion. These processes are represented in the model using "stochastic weather generation, infiltration theory, hydrology, soil physics, plant science,

hydraulics and erosion mechanics" (Flanagan and Nearing 1995, p. 1.1). The WEPP is a daily simulation model that computes soil loss and sediment delivery from rill and inter-rill erosion for individual hillslopes or small watersheds (Flanagan and Nearing 1995). The WEPP erosion routine is based on a steady-state sediment continuity equation that describes the movement of soil in rills:

$$\frac{dG}{dx} = D_f + D_i$$

where x is the distance downslope (m), G is the sediment load (kg s^{-1} m^{-1}), D_f is the rill erosion rate (kg s^{-1} m^{-2}), and Di is the inter-rill sediment delivery to rills (kg s^{-1} m^{-2}). Erosion is conceptualized as a series of inter-rill areas that deliver sediment to concentrated flow channels (i.e., rills) that is either deposited in the rill or transported off the hillslope. For this study, WEPP model calculations are based on WEPP version 2012.800 using the Windows interface (Table 4.4 input parameters). For modelling, CLIGEN was used to convert daily climate data (i.e., precipitation and temperature) into more temporally detailed distributions for soil loss and runoff calculations.

Table 4.4. WEPP input parameterization for calculating soil loss from May 17, 2018 to May 16, 2019. Topographic data is summarized in Table 4.1.

	Management/Field Conditions
Soils	Loam & Sandy Loam
	Texture (average): 34.82% silt, 13.27% clay, 51.91% sand
	Miscellaneous: 5% granular, 2% organic matter*, 12.5 CEC* (meq 100 g^{-1}), 0.25 albedo*, Inter-rill erodibility**, rill erodibility**, critical shear**, effective hydraulic conductivity**
Management	Pre-management: After fall moldboard plow
	(May 12, 2018) Cultivator: 7.5 cm depth (2 passes)
	(May 12, 2018) Nutrient (N, P, K, liquid fertilizer) and herbicide application
	(May 13, 2018) Planting: corn, row width: 0.75 m, crop spacing: 0.15 m
	(June 16, 2018) Nutrient (N) and herbicide application
	(Nov 11, 2018) Harvest: residue height: 0.30 m, crop yield: 12.09 t ha^{-1}
	(Dec 10, 2018) Moldboard plow: 15 cm depth
	(June 8, 2019) Cultivator: 7.5 cm depth (2 passes)
	(June 9, 2019) Planting: soybean
Tile Drainage	Drain spacing: 7.6 m, tile depth: 0.91 m, pipe diameter: 0.1 m
	Drainage coefficient: 0.5*
Weather	Daily precipitation (annual sum): 998.8 mm
	Daily air temperature (mean ± one SD): 7.25 ± 11.18 °C
	Temperature range (min/max): -26.10 to 33.90 °C

*estimated **calculated by WEPP

4.2.4. Analysis

We focus on the six distinct drainage basins with soil berms and surface inlets (i.e., Basins A, B, C, D, E, and F; Fig. 4.2) for evaluating model estimates of soil erosion. For the purposes of this study, we define the rate of soil erosion as soil loss by water erosion to catch basins per unit area. USLE results are computed as soil loss per unit area (i.e., soil loss from an individual hillslope) and WEPP results are computed as sediment delivery per unit length (i.e., kg m^{-1}) and multiplied by the hillslope width to convert into soil loss per unit area for comparing modelled results. Both model outputs reflect soil loss by water erosion from a hillslope to the lowest point in the catchment (i.e., the catch basin). The USLE and WEPP were used to estimate rates of soil erosion in each of the six catch basins on an annual and sub-annual (i.e., seasonal) basis.

For evaluating the USLE and WEPP, we conducted a “blind evaluation” (Batista et al., 2019, p. 4) whereby the USLE and WEPP were parameterized and soil erosion estimates were compared to UAV-based measurements of soil erosion for the 2018–2019 study year; no calibration procedure was conducted. Measured rates of soil erosion were compared to model estimates of soil erosion for all six catch basins and evaluated based on the absolute magnitude of error, percent error, and Nash-Sutcliffe model efficiency (NSE; Nash and Sutcliffe 1970):

$$NSE = 1 - \frac{\sum_{i=1}^{n}(Q_m - Q_p)^2}{\sum_{i=1}^{n}(Q_m - \bar{Q}_m)^2}$$

where Q_m is the measured soil loss, $\bar{Q}_m$ is the mean of measured soil loss, and Q_p is the modelled soil loss. NSE values range from -∞ to 1, with a NSE of 1 corresponding to a perfect match between measurements and model predictions, a NSE of 0 indicates that the modelled soil loss is as accurate as the mean of the measurements, and a NSE of less than 0 indicates that the mean of measurements is a better predictor than the erosion model.

For comparing the percent error between measured and modelled results, we assume the erosion model has reached the upper limit of predictive accuracy if results are within 20% of measured values (based on the average coefficients of variation from the replicate erosion plots of Wendt et al., 1986). UAV-based measurements of soil erosion are assumed accurate for the purposes of model evaluation, but we include the uncertainty metrics of Meinen and Robinson (Chapter 3; 2020c) in our results. Measurements of soil erosion had an average uncertainty of 29% (based on a ±0.04 m confidence interval for M3C2 surface change calculations). Soil erosion measurements likely underestimate actual erosion rates since sediment was lost into the surface inlets, i.e., the depositional plumes in the catch basins used for measuring soil erosion rates were not representative of all the eroded sediments; the exact volumetric amount of sediment lost into the subsurface drainage network is not known.

4.3. Results

4.3.1. Model evaluation

Erosion model estimates were compared to UAV-based erosion measurements for each of the six study basins on both an annual (Table 4.5) and sub-annual basis (Table 4.6). On an annual basis, the total cumulative erosion rate (i.e., soil loss by water erosion to catch basins per unit area) for all six study basins was measured at 18.83 t ha^{-1} yr^{-1}. The USLE overestimated the erosion rate at 26.23 t ha^{-1} yr^{-1}, whereas the WEPP underestimated the erosion rate at 16.41 t ha^{-1} yr^{-1} (Table 4.5). Assuming a natural stochastic variation of 20% in soil erosion rates (i.e.,

3.77 t ha^{-1} yr^{-1}), only the aggregated results of WEPP are within the upper limit of annual predictive accuracy.

At the semi-distributed basin scale, both the USLE and WEPP exhibited a higher range of variability with errors exceeding 20% when compared to annual UAV-measured values (Table 4.5). The absolute average magnitude of error of soil erosion estimates for the six catch basins were 7.36 t ha^{-1} yr^{-1} and 4.09 t ha^{-1} yr^{-1} for the USLE and WEPP, respectively. WEPP estimates of soil erosion were more accurate than the USLE for each basin, with the exception of Basin D. The soil erosion rate of Basin D was unexpectedly high considering its moderate slope and small size. The five other basins had a closer agreement between measured and modelled soil loss using the WEPP model and fell within or close to the upper limit of predictive accuracy. The USLE had a strong tendency to overestimate soil erosion rates for the study site, whereas the WEPP had a moderate underestimation of soil erosion rates.

Table 4.5. Annual UAV-based erosion measurements and modelling estimations. Basin-level WEPP efficiency (NSE: 0.97), basin-level USLE efficiency (NSE: 0.56).

Basin	Area (ha)	Measured soil loss (t)	USLE soil loss (t)	USLE (% error)	WEPP soil loss (t)	WEPP (% error)
A	3.27	68.70 ± 15.67	99.84	45	63.29	8
B	2.69	53.64 ± 11.62	79.52	48	46.20	14
C	0.22	0.00 ± 0.00	1.50	N/A	0.88	N/A
D	0.48	10.52 ± 4.24	6.21	41	4.56	57
E	0.73	10.46 ± 3.57	13.10	25	7.92	24
F	1.09	16.20 ± 7.20	22.34	38	16.37	1
TOTAL:	**8.48**	**159.52**	**222.50**	**39**	**139.22**	**13**

Sub-annual estimates of soil erosion (Table 4.6) compared to UAV-measured values showed a much larger discrepancy between models than was observed at the annual temporal scale. The total cumulative erosion rate for all six study basins showed a strong seasonal dependency, with a measured soil loss of 16.08 t ha^{-1}, 0.00 t ha^{-1}, and 2.73 t ha^{-1} for the growing season, mature crop/stubble, and fallow winter periods, respectively. The USLE estimated a soil loss of 20.06 t ha^{-1}, 0.87 t ha^{-1}, and 5.30 t ha^{-1} while the WEPP estimated a soil loss of 14.06 t ha^{-1}, 0.02 t ha^{-1}, and 2.34 t ha^{-1} for the three respective periods. The aggregated, i.e., field-scale,

sub-annual results of the WEPP are within the upper limit of predictive accuracy (i.e., ± 20% measured values) while the USLE had a moderate overestimation of soil loss for all three periods.

At the semi-distributed basin scale (Table 4.6), the USLE and WEPP once again exhibited a high range of variability, with the WEPP outperforming the USLE for sub-annual estimates. The absolute average magnitude of error for the six catch basins for the three respective time periods was 5.33 t ha^{-1}, 0.65 t ha^{-1}, and 2.47 t ha^{-1} for the USLE (overall: 2.82 t ha^{-1}) and 4.18 t ha^{-1}, 0.01 t ha^{-1}, and 1.08 t ha^{-1} for the WEPP (overall: 1.76 t ha^{-1}). The USLE had a sub-annual NSE of 0.80, exhibiting an overestimation of soil loss for most basins, while the WEPP had a sub-annual NSE of 0.96 with a close agreement between UAV-measured values and estimated soil loss.

Table 4.6. Sub-annual UAV erosion measurements and modelling estimates: growing season (GS), mature crop, stubble (MC, S), and fallow (F). Basin-level WEPP efficiency (NSE: 0.96), basin-level USLE efficiency (NSE: 0.80).

Basin	Study Period	Measured soil loss (t)	USLE soil loss (t)	USLE (% error)	WEPP soil loss (t)	WEPP (% error)
A	GS	61.32 ± 14.18	76.36	25	53.91	12
B	GS	39.40 ± 9.12	60.82	54	39.70	1
C	GS	0.00 ± 0.00	1.14	N/A	0.88	N/A
D	GS	10.52 ± 4.24	4.75	55	4.29	59
E	GS	10.18 ± 3.48	10.02	2	7.09	30
F	GS	14.97 ± 6.88	17.09	14	13.38	11
Total:		**136.39**	**170.17**	**25**	**119.25**	**13**
A	MC, S	0.00 ± 0.00	3.30	N/A	0.09	N/A
B	MC, S	0.00 ± 0.00	2.63	N/A	0.11	N/A
C	MC, S	0.00 ± 0.00	0.05	N/A	0.00	0
D	MC, S	0.00 ± 0.00	0.21	N/A	0.01	N/A
E	MC, S	0.00 ± 0.00	0.43	N/A	0.00	0
F	MC, S	0.00 ± 0.00	0.74	N/A	0.00	0
Total:		**0.00**	**7.36**	**N/A**	**0.21**	N/A
A	F	7.38 ± 1.49	20.18	173	9.39	27
B	F	14.24 ± 2.50	16.07	13	6.39	55
C	F	0.00 ± 0.00	0.30	N/A	0.00	0
D	F	0.00 ± 0.00	1.25	N/A	0.26	N/A
E	F	0.28 ± 0.09	2.65	846	0.83	196
F	F	1.22 ± 0.32	4.52	270	2.99	145
Total:		**23.12**	**44.97**	**95**	**19.86**	**14**

4.4. Discussion

4.4.1. Model evaluation

An ongoing challenge in erosion modelling is recognizing the scale-dependency of input parameters and ensuring that a model is correctly parameterized at the spatial (e.g., hillslope, field, watershed) and temporal scale (e.g., annual, sub-annual) of interest. The model user makes

the subjective choice on the spatial and temporal scales to measure, estimate, and interpolate input parameters. Given the same objectives, different users will likely conceptualize and parameterize an agricultural system differently. A simple blind model evaluation whereby an erosion model is parameterized, run, and compared to real measurements of soil loss increases the model user's confidence that the correct parameter set was chosen and that the model is appropriate for the climate, soils, topography, cropping system, and land management practices of the system being studied.

The semi-distributed model evaluation of the USLE yielded accurate relative estimates of soil loss (e.g., Basin A was responsible for approximately 43 - 45% of total annual soil loss), but overestimated soil loss during each cropstage and subsequently overestimated annual soil loss (NSE: 0.56). Analysis of the cropstage USLE results demonstrated that this overestimation may have been a result of inadequate model input data rather than model error. The I_{30} calculated for the "establishment" and "fallow" cropstages was likely too high; the hourly-rainfall intensities converted to 30-minute intensities did not correctly characterize the intensity of the most erosive storms. The less accurate short-term estimates produced by the USLE are likely expected by practitioners with experience using the USLE, whereby long-term average (i.e., 20 - 22 years) estimates of soil loss are expected to be more accurate. However, the USLE was originally intended to be used for both long-term and short-term predictions of soil erosion. Wischmeier and Smith (1978) state in Handbook No. 537 that "with appropriate selection of its factor values, the equation will compute the average soil loss for a multi-crop system, for a particular crop year in a rotation, or for a particular cropstage period within a crop year" (p. 3), with the caveat that the equation will be "substantially less accurate" (p. 4) for predicting individual storm events compared to long-term averages.

The structure of the USLE does not explicitly include runoff or seasonal temperature changes, so short-term (i.e., cropstage, 1-year annual) predictions of soil loss in regions characterized by high temporal variability in temperatures with intermittent snowmelts will likely be worse than long-term predictions. While the USLE includes a subfactor for thaw and snowmelt (R_s), since erosion plots used in the model development were located in the Midwest and Pacific Northwest United States, the relationship is a single multiplicative factor of 1.5 times the December through March precipitation. This relationship may relate well to the conditions of the Pacific Northwest whereby "… as much as 90 percent of the erosion on the steeply rolling wheat land has been estimated to derive from runoff associated with surface thaws and snowmelt "(Wischmeier and Smith 1978, p. 7), but does not necessarily relate to the conditions of other

winter climates. We intentionally chose to exclude the R_s sub factor from our study based on observations from the previous year (2017–2018 winter) where snowmelt produced no observable amount of erosion (Fig. 4.3a); including the R_s sub factor would have increased our error in the fallow cropstage from 95% to 268%. The overestimation of winter soil loss may have also been exacerbated as a result of the soil loss ratio being too high for the "stubble" and "rough fallow" cropstages since frozen soils mediated erosional processes and snow melt produced very little soil erosion.

Our semi-distributed evaluation of the WEPP provided insights into the applicability of the WEPP for the conditions of our agricultural study site. The WEPP had accurate annual (NSE: 0.97) and sub-annual predictions (NSE: 0.96) indicating that we correctly parameterized the model with our in-situ measurements, estimations, and the parameters that we let WEPP calculate from its database. The WEPPs process-based modelling structure and incorporation of temporally-distributed management practices (e.g., tillage), plant science (e.g., crop growth), and hydrology (e.g., snowmelt and associated runoff) on a daily timestep allowed it to accurately model the seasonal dynamics of southwestern Ontario. Although the WEPP had a tendency to underpredict soil erosion rates, aggregated field-scale estimates of soil erosion were within the upper limit of predictive accuracy.

While our UAV-based evaluation approach and application to the climatic conditions in southwestern Ontario are novel, the general findings of our study corroborate existing literature. Both the USLE and WEPP model evaluations demonstrated that: (1) annual estimates of soil erosion are more accurate than sub-annual estimates (e.g., Jetten et al., 1999), and (2) aggregated field-scale estimates of soil erosion are more accurate than individual hillslope or basin estimates (e.g., Jetten et al., 2003; model error increases as the spatial resolution of predictions becomes finer). The stochastic variation in soil erosion rates is most pronounced at fine spatial and temporal scales (e.g., hillslopes); coarse scales, e.g., full farm fields, allow the model to have an averaging effect whereby overestimations and underestimations balance each other out. The USLE and WEPP have been found to have similar annual predictive capabilities (Tiwari et al., 2000; Laflen et al., 2004), albeit with a high range of error. At shorter time scales the WEPP was specifically designed to replace the USLE by improving short-term soil loss estimates by a process-based representation of climate and hydrology (Flanagan and Nearing 1995); our study corroborates that the WEPP outperforms the USLE at shorter time-scales (i.e., 1-year annual and sub-annual) at the farm-field scale.

4.4.2. Erosion modelling and best management practices (BMPs)

There often exists a disconnect between the spatial scale at which best management practices (BMPs) are operationalized and the spatial scale at which they are prescribed by environmental modellers. To illustrate this disconnect we conducted a literature review using Google Scholar with the keywords “erosion model”, “agriculture”, and “BMP”. Thirty-one of the first one hundred reviewed papers were relevant and contained a BMP case study, whereby 14 (45.2%) used the SWAT model for BMP assessments, 4 (12.9%) used USLE, RUSLE, or RUSLE2, 3 (9.7%) used AGNPS, 2 (6.5%) used WEPP, and the remaining papers all employed a unique model. Twenty-three (74.2%) case studies used a combination of sediment yield, discharge, and nutrient measurements at catchment outlets for model evaluation, while the remaining 8 studies (25.8%) contained no model evaluation. Twenty-one (67.7%) studies used a hydrologic response unit (HRU; i.e., a catchment with homogeneous land use, soil, and topography) discretization for BMP implementation, 5 (16.1%) used a raster-based discretization, 2 (6.5%) were unspecified, and the remaining 3 studies (9.7%) used farm fields or hillslopes for discretization (WEPP hillslopes, Abaci and Papanicolaou 2009; AGNPS farm fields as individual cells, Yuan et al., 2008; SWAT farm field as HRU, Santhi et al., 2006). While BMPs are implemented at the farm field-scale to mitigate soil loss, the most common environmental modelling approach was to prescribe them at the scale of the HRU and evaluate modelling results with point-based measurements of sediment and discharge at watershed outlets (e.g., Bicknell et al., 1985; Moore et al., 1992; Bracmort et al., 2006; Rao et al., 2009; Betrie et al., 2011; Rousseau et al., 2013; Smith et al., 2014; Briak et al., 2019; Ricci et al., 2020). While this approach is pragmatic for BMP studies comprising large spatial extents, there is no evaluation or understanding of the hydrologic and sedimentologic processes at the most important spatial scale, the individual farm field.

To facilitate model up-scaling from individual farm fields to watersheds, we advocate that environmental modellers discretize watersheds as a collection of individual farm fields and coalesce outlet and field-based evaluations for a more holistic evaluation. This two-fold evaluation will allow the modeller to have a more in-depth understanding of the dominant sediment transport processes from fields to waterways where BMPs are implemented (i.e., field-scale evaluation) and from waterways to catchment outlets (i.e., outlet-based evaluation). This ensures the model is valid for a certain set of physiographic and climactic conditions, addresses issues of model equifinality and provides insights into model uncertainty. Only using an outlet-based evaluation may lead to a poor model implementation (e.g., equifinal model) and the implementation of

ineffective BMPs that can cause economic loss and degrade farmer confidence in governance and scientific modelling.

4.4.3. Field-scale best management practice evaluation

The UAV-based approach in this study was used to evaluate the applicability of the USLE and WEPP for a single agricultural field in southwestern, Ontario. The evaluation demonstrated that the WEPP was able to model the temporal variation in erosion rates whereas the USLE had some challenges representing temporally-distributed soil erosion rates (Table 4.6). Based on this evaluation, the WEPP should be an effective tool for evaluating field-scale BMPs. Our WEPP modelling results and field-scale measurements demonstrate that the most effective BMP would be one that incorporates additional biomass into the soil during the early growing season. This can be achieved by switching from a conventional fall plowing implement (i.e., moldboard plow; Fig. 4.1) to a conservation plowing implement (i.e., chisel plow). Chisel plows have long plow shanks, typically spaced 30 cm apart, with sweeps, shovels, or chisel points that break up and stir the soil but do not invert the topsoil like a traditional moldboard plow. This leaves a rough soil surface with sufficient biomass to cover the soil during the winter, early spring, and after the secondary tillage in the spring for final fitting when the site is most susceptible to erosion.

To evaluate the effects of switching tillage practices as a BMP to reduce long-term soil loss on our study site, we used the WEPP model to estimate 10-year average (2005–2014) soil erosion rates for: (1) a moldboard plow, (2) a chisel plow with coulters and shovels, and (3) a chisel plow with coulters and sweeps. The fall moldboard plow buries 95% of crop residue whereas the chisel plow will only bury 30–55% of crop residue (55% with coulters and shovels, 30% with coulters and sweeps). Studies demonstrate comparable yields between moldboard and chisel plowing for corn, soybean, and wheat, albeit with small variations in yield depending on nutrient amendments (Singer et al., 2004) and herbicide applications (Buhler, 1992), making it a pragmatic BMP choice for ameliorating accelerated rates of soil erosion.

The WEPP estimated the 10-year average erosion rate of the full 15.9-ha study site at 8.12 t ha^{-1} yr^{-1} when using a fall moldboard plow. Replacing the moldboard plow with a chisel plow with coulters and shovels for the fall tillage reduced soil erosion by 43%, resulting in a 10-year average erosion rate of 4.65 t ha^{-1} yr^{-1} (Table 4.7; Fig. 4.4). Replacing the moldboard plow with a chisel plow with coulters and sweeps for the fall tillage reduced soil erosion by 64%, resulting in a 10-year average erosion rate of 2.91 t ha^{-1} yr^{-1} (Table 4.7; Fig. 4.4). For all plowing implements, the WEPP estimated that the majority of long-term soil erosion occurred during the early growing season, with an average of 6.4 days per year with soil erosion. Winter events and

snowmelt constituted 70% of the average long-term runoff with 14.1 days per year with runoff, but winter runoff events were rarely associated with soil loss (Figs. 4.4 and 4.5). These results were consistent with our in-situ observations and measurements during the 2018–2019 study year.

Table 4.7. WEPP tillage scenarios of soil loss on the full 15.9-ha study site for three different tillage implements for a 10-year period (2005–2014). Results are split into the non-growing season (November to April) and the growing season (May to October).

Plowing implement	Non-growing season: total soil loss [t]	Growing season: total soil loss [t]	Erosion rate (t ha^{-1} yr^{-1})
Moldboard Plow	261.25	1028.43	8.12
Chisel Plow[1]	133.10	606.13	4.65
Chisel Plow[2]	58.80	402.81	2.91

1 chisel plow with coulters and shovels, **2** chisel plow with coulters and sweeps

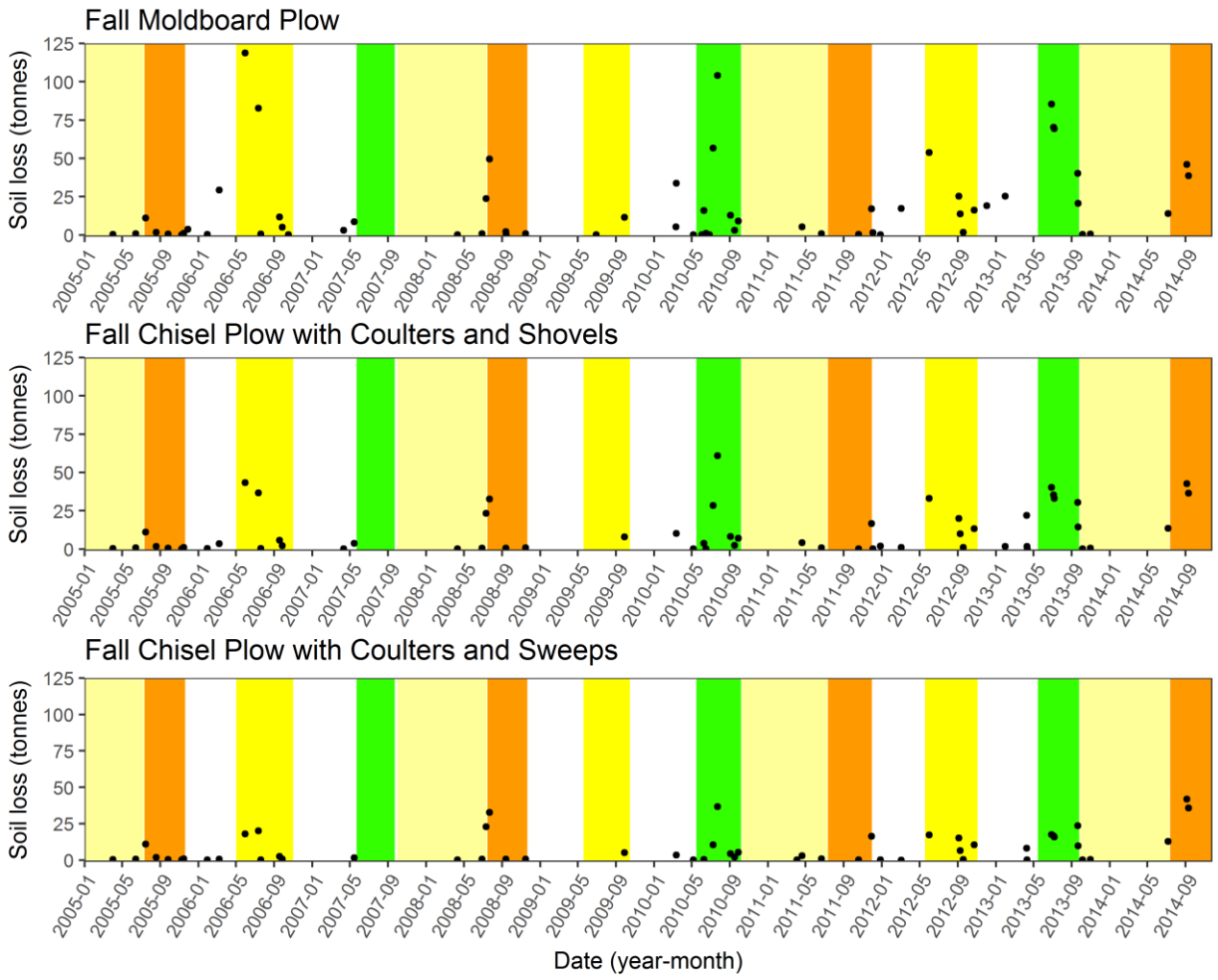

Fig. 4.4. WEPP soil loss predictions for the full 15.9-ha study site over a 10-year period. Soil loss is both to catch basins and off-site. Colored bars indicate growing season for crops: winter wheat (beige), oats (orange), corn (yellow), and soybean (green).

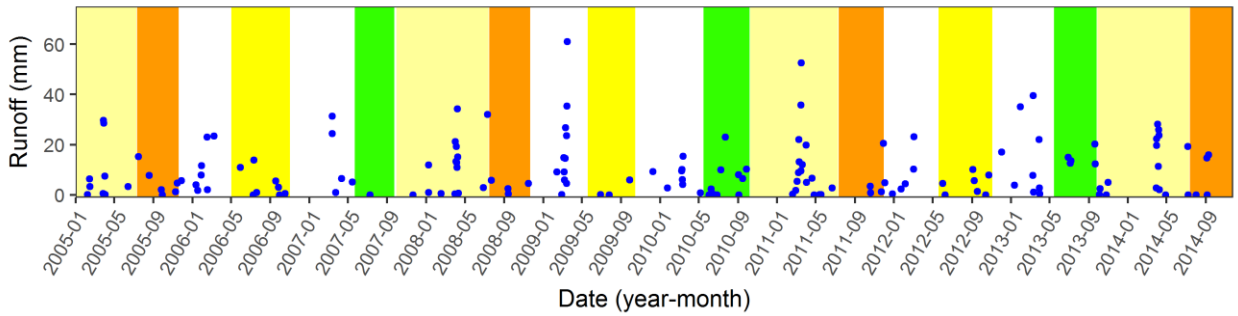

Fig. 4.5. WEPP runoff patterns for the full 15.9-ha study site for all three plowing implements. Colored bars indicate growing season for crops: winter wheat (beige), oats (orange), corn (yellow), and soybean (green).

Considering the regional context of our study site in that 68.1% of farms in the local county are using a conventional tillage system in their crop rotation (e.g., moldboard plow; Statistics Canada 2016), the transition to a conservation tillage system (e.g., chisel plow) could contribute to the amelioration of water quality issues in the region originating from sediment and particulate phosphorus losses. For our study site, the WEPP model estimated a 64% long-term reduction in soil loss when switching from a moldboard plow to a chisel plow with coulters and sweeps. While no-till management techniques would likely further reduce soil loss, no-till management practices can increase the risk of dissolved reactive phosphorus runoff (King et al., 2015) via macropore flow to subsurface tile drainage. Dissolved reactive phosphorus is readily bioavailable for biota uptake and is the limiting nutrient for primary production in adjacent aquatic systems (i.e., Lake Erie). Since the majority of the upper-Nith Watershed is tile drained (Loomer and Cooke 2011), permanent no-till systems are not recommended. A conservation tillage with a chisel plow removes the macropore connectivity of soils with subsurface drainage lines while still ensuring there is biomass on the field surface to protect against the impacts of rainfall when the field is most susceptible to erosion.

4.5. Conclusions

In this study we used semi-distributed erosion measurements with a UAV and SfM-MVS to evaluate the applicability of the USLE and WEPP to conditions in southwestern Ontario, Canada. While both models had satisfactory results, the USLE had a tendency to overestimate soil loss for each season which may have been the result of an incorrect characterization of rainfall intensity with our methodology. In contrast to the USLE, our model evaluations highlighted that the process-based modelling structure of the WEPP modelled the hydrology of our study site correctly (e.g., erosion from snowmelt and runoff) and was able to accurately model soil loss at an annual and sub-annual time step. For both models, model error tended to increase at shorter

time scales and small spatial extents; annual aggregated field-scale estimates of soil erosion were more accurate for both models. We strongly advocate that UAV-based model evaluations be conducted more commonly to ensure erosion models are behavioral before evaluating new BMPs and before scaling out models to larger spatial extents. UAV-based approaches collect the necessary qualitative and quantitative erosion measurements for model testing at the scale of the agricultural decision maker and can be used to inform models a priori. Future research should be aimed at improving the accuracy of the SfM-MVS workflow for change-detection such that fully distributed model evaluations can be conducted.

Chapter 5. Why connectivity matters in agricultural soil erosion modelling: A simulation of surface runoff on very-high resolution DEMs

5.1. Introduction

Soil loss is the movement of soil from a location that provides an ecosystem service to humans to one that does not, while soil erosion simply refers to the on-site movement of soil. While both have negative economic and environmental impacts, soil erosion only impacts on-site conditions, affecting crop yields by relocating soils from upslope to downslope areas (e.g., tillage erosion; Lobb et al. 1995, Van oost et al. 2006), while soil loss has both on-site and off-site impacts, reducing crop yields on-site (e.g., lost topsoil; den Biggelaar et al. 2001) and impacting waterbodies off-site (e.g., eutrophication, Michalak et al. 2013). On-site impacts of soil erosion and soil loss are the primary focus of landowners, since on-site impacts can directly affect farm profitability, and the off-site costs of soil loss are externalized. The focus of landowners on on-site impacts can be problematic since the costs associated with off-site soil loss are much greater than the costs of on-site soil erosion (e.g., 80% of costs occurred off-site in England and Wales; Graves et al. 2015, Boardman et al. 2019) and the differentiation between soil erosion and soil loss is not considered in most contemporary studies (e.g., studies based on the Universal Soil Loss Equation [USLE]; Panagos et al. 2015, FAO 2015).

The differentiation between soil erosion and soil loss is, in part, a function of landscape connectivity. Landscape connectivity in soil erosion studies refers to the degree by which soil can move between adjacent systems, e.g., agricultural fields to waterways. Low rates of water erosion in a well-connected system can have larger off-site impacts than high rates of water erosion in a disconnected system (Boardman et al. 2019). An accurate representation of landscape connectivity is necessary for accurate predictions of soil loss by water erosion; models that only represent one system (e.g., hillslopes; USLE, Wischmeier and Smith 1978) cannot differentiate between soil erosion and soil loss.

Soils can only move between systems when they are eroded, entrained, and transported in surface runoff, which makes landscape connectivity a function of surface runoff. Modelling surface runoff in an agricultural system requires an accurate representation of precipitation (intensity, duration), soil properties, surface cover, and microtopography. While precipitation does not need to have a spatially distributed component for field-scale hydrologic modelling, a spatial representation of soil properties, surface cover, and microtopography would improve spatially distributed predictions of surface runoff. However, environmental models are constrained by data inputs. The spatial variability of soil parameters (e.g., antecedent moisture conditions, hydraulic

conductivity) and surface cover make it prohibitive to accurately collect these data across large spatial extents at a fine resolution using conventional methods; they are more pragmatically represented aspatially at the farm-field scale. In contrast, an improved spatial representation of microtopography can now be achieved rapidly at a low-cost using UAVs (also known as remotely piloted aircraft systems; RPAS) and structure-from-motion (SfM) photogrammetry (Chapter 3; Meinen and Robinson 2020c).

The spatial and temporal variability of microtopography in agricultural systems from tillage and field operations are important drivers of infiltration, formation of flow pathways, and flow depth, which all affect surface runoff, yet they have received very little attention in hydrology (Dunne et al. 1991; Thompson et al. 2010). The exclusion of the spatially distributed effects of microtopography on hydrological processes is due to the computational constraints of representing small-scale distributed processes in numerical hydrologic models and the difficulty in measuring microtopography at a sufficient spatial resolution. The few studies on the effects of microtopography on hydrology and surface runoff are constrained to the plot-scale using simulated surfaces (virtual plots; e.g., Thompson et al. 2010; Appels et al. 2011; Frei and Fleckenstein 2014). While using plot-scale studies on simulated surfaces is pragmatic, it can be difficult to scale hydrologic responses from a simulated agricultural plot to an actual agricultural plot, hillslope, or field.

In this study, we use a series of very-high resolution (10-cm) agricultural digital elevation models (DEMs) created with a UAV SfM-MVS workflow to examine the impacts of microtopography on surface runoff to answer the following two research questions: (1) do factors that describe the microtopography of the landscape (i.e., random roughness [RR], slope, and maximum depression storage [MDS]) and land management practices (i.e., tillage orientation, and tillage implements) have a statistically significant impact on surface runoff, and (2) is the hydrologic response of a plot representative of the hillslope within which it resides? To answer these two questions, we developed a simple hydrological model to dynamically simulate rainfall, infiltration, and surface runoff on very-high resolution agricultural DEMs. We compared modelled runoff values to a linear model of surface runoff that used a set of topographic and environmental predictors to check for statistical significance.

5.2. Materials and Methods

5.2.1. Study site

The agricultural field used for this study is a 15.9-ha farm field located in southwestern Ontario, Canada (Fig. 5.1). The field has a 3-year rotation of corn, soybean, and winter wheat, which is a

common rotation for the region. Our study focusses on the period where the soil surface was exposed after a fall moldboard plow following a corn harvest, and after a spring cultivator was used for seedbed preparation for soybeans. The moldboard plow inverted the topsoil, burying the majority of corn stalk residue creating a rough soil surface (15 cm plow depth, 1 pass), while the field cultivator created a smoothed soil surface for planting (7.5 cm plow depth, 2 passes).

To model the topography of the farm field, we collected nadir optical imagery of the study site using FLIR System's R60 SkyRanger UAV. We captured imagery with the SR-3SHD payload (15 MP RGB, 4608 × 3288 resolution, 46-degree field-of-view) after the moldboard plow (33 ground control points, 0.011 m ground-sampling-distance) and using the HDZoom30 payload (20 MP RGB, 5184 × 3888 resolution, 68.6-degree field-of-view) after the field cultivator (69 ground control points, 0.014 m ground-sampling-distance). Ground control surveys were conducted using SmartNet's network real-time kinematic global navigation satellite system (RTK-GNSS) using a Leica Viva GS14 and Leica Viva CS15 field controller. The ground control survey and optical imagery were processed using Structure-from-Motion and Multi-view Stereo (SfM-MVS) algorithms in Pix4D (Pix4D SA, Switzerland) to generate 10-cm DEMs. See Meinen and Robinson (Chapter 3; 2020c) for more details on the processing workflow and UAV image acquisition details.

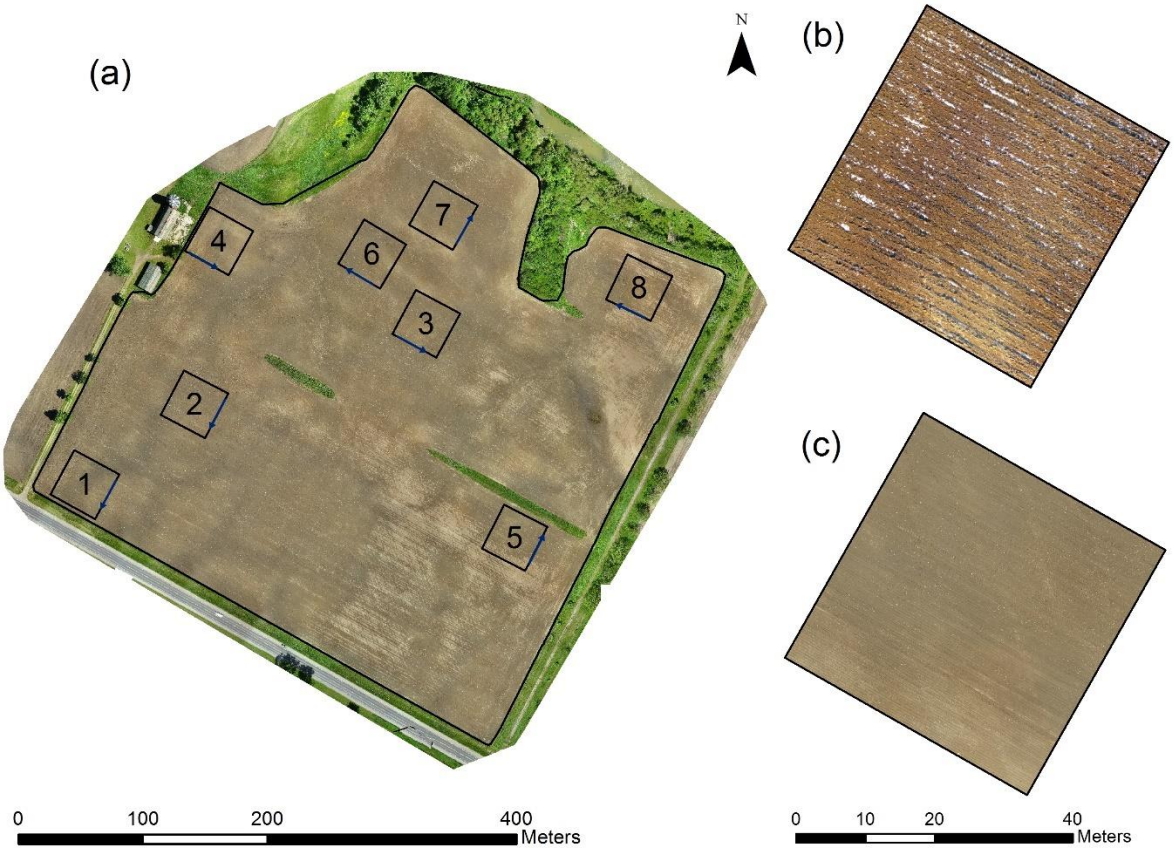

Fig. 5.1. UAV orthomosaic of (a) the full cultivated study site with labelled plots 1 – 8 used for hydrology simulations, (b) a moldboard plowed plot (Plot M7), and (c) a cultivated plot (Plot C7). See Table 5.1 for a detailed description of each plot.

5.2.2. Hydrology model

We developed a simple hydrology model to represent saturation excess overland flow using very-high resolution DEMs. The model is a continuous simulation (0.25-min timestep) that iterates through four phases for calculating the hydrologic response of a farm field (Fig. 5.2):

1. **Rainfall:** steady-state storms are simulated that distribute rainfall uniformly over a DEM surface for each model timestep.

2. **Infiltration:** water is infiltrated into the soil for each timestep using the Mein-Larson (1973) modification of Green-Ampt (1911; Section 5.2.3).

3. **Flow routing:** water is routed from cells of higher elevation to cells of lower elevation using a D4 routing algorithm on a cell-by-cell basis. Ponded water is added to the elevation of each cell to account for depressions filling and spilling. The velocity of

overland flow is assumed constant within a single hillslope and is calculated based on the average gradient of the modelled hillslope (McCuen et al. 2002):

$$v = 10kS^{0.5}$$

where v is the velocity of shallow concentrated flow (m s^{-1}), k is a dimensionless unit which is a function of land cover, and S is slope (m m^{-1}).

4. **Surface Runoff:** cumulative runoff is calculated as the total volume of water that flows off of a DEM surface during the simulation. Water that reaches an edge cell of a DEM is preferentially routed off of the surface.

Model input requirements for our hydrology simulation are rainfall rate (mm h^{-1}; steady rainfall), a very-high resolution DEM (.ascii format), and the following soil properties: effective porosity, wetting front soil suction head (cm), hydraulic conductivity (cm h^{-1}), and the initial saturation (i.e., antecedent moisture conditions).

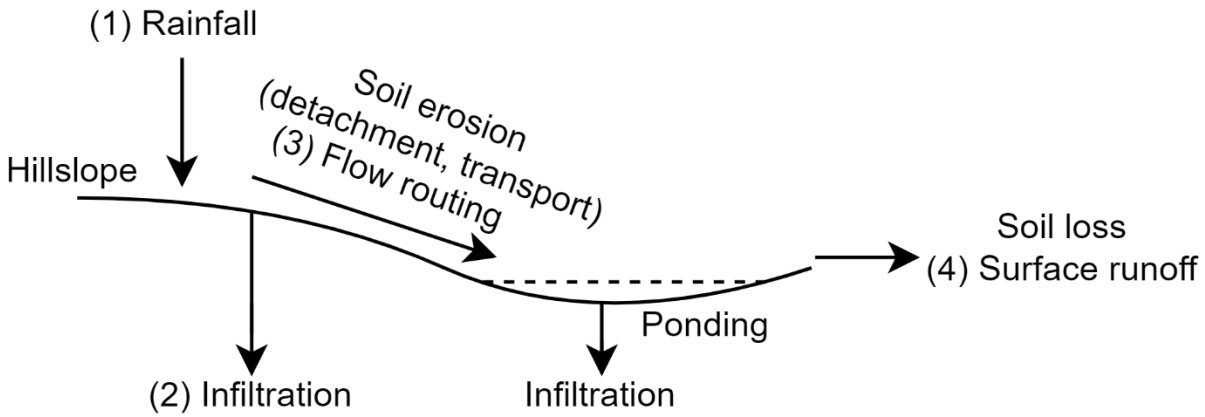

Fig. 5.2. Conceptual diagram of hydrology model.

5.2.3. Infiltration

For each model timestep, we use the Mein and Larson (1973) modification of the Green-Ampt (1911) model to simulate infiltration into the soil column. The Green-Ampt model assumes a sharp break in the soil column at the wetting front and assumes continuous ponding at the soil surface. The Mein and Larson (1973) modification is used to estimate the cumulative infiltration before the rainfall rate exceeds the infiltration rate of the soil, i.e., cumulative infiltration before ponding occurs. While the simulation time, t, is less than the time to ponding, t_p, the infiltration rate is equal to the rainfall intensity and the cumulative infiltration is calculated as:

$$F(t) = it \qquad for\ t < t_p$$

where *F(t)* is the cumulative infiltration at time *t*, *i* is the rainfall intensity (cm h^{-1}), and t_p is time to ponding (h). The time to ponding is calculated as:

$$t_p = \frac{K\psi\Delta\theta}{i(i-K)}$$

where K is the hydraulic conductivity of the soil (cm hr^{-1}), ψ is the wetting front soil suction head (cm), and $\Delta\theta$ is the increase in soil moisture during infiltration. Once ponding has occurred on the soil surface, $F_p = it_p$, where F_p is cumulative infiltration at ponding time (cm). The increase in soil moisture during infiltration is a function of the initial saturation of the soil column and the effective porosity of the soil:

$$\Delta\theta = (1 - S_e)\theta_e$$

where S_e is the initial saturation of the soil column and θ_e is the effective porosity of the soil. Since the Green-Ampt model assumes continuous ponding at the water surface, the cumulative infiltration after ponding occurs on the soil surface can be calculated as:

$$F(t) = Kt + \psi\Delta\theta\ln\left(1 + \frac{\mathrm{F(t)}}{\psi\Delta\theta}\right) \qquad for\ t > t_p$$

Once this implicit equation is solved, the infiltration rate is:

$$f(t) = K\left[\frac{\psi\Delta\theta}{\mathrm{F(t)}} + 1\right] \qquad for\ t > t_p$$

where *f(t)* is the infiltration rate at time *t*.

5.2.4. Hydrology simulations

Although we modelled the topography of our full 15.9-ha agricultural study site (Chapter 3; Meinen and Robinson 2020c), we subdivided the farm field into 16 plots for our hydrology simulations (40 x 40 m; Table 5.1) to better isolate the relative impacts of microtopography on surface runoff. Plots were chosen to represent a range of slope gradients (1% to 14%), tillage orientations (down-slope, cross-slope, undefined), and two different tillage implements (moldboard, cultivator). Plots 2-3, 5-6, and 7-8 are plot-pairs (cross-slope, down-slope) and were used for comparing tillage orientations. Hydrology simulations were conducted on all 16 plots using three one-hour rainfall events (10 mm h^{-1}, 15 mm h^{-1}, 20 mm h^{-1}) and three antecedent soil moisture conditions (25% [AMC 1], 50% [AMC 2], 75% [AMC 3]), which resulted in a total of 144 simulations. The rainfall events and AMC conditions loosely corresponded to a range of environmental conditions that occurred on our study site from 2018 to 2019 that had the potential to produce surface runoff

(Chapter 3; Meinen and Robinson 2020c). The surface runoff value for each plot was recorded after the rainfall portion of the hydrology simulation had ended and water had sufficient time to route off the surface; each model outcome was deterministic.

For all hydrology simulations, we use the dominant textural class on our agricultural study site (loam) whereby we assume an effective porosity of 0.434, hydraulic conductivity of 0.34 cm h^{-1}, and a wetting front soil suction head of 8.89 cm. To correspond to bare-earth conditions, we use a k value of 0.274 to represent the effects of surface cover on flow velocity. The topography for each hydrology simulation was modelled with a 10 cm DEM.

Table 5.1. Topographic metrics for 40 x 40 m (0.16 ha) plots used in hydrology simulations: cultivator (C), moldboard (M).

Surface model	Random Roughness (RR) (mm)	Slope (%)	Tillage orientation	Maximum Depression Storage (MDS) (mm)
Cultivator (C)				
Plot C1	20.77	1.49	Undefined*	18.46
Plot C2	20.91	3.31	Cross	13.59
Plot C3	21.79	4.89	Down	10.45
Plot C4	21.23	8.02	Combination	1.07
Plot C5	20.20	9.77	Cross	1.48
Plot C6	20.91	9.51	Down	0.73
Plot C7	26.15	14.01	Cross	1.27
Plot C8	23.95	14.05	Down	0.61
Moldboard (M)				
Plot M1	38.12	1.78	Undefined*	19.07
Plot M2	35.10	3.45	Cross	16.14
Plot M3	41.47	5.26	Down	11.56
Plot M4	41.04	8.39	Combination	2.12
Plot M5	33.92	9.77	Cross	3.86
Plot M6	29.63	9.57	Down	0.66
Plot M7	27.70	14.07	Cross	0.82
Plot M8	33.58	14.05	Down	0.55

*the topography is predominantly level

5.2.5. Linear regression on drivers of surface runoff

To determine the relative impact of microtopography, land management, and environmental factors on surface runoff, modelled surface runoff values for each plot were regressed against 7 predictor variables (Table 5.2), whereby predictors were considered significant for $p < 0.05$. Topographic predictors were calculated in ArcGIS v10.6.1 for each plot (Table 5.2). RR is calculated as the standard deviation in elevation of the soil surface after a correction for slope has been made (methodology of Kamphorst et al. 2000). Surface slope is calculated using a 1 m raster representation of each plot. MDS, i.e., how much water can be stored on a soil surface, is calculated as the total water pooled on the DEM surface after a 50 mm h^{-1} rainfall event with no infiltration; this rainfall intensity was sufficient to fill and spill all depressions on each DEM surface. The calculation of MDS was made using our hydrology simulation for each plot after all excess water had routed off the surface, leaving only the pooled water in depressions.

Table 5.2. Predictors of surface runoff used for a multivariate linear regression.

Regression Metrics	Equation	Reference
Precipitation		10 mm h^{-1}, 15 mm h^{-1}, 20 mm h^{-1}
AMC		25%, 50%, 75%
RR*	$RR = \left[\frac{1}{k}\sum_{i=1}^{k}(Z_i - \bar{Z})^2\right]^{1/2}$	Z_i = height measurement (cm) on cell *i* K = number of measurements
Slope	$S = ATAN\left(\sqrt{\left(\left[\frac{dz}{dx}\right]^2 + \left[\frac{dz}{dy}\right]^2\right)}\right)$	Percent slope
MDS	$MDS = \bar{p}$	p = water pooled on each cell (cm) after a 50 mm h^{-1} storm (no infiltration)
Tillage orientation		Cross-slope, undefined, down-slope
Tillage implements		Moldboard, cultivator

*$Z_i - \bar{Z}$ is calculated by subtracting a smoothed DEM (focal statistics, mean, rectangle, 30 x 30 m) from the original DEM, i.e., correcting for surface slope before calculating the standard deviation of the surface height.

5.2.6. Up-scaling plots to hillslopes

Research on agricultural erosion and hydrologic processes is most commonly conducted at the plot scale, so an important question to address for field-scale research is if the hydrologic response of a plot is representative of the hillslope within which it resides. To determine if plots were representative of hillslopes, we ran an additional set of hydrology simulations on 6 hillslopes (Table 5.3) using three one-hour rainfall events (10 mm h^{-1}, 15 mm h^{-1}, 20 mm h^{-1}) and one

antecedent soil moisture condition (50% [AMC 2]), 18 simulations in total. We constrained our hillslope-scale hydrology simulations to 18 due to computational constraints and since only a subset of our plots resided within hillslopes that had a clearly defined start and end point with minimal topographic variation. The hydrologic response of each plot was compared to the hydrologic response of the hillslope within which it resided to look for variance in surface runoff values.

Table 5.3. Topographic metrics for each hillslope used in the hydrology simulations.

Surface Model	RR (mm)	Slope (%)	Tillage	MDS (mm)	Surface Area (ha)
Cultivator					
Hillslope C1	21.33	2.08	Undefined*	20.30	3.88
Hillslope C7	23.46	10.60	Cross	1.61	1.31
Hillslope C8	24.32	10.01	Down	0.75	0.74
Moldboard					
Hillslope M1	35.92	2.34	Undefined*	20.71	3.88
Hillslope M7	43.76	10.74	Cross	5.06	1.31
Hillslope M8	38.60	10.15	Down	1.50	0.74

*the topography is predominantly flat

5.3. Results

5.3.1. Surface runoff: Plots

To determine the relative impact of microtopography, land management, and environmental factors on surface runoff, we compared the variability in surface runoff for each hydrology simulation across our 16 plots (Table 5.4). There was a wide variance in the hydrologic response of each plot, and we note three well-defined empirical trends for tillage orientation, MDS, and slope.

Cross-slope tillage patterns decreased surface runoff relative to down-slope tillage patterns for every hydrology simulation, but the effect was less pronounced on plot pairs with steeper slope gradients and for larger storms. On average, cross-slope tillage patterns reduced surface runoff by 67.0% for 10 mm h^{-1} storm events, 45.1% for 15 mm h^{-1} storm events, and 29.7% for 20 mm h^{-1} storm events. The largest difference in surface runoff was exhibited by the relatively flat plot-pair M2-M3 where the cross-slope tillage pattern of M2 reduced surface runoff by an average of 68.4% for all hydrology simulations relative to the down-slope tillage pattern of M3.

This is contrasted by the steep plot-pair M7-M8 where the cross-slope tillage pattern of M7 reduced surface runoff by only 20.3% relative to the down-slope tillage pattern of M8.

Higher values of MDS led to a smaller volume of surface runoff, but the depressions in each plot did not need to be fully filled before surface runoff occurred. Comparing the set of plots with the highest values of MDS (Plots 1 – 3; MDS: 10.45 – 19.07) to the set of plots with the lowest values of MDS (Plots 4 – 8; MDS: 0.55 – 3.86), there was an average decrease in surface runoff for the set of plots with the highest value of MDS of 85.5% for 10 mm h^{-1} storm events, 75.2% for 15 mm h^{-1} storm events, and 70.0% for 20 mm h^{-1} storm events.

Slope gradient exhibited the same plot trends as MDS since slope and MDS were inversely correlated, i.e., MDS increased as slope decreased. As the slope gradient increased for each plot, surface runoff also increased. The set of plots with the shallowest slope gradients (< 5%; Plots 1 – 3) had a smaller and more variable volume of surface runoff than the plots with steeper slope gradients (8 – 14%; Plots 4 - 8).

Table 5.4. Surface runoff (mm) for each plot-scale hydrology simulation using three different rainfall intensities and antecedent moisture conditions. Bold numbers indicate that all the depression storage of the plot was filled for the rainfall event.

	10mm			**15mm**			**20mm**		
Surface	AMC1	AMC2	AMC3	AMC1	AMC2	AMC3	AMC1	AMC2	AMC3
C1	0.00	0.01	0.03	0.06	0.12	0.26	0.31	0.45	0.69
C2	0.00	0.01	0.10	0.24	0.60	1.44	1.65	2.46	3.68
C3	0.00	0.01	0.23	0.63	1.41	2.71	3.08	4.15	5.71
C4	0.00	0.05	0.73	**1.37**	**2.49**	**4.42**	**5.13**	**6.76**	**9.17**
C5	0.00	0.01	0.28	**0.77**	**1.83**	**3.69**	**4.50**	**6.15**	**8.57**
C6	0.00	0.06	**0.88**	**1.61**	**2.80**	**4.74**	**5.53**	**7.16**	**9.56**
C7	0.00	0.01	0.55	**1.28**	**2.49**	**4.47**	**5.12**	**6.75**	**9.15**
C8	0.00	0.11	**0.97**	**1.71**	**2.90**	**4.83**	**5.65**	**7.29**	**9.69**
M1	0.00	0.01	0.03	0.05	0.10	0.19	0.23	0.32	0.50
M2	0.00	0.01	0.04	0.06	0.12	0.39	0.51	0.92	1.66
M3	0.00	0.01	0.14	0.38	1.01	2.20	2.55	3.55	5.02
M4	0.00	0.05	0.59	1.18	2.22	4.08	4.76	**6.37**	**8.76**
M5	0.00	0.01	0.06	0.21	0.87	**2.46**	**3.09**	**4.58**	**6.87**
M6	0.00	0.04	**0.92**	**1.66**	**2.85**	**4.80**	**5.59**	**7.22**	**9.63**
M7	0.00	0.02	**0.71**	**1.48**	**2.72**	**4.71**	**5.38**	**7.02**	**9.42**
M8	0.00	0.13	**1.06**	**1.79**	**2.98**	**4.92**	**5.74**	**7.37**	**9.77**

5.3.2. Regression analysis: Plots

To evaluate if the drivers of surface runoff in Section 5.3.1. had a significant influence on simulated runoff rates, we regressed surface runoff against our 7 predictor variables using a multivariate linear regression (Table 5.2). The regression had an adjusted R-squared of 0.788, with four statistically significant predictors: precipitation, AMC, MDS, and tillage orientation (Table 5.5). Since there was a high degree of collinearity between predictors (VIF: 4.5 – 6), we optimized our regression by only including the statistically significant predictors. Our optimized regression had an adjusted R-squared of 0.791 with no collinearity between predictors, but tillage orientation was just outside the threshold for being statistically significant ($p = 0.06$).

Table 5.5. Multivariate linear regression for predicting surface runoff. Adjusted R-squared: 0.788.

Predictors	p-value	Variance Inflation Factor	Trend
(Intercept)	**5.41e-10**		
Precipitation	**< 2e-16**	1.000	Increase in precipitation, increase in runoff
AMC	**3.25e-11**	1.000	Increase in AMC, increase in runoff
MDS	**1.16e-04**	5.915	Increase in MDS, decrease in runoff
RR	0.790	4.824	No statistically significant trend
Slope	0.489	5.694	No statistically significant trend
Tillage orientation	**0.050**	1.086	Cross-slope tillage, decrease in runoff Down-slope tillage, increase in runoff
Tillage implements	0.997	4.673	No statistically significant trend

Despite MDS being the strongest topographic predictor of surface runoff, MDS is a poorly defined predictor, because there is no standardized method for calculating MDS, and an accurate calculation of MDS is constrained by the spatial resolution of the DEM used in the calculation, since grid cell size has a significant impact on surface depression storage (Abedini et al. 2006; Martin et al. 2008). Due to ambiguity with calculations of MDS, it is more pragmatic to relate surface runoff as a function of simpler topographic predictors. To assess the individual contribution of each topographic predictor, modelled surface runoff values for each plot were regressed against precipitation, AMC, and one topographic variable (Table 5.6).

In lieu of MDS, slope was found to be the best predictor of surface runoff with an adjusted R-squared of 0.753; MDS was collinear with slope (VIF ~ 5), making slope a strong substitute for MDS. While both slope and MDS are affected by the spatial resolution of the input DEM, only the accuracy of MDS is constrained by the spatial resolution of the DEM. Tillage orientation was also a good topographic predictor of surface runoff and could be used in conjunction with slope for a more accurate estimation of surface runoff. While RR and tillage implements were not statistically significant, it is important to note that all the listed topographic variables will have an impact on the economic and environmental significance of surface runoff, e.g., impacting soil erosion and soil loss. For example, different tillage implements will affect the aggregate stability and amount of crop residue on the soil surface which has a significant impact on soil movement (Busari et al. 2015), even if the effects on surface runoff were poorly defined at the plot scale.

Table 5.6. Alternative multivariate linear regression for predicting surface runoff using precipitation, AMC, and one topographic variable. The regression must yield an adjusted R-squared > 0.588 to be a better fit than a model with no topographic predictor.

Adjusted	**p-value**						
R-squared	Precipitation	AMC	MDS	RR	Slope	Tillage orientation	Tillage Implements
0.787	**< 2e-16**	**3.03e-11**	**< 2e-16**	x	x	x	x
0.592	< 2e-16	6.27e-07	x	0.111	x	x	x
0.753	**< 2e-16**	**4.45e-10**	x	x	**< 2e-16**	x	x
0.602	**< 2e-16**	**4.69e-07**	x	x	x	**0.015**	x
0.587	< 2e-16	7.37e-07	x	x	x	x	0.431

5.3.3. Surface runoff: Plots to hillslopes

To identify if the hydrologic response of a plot was representative of the hillslope within which it resides, we compared the results of our plot-scale hydrology simulations with 18 hillslope-scale hydrology simulations. The hillslope-scale hydrology simulations showcased the same general surface flow relationships that occurred at the plot scale, i.e., (1) cross-slope tillage patterns resulted in a lower volume of surface runoff relative to down-slope tillage patterns, (2) surface runoff increased as MDS decreased, and (3) surface runoff increased as slope gradient increased (Table 5.7).

While the same general empirical trends held true at both the plot and hillslope scale, there was less surface runoff at the hillslope scale relative to the plot scale, most notably for the more topographically complex moldboard-plowed surfaces. The greater difference between plot and hillslope scales for the moldboard-plowed surfaces is expected since the results from a planar one-dimensional plot are easily scaled in space, whereas a topographically complex surface is more difficult to generalize. As the complexity of the surface increases, it becomes increasingly more difficult to capture the topographic variability of a hilllslope using a plot.

Table 5.7. Surface runoff for each hillslope compared to the equivelant plot-pair for AMC2 rainfall events.

	10mm	15mm	20mm		10mm	15mm	20mm
Surface Model	AMC2	AMC2	AMC2	**Surface Model**	AMC2	AMC2	AMC2
Cultivator				**Cultivator**			
C1 Plot	0.01	0.12	0.45	C1 Hillslope	0.00	0.05	0.20
C7 Plot	0.01	2.49	6.75	C7 Hillslope	0.01	2.34	6.45
C8 Plot	0.11	2.90	7.29	C8 hillslope	0.01	2.38	6.49
Moldboard				**Moldboard**			
M1 Plot	0.01	0.10	0.32	M1 Hillslope	0.00	0.04	0.13
M7 Plot	0.02	2.72	7.02	M7 Hillslope	0.00	0.85	4.00
M8 Plot	0.13	2.98	7.37	M8 Hillslope	0.01	1.96	5.94

The topographic variability of a moldboard-plowed surface relative to a cultivated surface is best exemplified by a visual comparison of surface runoff patterns on Hillslope M7 (Fig. 5.3a) and Hillslope C7 (Fig. 5.3d). There was a lower amount of surface runoff on Hillslope M7 due to surface ponding in random localized depressions. In the north-western section of Hillslope M7 (Fig 5.3c), water ponded to a depth of 5 – 10 cm created by the deeper 15 cm moldboard plow; these localized depressions were hydrologically disconnected on Hillslope M7, whereas Hillslope C7 had a smoother soil surface that actively contributed to surface runoff (Fig. 5.3f). Due to the spatial variability of these localized depression on Hillslope M7, Plot M7 did not capture the full effect of these depressions on surface runoff, and as such, the plot-scale simulation had significantly more runoff than the hillslope-scale simulation. Similarly, since the gradient of each hillslope decreased towards the field edge, significant amounts of surface runoff pooled in cross-slope tillage lines, tire tracks, and flat topography at the field edge of both surfaces, but more prominently for the moldboard plowed surface (e.g., Fig. 5.3b, e); these edge effects were not captured at the plot scale for either the cultivated or moldboard surfaces.

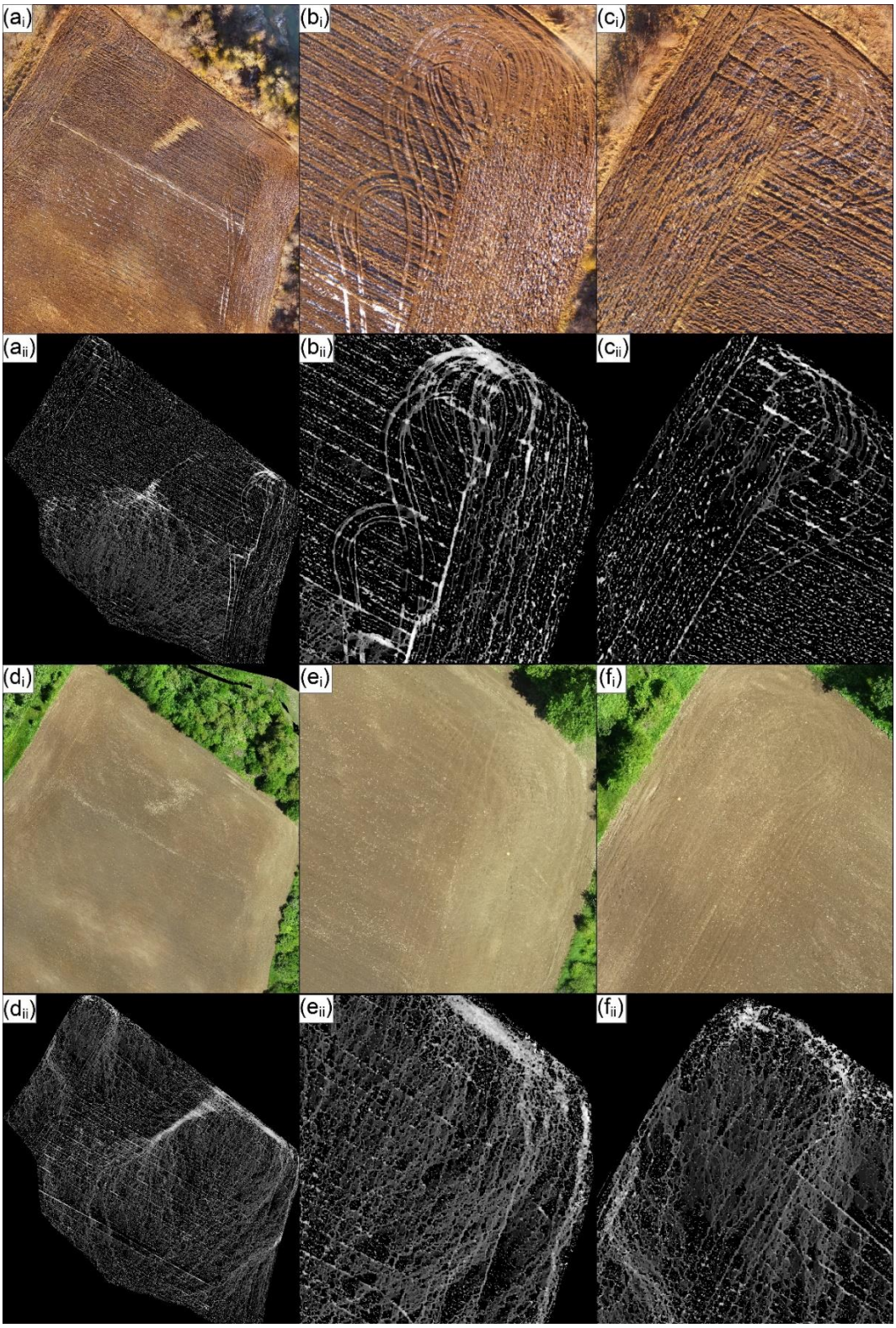

Fig. 5.3. Difference in modelled flow pathways between a moldboard plow (a, b, c; Hillslope M7) and a field cultivator (d, e, f; Hillslope C7) during a one-hour 20 mm hr^{-1} storm event with 50% antecendent soil moisture content: (i) UAV orthomosaic, (ii) simulated flow pathways. For the simulated flow pathways, black indicates no water accumulation.

5.4. Discussion

Our hydrology simulations demonstrated a wide variation in hydrologic responses from different plots and hillslopes. MDS, slope, and tillage orientation all had a statistically significant impact on surface runoff at the plot scale. These three relationships are expected since cross-slope tillage patterns and shallow slope gradients are likely to increase surface ponding and an increase in surface ponding (or MDS) will decrease surface runoff (Mishra et al. 2014; Huang et al. 2006). While MDS was the best single topographic predictor of surface runoff, incorporating the effects of slope into a hydrology model is the most pragmatic approach for including the effects of microtopography on surface runoff, since slope is a simpler surface metric to calculate and collinear with MDS. A simple regression that predicts surface runoff for a given soil type as a function of precipitation, AMC, and one topographic predictor aligns well with simple models of surface runoff like the Soil Conservation Services (SCS) runoff curve number, which for a given soil type, predicts surface runoff from precipitation, AMC, and an initial abstraction coefficient. An inclusion of a topographic predictor is necessary for an accurate prediction of surface runoff, most notably for flat agricultural systems with high rates of surface ponding (e.g., Plot M1, C1).

While the type of tillage implement did not have a statistically significant impact on surface runoff at the plot scale, our hillslope-scale hydrology simulations showcased that the deeper moldboard plow was responsible for hydrologically disconnecting large areas of each hillslope. Conditions were more favorable for surface runoff on cultivated hillslopes. The plot-scale representation of the moldboard-plowed hillslopes did not adequately capture these isolated depressions, indicating that the hydrologic response of a plot can be a poor predictor of hillslope-scale hydrology. While the moldboard plow is generally linked with increased water erosion rates due to an exposed soil surface from inverting the soil column (e.g., Wischmeier and Smith 1978), the decreased landscape connectivity may ameliorate soil loss. The effects of the decreased connectivity can be seen in Meinen and Robinson (Chapter 3; 2020c) where soil movement from upslope areas to downslope catch basins was highest immediately following a spring cultivation and relatively low on a moldboard plowed surfaces over a winter season.

5.5. Conclusions

While the computational expense of running hydrology simulations on very-high resolution DEMs is still high, our ability to quickly measure microtopography with the UAV SfM-MVS workflow has made very-high resolution agricultural DEMs a valuable research tool for improving our understanding of field-scale hydrology. Our hydrology simulations demonstrated that the microtopography of an agricultural system can have a significant impact on rates of surface runoff.

Incorporating the spatial and temporal variation in microtopography from field and tillage operations is necessary for an accurate model of surface runoff and associated soil loss. Landscape connectivity between agricultural fields and waterways cannot be modelled without an accurate representation of microtopography.

Chapter 6. From hillslopes to watersheds: Variability in model outcomes with the USLE

6.1. Introduction

The roots of modern soil erosion modelling originated in the American Midwest during the early 1900's (e.g., 1917 Missouri Agricultural Experiment Station). The detrimental impacts of mechanized agriculture on soil erosion and agricultural productivity were brought to the attention of the American Congress by Hugh Hammond Bennett who secured funding in 1929 for establishing ten experimental erosion plots (Meyer and Moldenhauer 1985). The advocacy of Bennett to the American Congress, the 1930's Dust Bowl in the Great Plains of North America, and the subsequent widespread crop failure collectively influenced the American Congress to pass the Soil Conservation Act of 1935 (Public Law 74-46). The act states that, "…it is hereby recognized that the wastage of soil and moisture resources on farm, grazing, and forest lands of the Nation, resulting from soil erosion, is a menace to the national welfare and that it is hereby declared to be the policy of Congress to provide permanently for the control and prevention of soil erosion…" (Public Law 74-46). This act provided national funding for soil erosion research, resulting in the first conceptualizations of erosion models (e.g., Zingg 1940; Smith 1941; Musgrave 1947) and most prominently culminated with the development of the Universal Soil Loss Equation (USLE; Wischmeier and Smith 1965).

The USLE is a lumped empirically-based soil erosion model that was developed by the United States Department of Agriculture and Soil Conservation Services. First published in Agricultural Handbook no. 282 (Wischmeier and Smith 1965) and widely adopted based on the superseding publication in 1978 (no. 537; Wischmeier and Smith 1978), the USLE is the culmination of over 10,000 plot years of erosion measurements spanning several decades. The basis of the USLE is a unit plot, represented by a small, fallow agricultural plot (22.1 m long x 1.8 m wide) with a 9% slope gradient and an up-down slope tillage pattern; the soil loss of other experimental erosion plots (e.g., slopes 3 – 18%, slope lengths 9 – 91 m) were described relative to these reference conditions. The USLE encapsulates a representation of the erodibility of an agricultural hillslope relative to the conditions of the unit plot using six empirically-derived factors (Wischmeier and Smith 1978):

$$A = R\,K\,L\,S\,C\,P$$

where A is the annual soil loss per unit area (t ha^{-1} yr^{-1}), R is a rainfall and runoff factor (MJ mm ha^{-1} h^{-1} yr^{-1}), K is a soil erodibility factor (t ha h ha^{-1} MJ^{-1} mm^{-1}), L is a slope-length factor (unitless),

S is a slope-steepness factor (unitless), C is a cover and management factor (unitless), and P is a supporting practice factor (unitless; Wischmeier and Smith 1978). Soil loss in the USLE is conceptualized as soil loss from an agricultural hillslope resulting from rill and interrill erosion.

Since the seminal publication of 1978 (Wischmeier and Smith 1978), the USLE has been revised (RUSLE; Renard et al. 1991) and succeeded by RUSLE2 and the process-based Water Erosion Prediction Project (WEPP; Laflen et al. 1991). The successors of the USLE and new models developed in the late 20th century sought to overcome the inherent empirical limitations of the USLE and extend the applicability of soil erosion models by representing sediment conveyance and depositional processes (e.g., Laflen et al. 1991). These modelling developments can be classified into two classes of erosion models: (1) hybrid models that couple the USLE factors with a sediment transport model (e.g., Soil and Water Assessment Tool, Arnold et al. 1998; Areal Nonpoint Source Watershed Environment Response Simulation, Beasley et al. 1980), or (2) process-based models that are independent of the empiricisms of the USLE (e.g., LISEM; De Roo et al. 1996, WEPP).

Despite scientific efforts to derive new process-based models or improve upon the USLE, the USLE and revised USLE still remain the de-facto standards for management-oriented soil erosion studies (Alewell et al. 2019) both as a standalone tool and via incorporation into hybrid models. The USLE has been operationalized for ease of use with Geographic Information Systems (GIS) to up-scale the model from predicting soil loss for individual hillslopes to predicting soil erosion at national (e.g., Italy; Grimm et al. 2003, Switzerland; Prasuhn et al. 2013), continental (e.g., Europe; Panagos et al. 2015a), and global (e.g., Borrelli et al. 2017) scales. Among these large-scale applications, the USLE has been used as a decision support tool for soil erosion prevention (e.g., Prasuhn et al. 2013), a technical support tool for sustainable development (e.g., Van der Knijff et al. 1999; Grimm et al. 2003), and for quantifying the severity of soil degradation from soil erosion processes globally (e.g., FAO, 2015).

Models applied at large spatial extents typically forgo complicated process descriptions, which result in higher intrinsic model error but low model input error (Rompaey and Govers 2002). The simple structure and parsimonious parameterization of the USLE meets this criterion and has driven its widespread use from small (i.e., plot, field) to large (watershed, national, global) spatial extents. However, if model applications across large spatial extents are the result of extending a model beyond its designed application space, then additional uncertainty is introduced into modelling outcomes. Despite the USLE being designed for predicting soil loss from planar hillslopes, its implementation in combination with a GIS has taken vastly different methodological

approaches (e.g., Fistikoglu and Harmancioglu 2002; Amore et al. 2004; Erdogan et al. 2007; Pandey et al. 2007; Dabral et al. 2008; Hui et al. 2010; Devatha et al. 2015; Belasri and Lakhouili 2016; Rizeei et al. 2016; Singh and Panda 2017) for up-scaling the USLE to large spatial extents with little-to-no acknowledgement of the different types of error and uncertainty, or their quantification, in the up-scaling process.

The predictive accuracy of an erosion model can be conceptualized as comprising four components: (1) intrinsic model error, (2) model input error, (3) model user error, and (4) stochastic error. Intrinsic model error is the error inherent to the model as a result of a simplified modelling structure, which manifests itself when a model developer chooses to forgo a parameter that affects soil erodibility (e.g., hydraulic conductivity) in favor of a more parsimonious modelling structure (e.g., soil texture). Model input error is the error derived from poorly measured or estimated model inputs, which typically manifests itself when remote sensing products are used in lieu of detailed in-situ measurements. Model user error is a result of an incorrect application or parameterization of a model. Lastly, the stochasticity of coupled human-natural systems (e.g., variance in replicate plots; Wendt et al. 1986) can result in variation among erosion estimates that cannot practically be modelled (i.e., stochastic error). The total error of a model's prediction is the sum of these four error sources.

All USLE predictions of soil erosion rates will carry some amount and combination of intrinsic model error, model input error, model user error, and stochastic error. However, when up-scaling the USLE from the hillslope scale to larger spatial extents, model input and user error are of particular concern, since data constraints, design choices, and spatial conceptualizations of a system will invariably influence model outcomes. Error in erosion predictions can be evaluated for studies conducted at larger spatial extents by comparing modelled and measured soil erosion rates on a subset of farm fields within a watershed (e.g., Favis-Mortlock, 1998) or when there is comprehensive erosion data collected for the watershed (e.g., Jetten et al. 1999). Since comprehensive erosion data are typically not available and validating the outcomes of spatially-distributed erosion rates is complex, we focus our discussion on the variability in USLE model outcomes, rather than error or uncertainty. To exemplify the variability in USLE model outcomes, we conduct a case study for up-scaling the USLE in the upper-Nith Watershed, Ontario, Canada. We compare our recommended modelling approach with other common modelling approaches in literature to answer the following question: what is the variability in model outcomes from different model user's design choices for up-scaling the USLE to large spatial extents?

6.2. Materials and Methods

6.2.1. Study Site

Our case study is situated in the upper reaches of the Nith Watershed in Ontario, Canada. The upper-Nith Watershed is an agricultural watershed characterized by row cropping of corn, soybean, winter wheat, and alfalfa. In 2015, farm fields covered 39,708 ha (73%) of the watershed, with an average farm-field size of 8.46 ha, an average farm-field slope of 1.8 degrees, and a standard crop rotation of corn, soybean, and winter wheat. An extensive tile drainage system covers the upper-Nith Watershed (Appendix C Fig. C7), which drains 22,660 ha of farm fields (57% of farmland). Soils in the northern half of the upper-Nith Watershed are composed of clay loam and loam, contrasted by a mosaic of soils in the southern half of the watershed which are primarily loam and silty loam.

The annual precipitation for the upper-Nith Watershed is 958.3 mm yr^{-1} (2005 – 2014; Wellesley Dam meteorological station), with snow melt occurring intermittently throughout the winter months and during the early spring. The intermittent snow melts and spring freshet result in a high rate of discharge in the upper-Nith River throughout the winter and early spring months, with 76.82% of annual discharge occurring from November to April, and the remaining 23.18% of annual discharge occurring during the warmer growing season (May to October; 2005 – 2014; Environment Canada hydrometric station 02GA018).

The sediment yield of the upper-Nith River correlates well with discharge. A linear model relating sediment yield samples (n = 41; Environment Canada Station 16018403202; Appendix C Fig. C6) with discharge ($R^2 = 0.47$) estimated that 87.14% of sediment export occurred during the non-growing season (November to April) and the remaining 12.86% of sediment export occurred during the growing season (May to October). The 10-year average sediment yield of the upper-Nith Watershed was calculated at 22,131.35 t yr^{-1} (2005 – 2014; 0.41 t ha^{-1} yr^{-1}), with a more recent 5-year average of 19,943.07 t yr^{-1} (2010 – 2014; 0.37 t ha^{-1} yr^{-1}).

The upper-Nith Watershed has consistently experienced elevated levels of suspended sediments and nutrients (N and P) relative to the other sub-watersheds of the Grand River (Loomer and Cooke 2011). Nutrient concentrations measured at the outlet of the upper-Nith Watershed of unfiltered P (Environment Canada Station 16018403202) have exceeded water quality guidelines (guideline value is 0.03 mg L^{-1} to prevent eutrophication; Environment Canada, 2004) in 98% of samples (n = 47) between 2005 and 2014. Elevated levels of suspended sediments and P can be associated with eroded agricultural sediments, making the upper-Nith Watershed ideal for a case study on agricultural soil erosion and soil loss.

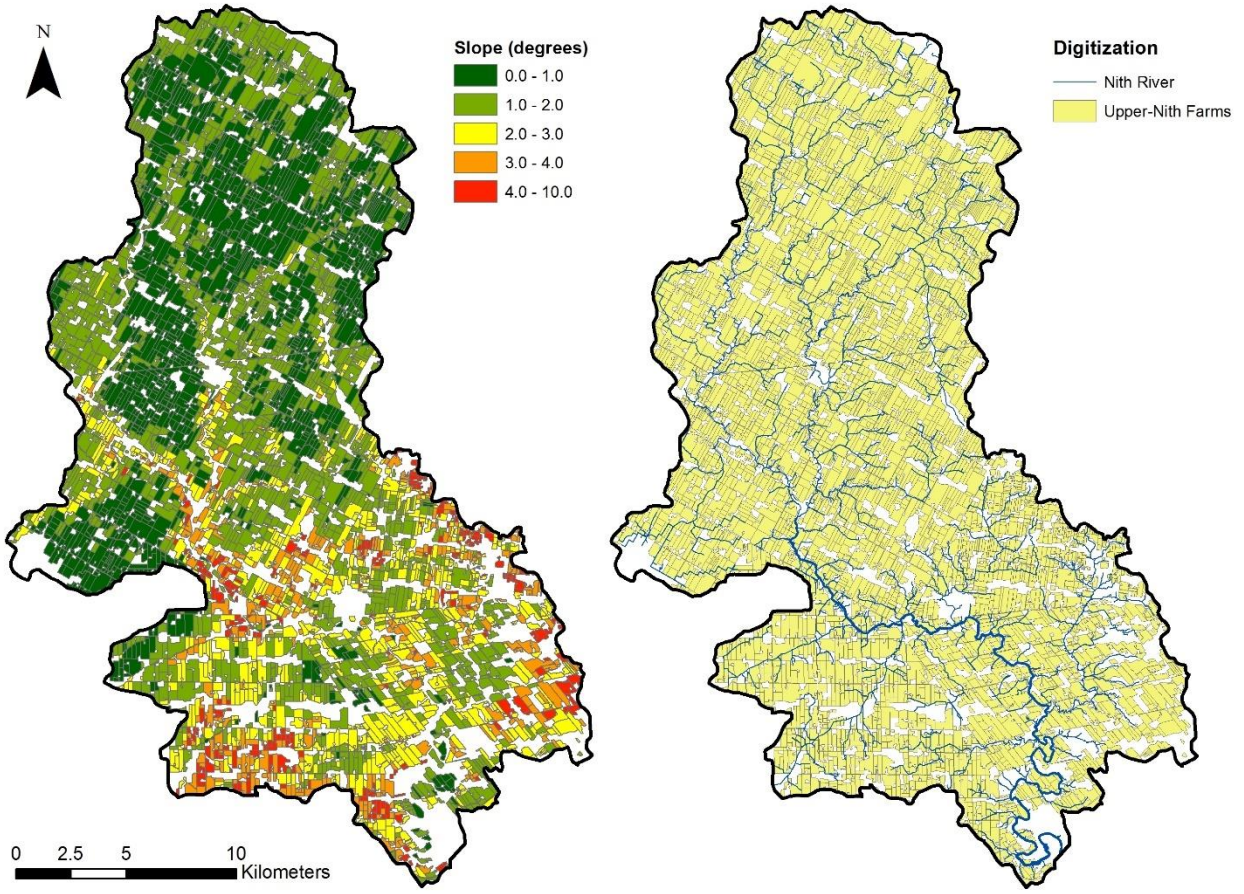

Fig. 6.1. Upper-Nith Watershed. Average farm field slope (4 m LiDAR DEM; left), and agricultural farm fields overlain by the Nith River and its tributaries (right). Farm field polygons were digitized using 2015 Southwestern Ontario Orthoimagery Project (SWOOP) airborne imagery.

6.2.2. Erosion Modelling

6.2.2.1. Soil Erosion: USLE

Our recommended modelling approach implements the USLE as outlined in Agricultural Handbook no. 537 to estimate a 5-year average erosion rate (2010 – 2014) for the upper-Nith Watershed. While most USLE studies use a raster-based model implementation, our recommended modelling approach uses a polygon-based discretization for calculating and summarizing results whereby each polygon is representative of an individual farm field and was manually digitized using 2015 Southwestern Ontario Orthoimagery Project (SWOOP) airborne imagery with a fixed scale of 1:4000 (Fig. 6.1). Each farm field was assigned a static K and LS-factor for our study period, an R-factor for each year, and a C-factor for each cropstage. The six USLE factors in our recommended modelling approach were calculated as follows:

Rainfall and runoff (R). The R-factor reflects the impacts that rainfall and runoff have on water erosion. The R-factor is a summation of the total kinetic storm energy times the maximum 30-minute rainfall intensity for all rainstorms in a given year (p. 5; Wischmeier and Smith 1978):

$$R = \sum_{i=1}^{m} (EI_{30})_i$$

where R is the annual rainfall and runoff factor (*MJ mm ha^{-1} h^{-1} yr^{-1}*), m is the total number of storms in a year, EI_{30} is the rainfall erosivity of a single storm event, i (MJ mm ha^{-1} hr^{-1}), calculated as the total kinetic energy of rainfall (E; MJ ha^{-1}) times the maximum 30-minute rainfall intensity (I_{30}; mm hr^{-1}). Storms are only included in R calculations that exceed 12.7 mm of precipitation. While events smaller than 12.7 mm in size can produce a runoff response if they occur on wet antecedent conditions, most erosion and nutrient loss events are associated with high magnitude rainfall events (e.g., Macrae et al. 2007a).

We calculated the rainfall erosivity of each storm event using hourly rainfall data collected from the Wellesley Dam meteorological station. The meteorological station is located in the central portion of the watershed and we assumed that the spatial distribution of rainfall was uniform over the entire watershed. Since the minimum requirement for calculating the I_{30} of each storm is 30-minute rainfall data and we only had hourly rainfall data, we used a relationship developed by Panagos et al. (2015b) to convert from 60-minute intensities to 30-minute intensities ($R_{30\ min}$ = 1.5597 x $R_{60\ min}$). This conversion was found to be a reasonable approximation for annual predictions by Meinen and Robinson (2021) for a field-scale USLE case study in the watershed, albeit with a poor characterization of the most intense rainfall events. We only recommend using this empirical-scaling approach in the absence of 30-minute rainfall data, since it may be a substantial source of uncertainty in modelling outcomes. Our 5-year average R-factor (1923 *MJ mm ha^{-1} h^{-1} yr^{-1}*) related very well to the long-term average R-factor calculated by the Ontario Ministry of Agriculture and Rural Affairs (1864 *MJ mm ha^{-1} h^{-1} yr^{-1}*; OMAFRA 2012).

Soil erodibility (K). The K-factor represents the susceptibility of different soil types to water erosion (p.10; Wischmeier and Smith 1978):

$$100K = (2.1M^{1.14}(10^{-4})(12-a) + 3.25(b-2) + 2.5(c-3)) \times 0.1317$$

where K is the soil erodibility factor (t ha h ha^{-1} MJ^{-1} mm^{-1}), M is the soil particle-size parameter (based on soil texture), *a* is percent organic matter, *b* is the soil-structure code, and *c* is the profile-permeability class.

To calculate the K-factor, the spatial location of soil textural classes (M) and other edaphic characteristics (a, b, c) were selected from the Ontario Soil Survey Complex polygon (1:50,000 scale; OMAFRA 2019). The Ontario Soil Survey Complex polygon was rasterized, and the K-value for each farm field polygon was calculated as the average of the K-factor raster within the polygon.

Slope-length factor (L). The L-factor represents the effect that the length of a hillslope has on water erosion. The USLE L-factor was developed to be applicable to planar hillslopes, i.e., the shape of the experimental erosion plots, and does not have any provision for complex topography (p. 12; Wischmeier and Smith 1978). Due to this simplification of topography, a common methodological challenge in up-scaling the USLE stems from the difficulty and subjectivity with calculating the L-factor in a GIS (Morgan and Nearing 2011).

The most common approach for up-scaling the L-factor involves using the concept of specific catchment areas (i.e., upslope area of a unit contour divided by the contour width) in lieu of planar hillslopes (e.g., Moore and Burch 1986, Griffin et al. 1988, Moore and Wilson 1992, Desmet and Govers 1996, Mitasova et al. 1996). When using the concept of specific catchment areas, two challenges are immediately presented that have the potential to introduce model input and user error: (1) the choice of spatial elevation dataset (i.e., grid cell size, accuracy), and (2) the methodology used for discretization of specific catchment areas. The standard approach for calculating specific catchment areas in a GIS is using the dataset with the finest spatial resolution, hydrologically conditioning the DEM, and using a GIS flow accumulation tool to delineate upslope areas (e.g., D8 algorithm; Jenson and Domingue 1988).

Algorithms like the D8 flow direction and D8 flow accumulation, typically used in a GIS for calculating specific catchment areas, are sensitive to topographic variation and require depression filling (i.e., hydrologic conditioning) to derive meaningful estimates of hydrological connectivity. However, when a DEM is fully hydrologically conditioned, all flow is assumed to be connected from any point in the landscape to the lowest point of elevation; there is no consideration of natural or anthropogenic barriers that inhibit flow or impede sediment movement (Fryirs et al. 2007). While hydrologic conditioning is prudent for many hydrological analyses, it removes the depositional cavities in the landscape, which increases the size of specific catchment areas by artificially increasing landscape connectivity and results in an overestimation of the L-factor.

For calculating the L-factor in our recommended modelling approach, we use the concept of specific catchment areas for up-scaling the L-factor and followed a three-step approach for discretizing specific catchment areas: (1) we clipped our DEM to our farm field polygon layer before calculating contributing areas to ensure that natural (e.g., wind breaks) and artificial (e.g., roadways) barriers between fields correctly inhibited flow paths, (2) we partially hydrologically conditioned our DEM (Z fill limit = 0.4 m) to remove spurious artefacts and small microtopographic depressions in the DEM while preserving larger topographic depressions where flow would be disconnected, and (3) calculated specific catchment areas using a D8 flow algorithm and D8 flow accumulation tool. For calculating the L-factor, we use the methodology of Griffin et al. (1988):

$$L = (\frac{A_s}{22.13})^m * (m + 1)$$

where L is the slope-length factor (unitless), A_s is the specific catchment area (upslope contributing area divided by the grid resolution), and m is a slope exponent (typically m = 0.4). The last part of the equation, i.e., m + 1, was introduced by Griffin et al. (1988) for predicting erosion at a point, e.g., for each grid cell on a DEM. Specific catchment areas were calculated using a 2 m LiDAR DEM for all agricultural land in the watershed; the 2 m LiDAR DEM was the highest-resolution DEM available for our watershed.

The slope exponent m represents the impacts that slope gradient has on surface runoff and is constrained to a range of values between 0.4 – 0.6. We adjusted the value within this range from 0.4, which underestimated the L-factor by 35 – 45% relative to the USLE methodology in Agricultural Handbook no. 537 (tested on 20 farm fields; p. 12-15; Wischmeier and Smith 1978), to 0.6, which provided the closest alignment with the original USLE methodology (± 15%). Once we calibrated the slope exponent, each farm field polygon was assigned an L-factor based on the average of the L-factor raster for each specific catchment area within the farm field polygon.

Slope steepness factor (S). The S-factor represents the impact that slope gradient has on water erosion. Since the USLE was developed on planar one-dimensional erosion plots, the S-factor needs to be reconceptualized for up-scaling to larger spatial extents. Similar to the L-factor, the choice of spatial elevation dataset (e.g., cell size, accuracy) and methodological implementation of the S-factor will have an impact on soil erosion estimates. Decreasing the spatial resolution of topographic data, i.e., using coarser data, will decrease slope steepness estimates; fine spatial resolutions (e.g., LiDAR DEMs) model the microtopography of the landscape while coarse DEMs (e.g., satellite DEMs) model an averaged macrotopography.

To calculate the S-factor, we selectively chose to use a 4 m DEM (up-sampled 2 m LiDAR DEM) as the most appropriate resolution for calculating the average slope steepness of specific catchment areas. Coarse DEMs (e.g., > 10 m) poorly represented slopes on small agricultural fields, while finer DEMs (e.g., < 2 m) captured the slope of microtopography rather than the predominant slope of the macrotopography. We calculated the S-factor in our recommended modelling approach based on the average slope of each catchment area using the methodology of Moore and Burch (1986):

$$S = \left(\frac{\sin\theta}{0.0896}\right)^{n}$$

where θ is the slope of the catchment area, and n is a slope exponent (n = 1.3). Each farm field polygon was assigned an S-factor based on the average of the S-factor raster within the polygon.

Cover and management (C). The effects of farm management on soil erodibility varies greatly throughout a year and soil is more susceptible to water erosion during seedbed preparation than when a mature crop is present (Wischmeier and Smith 1978). The temporal variability in soil loss during each management cycle is partly a function of rainfall erosivity, crop cover, and farm management (e.g., tillage). The representation of crop cover and management in the USLE, i.e., the C-factor, is equal to the soil loss ratio for a given cropping and tillage system multiplied by the percentage of annual EI (E, kinetic energy of rainfall; I, rainfall intensity) for a specific sub-annual timestep. The USLE operationalizes the C-factor for individual cropstages (i.e., six distinct periods of crop growth) that are represented in Agricultural Handbook no. 537 as: (1) rough fallow, (2) seedbed preparation, (3) crop establishment, (4) crop development, (5) maturing crop, and (6) residue or stubble.

A common approach for calculating the C-factor is selecting a lumped annual value using, for example, annual C-factor tables (e.g., Table C-3a in the RUSLEFAC handbook; p. 91, Wall et al. 2002). However, since the C-factor is a time-integrated factor, a lumped annual value fails to represent the varying relationships between rainfall intensity, land management, and crop cover throughout the year. While the USLE can be parameterized and yield accurate results using an annual C-factor selected from supplementary resources, the annual C-factor tables created by the Soil Conservation Service and other agencies are applicable to a specific climate, time period, and field management regime (e.g., primary tillage, secondary tillage, planting and harvest dates, etc.); recalculating a time-integrated C-factor value specific to a specific study area should always yield more accurate results.

Since farm fields can have different planting and harvest dates, more than one crop within a year (e.g., winter wheat following soybeans), and different land management practices, the choice of how these processes are captured will constrain the accuracy of the C-factor. When the C-factor is calculated using a GIS, land cover data derived from remotely sensed imagery are often used. While the spatial coverage and resolution of these data are typically sufficient for most applications, land cover data are typically annual and automated image classification techniques cannot identify land management activities (e.g., tillage types). Therefore, most studies calculate an annual C-factor (e.g., MLC, Singh and Panda 2017; NDVI, Grimm et al. 2003; unsupervised classification, Hui et al. 2010) and ignore variation in tillage, planting and harvest dates, or crop rotations.

To represent the human and natural component of the C-factor in our recommended modelling approach, we calculated the C-factor for each cropstage as a function of crop type, crop rotation, planting and harvest dates, tillage type, the respective soil loss ratios for each management cycle (p. 22 – 26; Wischmeier and Smith 1978), and the percentage of annual EI_{30} during each cropstage. In lieu of using annual land-cover data, we used a Monte-Carlo approach to generate plausible realizations of each agricultural system. To generate these realizations, we inferred land management practices using the 2016 Census of Agriculture in Canada (based on the Wilmot, Wellesley, and Perth East counties). The Census data were summarized by four dominant crop types (corn, soybean, alfalfa, wheat), three types of tillage (no till, conservation till, conventional till), and two types of agricultural land use (pasture, cropland; Table 6.1). The four crops comprised 88.5% of all cropland in the watershed with the remaining 11.5% of cropland being either ill-defined (e.g., mixed grains) or not have corresponding soil loss ratios in the agricultural handbook (e.g., sunflowers). We reclassified the remaining 11.5% crops to one of the four dominant crop types based on similarity (e.g., mixed grains assigned to wheat). To accommodate for this shift in crop practices, land area under no-till seeding was decreased to only winter wheat applications, which is the most common practice in the watershed for winter wheat. The decrease in no-till was balanced by an increase in conservation tillage across the other three dominant crop types. The similarity in crop types minimizes the effects of these amendments to accommodate data limitations on our soil erosion estimates.

Supporting practices (P). The P-factor represents the effects that different cropland practices (e.g., contouring or terracing) have on water erosion. No additional supporting practices were present in the watershed, so the P-factor was left at the default of 1 which represents no additional supporting practices.

Soil erosion (RKCLSP). Our recommended modelling approach uses a polygon-based discretization for calculating the average soil erosion rate of the upper-Nith Watershed, where the watershed is conceptualized as a collection of farm fields. Since the data in the Canadian Census of Agriculture is summarized for each county, rather than spatially for each field, a Monte-Carlo simulation was used to randomly assign each farm field polygon a cover and management practice based on the proportion of occurrences for each in the watershed. While this approach does not allow us to have a deterministic outcome, it has the advantage of being able to identify the most erosive farm fields in the watershed and isolate what specific management activities are associated with unsustainable rates of soil erosion for each farm field. A prescriptive approach for land management activities is largely prohibitive at the watershed scale.

The Monte-Carlo simulation was run 100,000 times per study year to generate a comprehensive distribution of potential soil erosion estimates for the watershed by multiplying the USLE factors of each farm field together using each possible arrangement of crop type, tillage, and land use. For each simulated year, the estimated soil erosion value for each farm field was stochastically modified by ± 20% to coincide with the natural variation in empirical soil erosion measurements (e.g., 20% variation in replicate erosion plots; Wendt et al. 1986).

Table 6.1. Tillage practices, land use, and the four main crop types in the Wilmot, Wellesley, and Perth East counties taken from the 2016 Census of Agriculture in Canada. The three counties cover the upper-Nith Watershed and additional agricultural land to the west.

Crop Types	Area (ha)	Original	Monte-Carlo Composition
Corn	28,116	31.3%	35.4%
Soybean	18,948	21.1%	23.9%
Alfalfa, Alfalfa mixtures	17,742	19.8%	22.3%
Wheat	14,636	16.3%	18.4%
Other	10,318	11.5%	0.0%
Land Use			
Cropland	89,760	94.7%	94.7%
Tame/seeded pasture	3,041	3.2%	3.2%
Natural land for pasture	2,013	2.1%	2.1%
Tillage			
No-till seeding	17,319	22.7%	18.4%
Conservation tillage	16,851	22.1%	26.4%
Conventional tillage	42,066	55.2%	55.2%

6.2.2.2. Soil Loss: USLE and Sediment Delivery Ratios

Conservation efforts are often focussed on ameliorating the off-site impacts of agricultural soil loss, e.g., pollution of adjacent surface waters, rather than on-site sediment redistribution from soil erosion. While sediment yield from a watershed is impacted by the amount of arable land and cropland within the watershed (Vanmaercke et al. 2015) and it is well established that agricultural activities accelerate the rate of soil erosion (Montgomery 2007), extending USLE results outside of the models intended design space to predict soil loss from fields to waterways with a sediment delivery ratio (SDR) is a dubious task. Relating gross erosion to sediment yield has been classically done using a single SDR whereby the fraction of gross erosion that is transported out of a watershed is expressed as:

$$SDR = \frac{Y}{E}$$

where Y is the sediment yield at the watershed outlet, and E is the gross erosion of the watershed. E is typically represented by USLE soil erosion estimates (e.g., Fistikoglu and Harmancioglu

2002, Amore et al. 2004, Pandey et al. 2007, Hui et al. 2010, Rizeei et al. 2016, Singh and Panda 2017) and the SDR indicates what percentage of eroded agricultural sediments are leaving the watershed (USDA 1971).

The first problem with using the USLE to represent the gross erosion of a watershed (E) is that agricultural sediments are not the only source of sediments contributing to sediment yield and measurements of sediment yield are only reflective of the fine material transported in the waterway. Waterways have a natural baseline sediment yield that is augmented not only by eroded agricultural sediments, but also sediment from subsurface tile drainage, in-stream erosion, and changes of sediment storage within the system itself. Furthermore, agricultural sediments are a highly variable component of watershed sediment budgets. It has been estimated that in tile-drained agricultural systems, sediment from field drains can account for 28 - 29% (Walling et al. 2002) to 51 - 55% (Walling et al. 2002) of the catchment sediment yield and can be a significant source of particulate P (Macrae et al. 2007b; King et al. 2015), while in other landscapes, in-stream erosion can be the dominant supplier of sediment and nutrients (e.g., 90 – 94%; Kronvang et al. 2013).

The second problem with using the USLE with an SDR to represent the delivery of eroded agricultural sediments to waterways is that not all eroded sediments have an equal probability of being conveyed to a catchment outlet. A distributed approach is required to capture the field-to-field variation in landscape conditions that drive sediment delivery to waterways. Each agricultural field has a unique delivery potential based on its relative position to a waterway and the filtering efficiency of the adjacent riparian zone. We can express the soil loss from fields to waterways of each agricultural field, *f*, as a function of each catchment within the field:

$$SDR_f = \frac{\sum_{j=1}^{n} E_j F_j}{\sum_{j=1}^{n} E_j + \sum_{i=1}^{m} E_i}$$

where SDR_f is the sediment delivery ratio of a farm field to a waterway, E is the soil erosion rate (t) of an agricultural catchment, F is the filtering efficiency (%) of the riparian zone, *j* is an index for the number of catchments on a farm field that have a potential to produce soil loss to waterways, and *i* is an index for the number of catchments on a farm field that are unlikely to produce soil loss to waterways (i.e., the catchment does not direct runoff towards a waterway).

To calculate the SDR_f of each field, our recommended modelling approach uses a distributed approach whereby E is the USLE soil erosion rate of an agricultural catchment within a field, the average filtering efficiency of riparian zones is defined by Yuan et al. (2009), and *j* and

i are calculated in ArcGIS v10.6.1 based on the direction of overland flow and proximity to waterways (Appendix C). When using the USLE to represent the soil erosion rate of a farm field, it is important to note that the USLE does not account for depositional processes at the bottom of a hillslope, so there will be a disconnect between the soil erosion rate and rate of soil loss from the field. To account for this, we re-ran our Monte-Carlo simulation to calculate soil loss from farm fields to waterways using a stochastic estimate of in-field depositional processes (-25 to -75%) and additionally included a stochastic estimate of the filtering efficiency of riparian zones (± 20%; based on Yuan et al. 2009). The range of these stochastic estimates illustrate considerable uncertainty associated with predicting soil loss to waterways with USLE, which is beyond its intended design. However, the stochasticity is necessary to derive a range of quantitative outcomes that capture the behaviour of the agricultural system and do not incorrectly emphasize a single estimate.

6.2.3. Variability in Model Outcomes

Since there is no standardized and accredited setup for up-scaling the USLE, different methodological implementations for up-scaling USLE factors will contribute to uncertainty in model outcomes. While certain up-scaling approaches are conceptually poor (e.g., calculating the C-factor using a single year of airborne imagery), it is difficult to provide guidance on what constitutes a correctly up-scaled implementation of each USLE factor. We focus on quantifying the variability in model outcomes, rather than error or uncertainty, because the size of our study area precludes a validation of erosion rates. To quantify the variability in model outcomes, we compare the recommended modelling approach from our case study with: (1) different design choices for implementing individual USLE factors, (2) a model implementation synonymous with the most common approach in a sampling of literature, and (3) national (SoilERI, Clearwater et al. 2016) and global studies on soil erosion (Borrelli et al. 2017).

To select different design choices for implementing individual USLE factors, we searched Google Scholar with the keywords “USLE”, “Watershed”, and “Erosion” to understand the most commonly used USLE methodologies among the first ten relevant papers (Fistikoglu and Harmancioglu 2002; Amore et al. 2004; Erdogan et al. 2007; Pandey et al. 2007; Dabral et al. 2008; Hui et al. 2010; Devatha et al. 2015; Belasri and Lakhouili 2016; Rizeei et al. 2016; Singh and Panda 2017), and supplemented this with several hand-selected papers (Van der Knijff et al. 1999; Grimm et al. 2003; Prasuhn et al. 2013; SoilERI, Clearwater et al. 2016; Borrelli et al. 2017). These publications have been cited on Google Scholar a total of 2269 times and use the USLE in a GIS environment to evaluate distributed soil erosion rates at large spatial extents.

6.3. Results

6.3.1. Soil Erosion: USLE

For contextualizing our results, the rate of natural soil regeneration is less than 1 t ha^{-1} yr^{-1} (Montgomery, 2007), with most conservation efforts focusing on keeping soil erosion rates under 5 to 11 t ha^{-1} yr^{-1} (e.g., Ontario guidelines from OMAFRA are < 6.7 t ha^{-1} yr^{-1}). Our recommended modelling approach, summarized across 100,000 Monte-Carlo simulations, calculated a 5-year average soil erosion rate of 6.66 t ha^{-1} yr^{-1} (Table 6.2) for the upper-Nith watershed, with a lower bound of 5.22 t ha^{-1} yr^{-1} and an upper bound of 8.18 t ha^{-1} yr^{-1}. In this context, soil erosion represents soil loss from hillslopes to anywhere in the landscape, including both on-site sediment redistribution and off-site soil loss.

Investigating the effects of a conventional tillage versus a conservation tillage demonstrated a substantial reduction in erosion rates. When using a conventional tillage system for the watershed (i.e., moldboard corn, moldboard soybean, no-till winter wheat; e.g., Meinen and Robinson 2021), we identified that 1421 farm fields (29.18% of agricultural land) would have an unsustainable rate of soil erosion, i.e., > 11.2 t ha^{-1} yr^{-1}, while under a conservation tillage system (i.e., chisel corn, chisel soybean, no-till winter wheat) only 377 farm fields (6.57% of agricultural land) would have a soil erosion rate greater than 11.2 t ha^{-1} yr^{-1} (Table 6.3). The moldboard plow inverts the topsoil, burying the majority of crop residue and leaving a rough soil surface, while the chisel plow breaks up the soil surface but does not invert the topsoil like the moldboard plow. Moldboard plows are typically used at a greater depth than chisel plows and do not leave sufficient biomass on the field surface to protect against water erosion.

The average of all our Monte-Carlo simulations calculated that 805 farm fields (15.55% of agricultural land) are likely eroding at a rate greater than 11.2 t ha^{-1} yr^{-1}. The northern half of the watershed is characterized by very low erosion rates, whereas fields in the south-western portion of the watershed have high soil erosion rates resulting from steeper slopes and soils more susceptible to water erosion (i.e., silty loams; Fig. 6.2a). Conservation efforts focussed on the fields that have an unsustainable rate of soil erosion (> 11.2 t ha^{-1} yr^{-1}; Fig 6.2a) would ameliorate the economic and environmental impact of soil erosion, while conservation efforts focussed on the northern half of the watershed would likely have no significance.

Table 6.2. USLE soil erosion rates for the upper-Nith Watershed.

Soil Erosion	2010	2011	2012	2013	2014	5-year Average
Mean (t ha^{-1} yr^{-1})	4.50	5.29	3.19	8.89	11.44	6.66
St. dev (t ha^{-1} yr^{-1})	0.53	0.62	0.37	1.04	1.34	0.77
Min (t ha^{-1} yr^{-1})	3.44	3.99	2.43	6.81	8.70	5.22
Max (t ha^{-1} yr^{-1})	5.67	6.82	4.00	11.19	14.48	8.18

Table 6.3. Soil erosion categories for each farm field in the upper-Nith Watershed using different crop and management rotations. A conventional rotation is moldboard (M) corn, moldboard (M) soybean, and no-till winter wheat (average C-factor: 0.327). A standard conservation rotation is chisel (C) corn, chisel (C) soybean, and no-till winter wheat (average C-factor: 0.147). Both the conventional rotation and conservation rotation have a right-skewed distribution (skewness: 2.96).

Erosion Category	Tillage	USLE Soil Erosion [t ha^{-1} yr^{-1}]	Total Area [ha]	Number of Fields
Negligible	M, M, no-till	< 2.2	1051	212
Tolerable	M, M, no-till	2.2 – 6.7	17987	2088
Tolerable - unsustainable	M, M, no-till	6.7 – 11.2	9084	973
Unsustainable	M, M, no-till	11.2 – 22.4	8217	950
Unsustainable	M, M, no-till	> 22.4	3369	471
Negligible	C, C, no-till	< 2.2	12332	1560
Tolerable	C, C, no-till	2.2 – 6.7	19614	2162
Tolerable - unsustainable	C, C, no-till	6.7 – 11.2	5154	595
Unsustainable	C, C, no-till	11.2 – 22.4	2361	318
Unsustainable	C, C, no-till	> 22.4	246	59

Fig. 6.2. Upper-Nith Watershed modelling results for each farm field: (a) USLE soil erosion, and (b) USLE/SDR_f soil loss to waterways. Individual rates of soil erosion and soil loss per field will vary depending on the land management practices specific to that site. Both graphics use an average C-factor value for visualization. White areas in the map represent all non-agricultural land uses (e.g., urban, forest, roadways).

6.3.2. Soil Loss: USLE and Sediment Delivery Ratios

Soil erosion has on-site impacts (e.g., tillage erosion affecting crop yield; Lobb et al. 1995, Van oost et al. 2006), while soil loss has both on-site (e.g., lost topsoil affecting crop yield; den Biggelaar et al. 2001) and off-site impacts (e.g., eutrophication of local water bodies; Michalak et al. 2013). To estimate soil loss from fields to waterways, we applied a field-scale SDR_f to our

USLE results and summarized the results across 100,000 Monte-Carlo simulations. Our modelling results estimated that soil loss from fields to waterways ranged from 6,083 – 12,256 t yr^{-1} (mean ± one standard deviation; SDR_f: 2.30 – 4.63%), with a 5-year average soil loss of 9,170 t yr^{-1} (SDR: 3.47%; 0.23 t ha^{-1} yr^{-1}; Table 6.4). Field-scale results showcased that the 20% of fields with the highest rates of soil loss were responsible for 77% of the total soil loss, with the tail end of this distribution contributing the majority of sediments (Fig. 6.2b); a large portion of farm fields with high erosion rates had low estimates of soil loss since they were disconnected from waterways (e.g., Fig. 6.3b, c).

For estimating the environmental impact of soil loss from agricultural fields to waterways relative to other sources of sediment we compared the estimated soil loss from farm fields to the sediment yield measured at the outlet of the upper-Nith Watershed. If we assume that all the sediment that entered the Nith River is transient, eroded agricultural sediments entrained and transported via overland flow would represent a maximum of 30.50 – 61.45% of the watershed's sediment yield (SDR_f: 2.30 – 4.63%) from 2010 – 2014. Based on a qualitative visual analysis of fields in the watershed, we hypothesize that in-field depositional processes are substantial and that the soil loss is likely closer to the lower-bound.

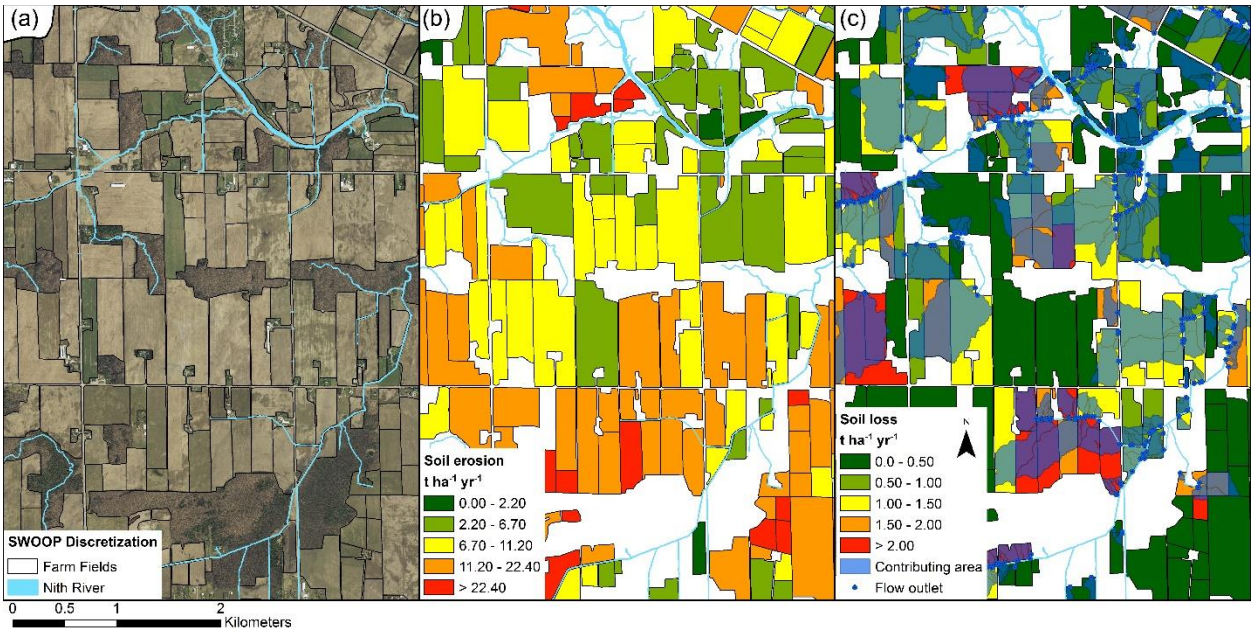

Fig. 6.3. (a) 2015 SWOOP imagery overlain by our discretization of farm fields, (b) USLE soil erosion results for each farm field, and (c) USLE/SDR_f soil loss to waterways from each farm field with contributing areas and flow outlets to waterways highlighted in blue. White areas in the map represent all non-agricultural land uses (e.g., urban, forest, roadways).

Table 6.4. Total modelled soil erosion (USLE) and soil loss (USLE/SDR_f). Modelled soil erosion indicates soil loss from agricultural hillslopes to anywhere on the landscape, modelled soil loss indicates soil loss from agricultural hillslopes to waterways, and measured sediment yield is from all sources at the outlet of the upper-Nith Watershed. Modelled soil erosion has a uniform distribution (skewness: 0.01) while modelled soil loss has a bell-shaped symmetric distribution with a slight right skew (skewness: 0.34).

	2010	**2011**	**2012**	**2013**	**2014**	**5-year mean**
Modelled soil erosion						
Mean (t yr^{-1})	178,636	210,085	126,631	352,996	454,373	264,568
St dev. (t yr^{-1})	20,874	24,601	14,765	41,169	53,124	30,728
Modelled soil loss						
Mean (t yr^{-1})	6,194	7,295	4,398	12,258	15,748	9,170
St. dev. (t yr^{-1})	2,088	2,465	1,477	4,119	5,314	3,087
Measured sediment yield (t yr^{-1}) *	9,431	26,560	7,506	32,364	23,854	19,943

*measured sediment yield is interpolated based on 41 samples (See Appendix C Fig. C6; Environment Canada Station 16018403202).

6.3.3. Variability in model outcomes

6.3.3.1. Different design choices for individual USLE factors

To quantify the variability in model outcomes for different implementations of USLE factors, we recalculated the average soil erosion rate for the upper-Nith Watershed using different design choices for individual USLE factors commensurate with the most common approaches in literature. The outcome of using different design choices in a USLE implementation led to a range in soil erosion estimates of 3.04 - 11.02 t ha^{-1} yr^{-1} for the upper-Nith Watershed, with significant spatial discrepancies between model outcomes (Table 6.5). This high level of variability can be constrained and challenges with equifinality ameliorated by making improved up-scaling design choices, for example:

C-factor. A correct implementation of the C-factor should include land use, crop type, tillage type, and crop rotations; a more detailed time-integrated C-factor should also include planting, harvest, and crop stage dates. When using simple look-up tables that did not include a human management component (i.e., they only represented crop types), there was a range in model outcomes of 9.44 - 9.81 t ha^{-1} yr^{-1}, which over-predicted soil erosion rates relative to our recommended modelling approach, i.e., 6.66 t ha^{-1} yr^{-1}. The uncertainty of using look-up tables is best exemplified when you consider that land management practices are what drive soil erosion

in agricultural systems; not including the human dimension indicates that the model user has no understanding of the impacts of the human component of agriculture. The polygon-based discretization of the landscape used in our recommended modelling approach, rather than a raster-based discretization, is a pragmatic approach for spatially assigning the human dimension of the C-factor on a field-by-field basis.

L-factor. In lieu of a topographic-based delineation (e.g., using a GIS) of specific catchment areas, a constant hillslope length can be used to avoid propagating model uncertainty if the model user only has access to coarse resolution DEMs. Using constant hillslope lengths of 50 m and 122 m led to model outcomes of 5.76 t ha^{-1} yr^{-1} and 8.22 t ha^{-1} yr^{-1}, respectively, with both approaches having a high spatial correlation with our recommended modelling approach. Both the range in model outcomes, i.e., 6.18 – 11.02 t ha^{-1} yr^{-1}, and spatial correlations were much poorer when a distributed GIS approach was used with coarse DEMs relative to our recommended modelling approach.

DEM resolution. Since DEM resolution has a significant impact on model uncertainty and is used to calculate both the L-factor and S-factor, we recommend using a DEM resolution of no less than 10 m for an accurate discretization of specific catchment areas and calculation of slope gradients. Coarse DEM resolutions (e.g., 30 m) are unable to model the slope of small topographically complex farm fields (e.g., 5 ha) and will lead to a poor discretization of specific catchment areas. Implementing the L-factor and S-factor with 90 m DEMs led to model outcomes of 11.02 t ha^{-1} yr^{-1} and 3.04 t ha^{-1} yr^{-1}, respectively, and was the largest source of uncertainty in modelling outcomes compared to our recommended modelling approach. Coarse DEMs may be appropriate for regions that are less topographically complex with larger farm field sizes, but they were a poor choice for modelling the upper-Nith Watershed.

Table 6.5. Different implementations of USLE factors for the upper-Nith Watershed. The percent difference and correlation coefficients are relative to our recommended modelling approach. The L-factor and S-factor use the GIS implementation of Moore and Burch (1986). The RUSLEFAC is the RUSLE handbook for Canada (Wall et al. 2002). Each of our model implementations had a right-skewed distribution (skewness ≈ 3). The worst modelling approaches relative to our recommended approach are highlighted in bold font.

USLE Factor	Details	Soil erosion ($t\ ha^{-1}\ yr^{-1}$)	Difference (%)	Correlation (field-scale)
	Recommended modelling approach	6.66	N/A	N/A
R-factor	RUSLEFAC look-up table (R = 1500)	4.31	35.3	1.00
R-factor	OMAFRA look-up table (R = 1864)	6.46	3.0	1.00
C-factor	OMAFRA look-up table, spatially assigned using Agricultural Census data with a Monte-Carlo simulation	9.44	41.7	0.94
C-factor	RUSLEFAC look-up table, spatially assigned using Agricultural Census data with a Monte-Carlo simulation	9.81	47.3	0.95
C-factor	RUSLEFAC look-up table, spatially assigned using the 2015 AAFC crop inventory raster	9.78	46.8	N/A*
L-factor	10 m (resampled LiDAR DEM) hydrologically conditioned, m = 0.4	6.18	7.2	0.71
L-factor	30 m (provincial DEM) hydrologically conditioned, m = 0.4	8.17	22.7	0.34
L-factor	90 m (resampled provincial DEM) hydrologically conditioned, m = 0.4	**11.02**	**65.5**	**0.27**
L-factor	constant hillslope length of 50 m, m = 0.4	5.76	13.5	0.91
L-factor	constant hillslope length of 122 m, m = 0.4	8.22	23.4	0.91
S-factor	10 m (resampled LiDAR DEM), n = 1.3	6.13	8.0	0.96
S-factor	30 m (provincial DEM), n = 1.3	4.35	34.7	0.89
S-factor	90 m (resampled provincial DEM), n = 1.3	3.04	54.4	0.86
RCKLSP	Literature-based model	4.05	39.2	N/A*
RCKLSP	National model; Clearwater et al. 2016	**15.73**	**136.2**	**N/A***
RCKLSP	Global model; Borrelli et al. 2017	**0.72**	**89.2**	**N/A***

*correlation coefficients cannot be computed since land use and management are prescribed in this approach and our recommended modelling approach randomly assigns land use and management using a Monte-Carlo simulation.

6.3.3.2. Literature-based model implementation

Using the most commonly represented methodology in our sampling of literature, i.e., a literature-based model implementation, we calculated a 30 m raster of annual long-term rates of soil erosion per pixel in the upper-Nith Watershed. For the literature-based model implementation, the R-factor was selected from an annual isoerodent map for Ontario (Figure R-1, p.46; Wall et al. 2002), annual C-factors were selected from a look-up table in the RUSLEFAC handbook (Table C-3a; p. 91; Wall et al. 2002) and spatially assigned using the 2015 30 m AAFC crop inventory raster (Fisette et al. 2013; crop types and land cover classes were derived from Landsat-8 optical imagery and RADARSAT-2 radar imagery), K-factors were selected from a table provided by OMAFRA and spatially assigned using the Ontario Soil Survey Complex polygon, the L-factor was calculated on a 30 m fully hydrologically conditioned DEM (provincial DEM) using the approach of Moore and Burch (1986; m = 0.4), and the S-factor was calculated on a 30 m DEM (provincial DEM) using the approach of Moore and Burch (1986; n = 1.3).

The literature-based implementation of the USLE calculated an average erosion rate of 4.05 t ha^{-1} yr^{-1} for the upper-Nith Watershed. The similarity in the estimated average soil erosion rates of the literature-based outcome (4.05 t ha^{-1} yr^{-1}) relative to our recommended modelling approach (6.66 t ha^{-1} yr^{-1}; Table 6.5) demonstrates that vastly different model implementation of the USLE can have similar results. The literature-based outcome had a compensatory effect whereby two factors (S-factor, R-factor) were underestimated, and two factors (L-factor, C-factor) were overestimated relative to our recommended modelling approach. This compensatory effect can lead to poor spatial outcomes and challenges with equifinality. For example, our recommended modelling approach estimated that, on average, 805 farm fields would be eroding at an unsustainable rate, i.e., > 11.2 t ha^{-1} yr^{-1}. The literature-based approach, when summarized at the field level, identified that 419 farm fields would be eroding at an unsustainable rate, with only 60.4% of those fields being the same as our recommended modelling approach. A simple comparison between the literature-based L-factor and the L-factor from our recommended modelling approach shows little spatial correspondence, i.e., spatial correlation of 0.34 at the farm-field scale, and a visual comparison shows significant discrepancies between model outcomes (Fig. 6.4). The uncertainty associated with the literature-based approach relative to our recommended modelling approach can be further exemplified by the C-factor. In our recommended modelling approach, we used a time-integrated C-factor where each field was assigned a detailed description of crop types, crop rotations, planting and harvest dates based on crop type, tillage types, and land use, for each cropstage; the literature-based approach

calculated an annual C-factor from a single year of airborne imagery, i.e., each cell in the raster was assigned a crop type and the remaining management practices were estimated. There is no understanding of the land management practices that drive soil erosion in the literature-based approach; both the human and natural components to be fully modelled for a meaningful model outcome.

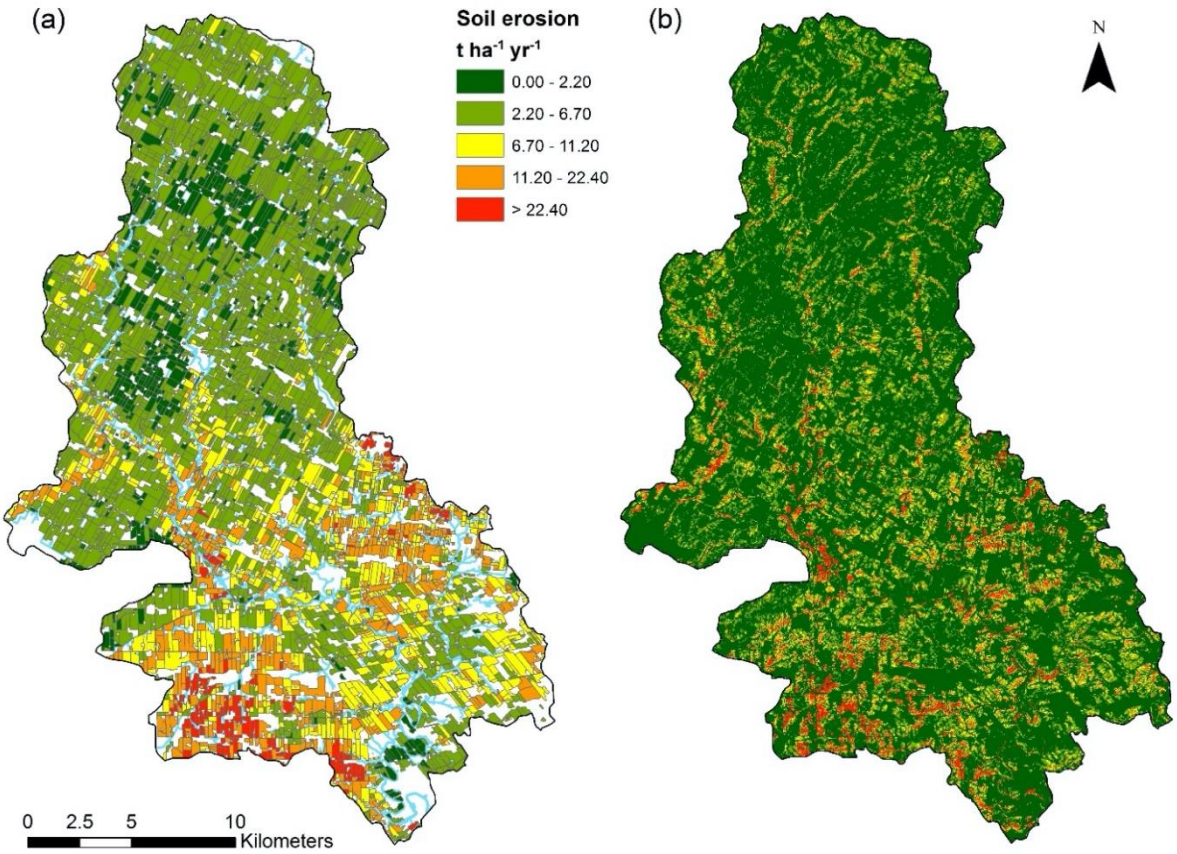

Fig. 6.4. Upper-Nith Watershed modelling results: (a) our recommended modelling approach depicting the soil erosion rate for each farm field using an average C-factor value for visualization, and (b) a literature-based implementation depicting the average soil erosion rate of each 30 m pixel. Erosion rates > 11.2 t ha^{-1} yr^{-1} are considered unsustainable.

6.3.3.3. National and global studies

To further emphasize the disparity among different USLE applications and model implementations, we compared the results from our recommended modelling approach to the most rigorous national estimate of soil loss in Canada, the SoilERI, created by AAFC, Canada (Clearwater et al. 2016). The SoilERI represents soil loss from both water and tillage erosion and is calculated using Soil Landscape of Canada (SLC) polygons and a combination of the USLE and RUSLE2. When we aggregated the SoilERI to the same spatial aggregation as our recommended modelling approach (i.e., summarized the values for each farm field polygon), the

SoilERI over predicted the rate of soil erosion by 9.07 t ha^{-1} yr^{-1} (136.2% difference) relative to our recommended modelling approach (SoilERI estimates: 15.73 t ha^{-1} yr^{-1}; recommended modelling approach: 6.66 t ha^{-1} yr^{-1}). This is sharply contrasted by the global study of Borrelli et al. 2017) that underpredicted soil loss by 5.94 t ha^{-1} yr^{-1} (89.2% difference) in the upper-Nith watershed relative to our recommended modelling approach (Borrelli et al. 2017 estimate of 0.72 t ha^{-1} yr^{-1}). While it is important to acknowledge the considerable data constraints of national and global erosion estimates and that the SoilERI estimates of soil erosion will be marginally higher since they include a tillage erosion component, there was a significant disparity between all three USLE applications despite the same model being applied.

6.4. Discussion

6.4.1. Why the USLE?

For an environmental problem to be a prominent issue on the world stage and to garner the interest of conservation groups, rigorous measurements are needed to quantify the severity of the problem, socio-economic drivers, and associated costs. Soil erosion is widely recognized as a global problem (e.g., Status of The World's Soil Resources Report; FAO 2015), whereby soil erosion has been identified as one of the main threats to agricultural sustainability, but somewhat paradoxically, these conclusions are drawn from a paucity of data. The sentiments of Trimble and Crosson (2000) aptly reflect why this is a problem, "It is questionable whether there has ever been another perceived public problem for which so much time, effort, and money were spent in light of so little scientific evidence" (p. 248). These sentiments are echoed by Boardman (2006), "We have difficulty in the recognition, description and quantification of erosion, and limited information on the magnitude and frequency of events that cause erosion… The inadequacy and frequent misuse of existing data leaves us open to the charge of exaggeration of the erosion problem (a la Lomborg)" (p. 73). The conclusions drawn from the paucity of data on soil erosion may be perceived as pragmatic to garner public interest, albeit rightly open to criticism.

Criticisms stem primarily from the generalization of plot-based erosion measurements that are extremely difficult to source and not suitable for generalization. For example, Pimentel (2006) is well cited (1001 citations on Google Scholar) and identifies a worldwide erosion rate of 30 t ha^{-1} yr^{-1}, sourcing Pimentel et al. (1995) for the erosion estimate. Pimentel et al. (1995) cites Barrows (1991) for an erosion rate for Asia, Africa, and South America of 30 to 40 tons ha^{-1} yr^{-1}, and an erosion rate of 17 tons ha^{-1} yr^{-1} for the United States and Europe. However, Barrows (1991) estimate is derived from Lal et al. (1989; Table III) using a synthesis of research from 24 countries that includes the following disclaimer: "The data used in this table comes from a wide range of

sources and is derived through a wide range of sampling methodologies; it is therefore not standardized and serves as only a general indication" (Table 10.6; Barrows 1991). While this synthesis of research is useful and informative, the soil erosion rates found in Table III of Lal et al. (1989) are sourced from eight different documents (Barber 1983, Fournier 1967, Humphreys 1984, Lal 1976a, Lal 1976b, Ngatunga et al. 1984, Roose 1977, World Resources Institute 1986) which are mostly inaccessible, and the few that are available were based on small plot-based studies (e.g., Tanzania; Ngatunga et al. 1984). Lal et al. (1989) warn that "the data obtained from small plots are often not comparable… misinterpretation and erroneous conclusions are major worries when using such data" (p. 58). While the nesting of sources and lack of citing primary literature is a concern, the issue lies in the use of data that has explicitly cautioned its use and lack of comparability and scalability.

A similar example is offered when searching for a primary source from the World Resources Institute (1986) citation in Table III of Lal et al. (1989). The World Resources Institute (1986; Table 5.5, p. 270) sources a compiled list of cropland soil erosion rates from the World Resources Institute and International Institute for Environment and Development which has an additional 16 references. One of these references is the estimate of soil erosion in Central Belgium sourced from Richter (1983), where Richter (1983) is not the primary source but cites Bollinne (1982) in-text: "eight year measurements, carried out in central Belgium, showed soil losses of 10 to 25 tonnes per hectare per year (p. 11; Bollinne, 1982)". However, Bollinne (1982) did not calculate an average erosion rate for Central Belgium but calculated the erosion rates of 12 small experimental erosion plots in central Belgium. While the scaling of small plot-based studies to large spatial extents may be the only approach at a particular moment in time, it embeds substantial errors in the estimate due to the disconnect in space and time between plots and their broad areas of application. Boardman (1998) and Crosson et al. (1995) have a more detailed discussion on the perpetuation of the poorly sourced estimate of Pimentel et al. (1995).

Due to a paucity of data on soil erosion measurements and the frequent erroneous up-scaling of plot-based based studies in both space and time, modelling is required to gain an understanding of the extent of erosion at large spatial extents. For example, the most rigorous global application of the USLE estimates a global soil erosion rate of 2.8 t ha^{-1} yr^{-1} (Borrelli et al. 2017; all land uses), which is in stark contrast with the widely cited global erosion rate of 30 t ha^{-1} yr^{-1} estimated by Pimentel (2006; cropland and pastures). While the predictive accuracy of erosion models can be evaluated at the farm-field scale (Meinen and Robinson 2021), model evaluation is much more challenging at large spatial scales due to a lack of spatially-distributed

erosion data, and therefore models should be up-scaled in a rigorous manner that does not introduce significant uncertainty or error in their outcomes. Without proper model execution and rigorous analysis, we are in danger of discrediting our results, which can erode public trust and sustainability efforts.

While the USLE has the ideal characteristics of a large-scale model, i.e., a simple parsimonious modelling structure, our modelling results highlight the uncertainty implicit to up-scaling the USLE to the watershed scale. Our recommended modelling approach calculated an average erosion rate of 6.66 t ha^{-1} yr^{-1}. The outcome of using different design choices led to a range in model outcomes from 3.04 to 11.02 t ha^{-1} yr^{-1}; changing the implementation of all the USLE factors with a literature-based methodology led to a modelling outcome of 4.05 t ha^{-1} yr^{-1}; a comparison with literature showed a range in model outcomes from 0.72 t ha^{-1} yr^{-1} to 15.73 t ha^{-1} yr^{-1}. While the USLE is a simple empirical model, the variability in model outcomes demonstrates the challenges in up-scaling the USLE to a large spatial extent. A standardized and accredited methodology for up-scaling the USLE is needed to reduce uncertainty in modelling results. Our analysis provides a first step toward discussing this standardization by quantifying the impacts of different design choices on erosion estimates and when specific design choices should be made.

6.4.2. Challenges with using the USLE and Sediment Delivery Ratios

While we present a quantitative model outcome for coupling the USLE with a field-scale SDR, i.e., SDR_f, to predict soil loss from fields to waterways by defining a wide range of stochastic uncertainty in our Monte-Carlo simulation (i.e., -25 to -75% in-field deposition, ± 20% soil erosion rate, ± 20% filtering efficiency of riparian zones), the complexity of human-natural systems often precludes a quantitative interpretation of results. This complexity and the challenges of modelling sediment delivery in agricultural systems are best exemplified when looking at overland flow paths on satellite imagery. For example, in the upper-Nith Watershed, overland flow frequently routed to artificial drainage structures at field-edges, accompanied by large depositional plumes, and drained directly to the Nith River via surface inlets and subsurface tiles or to an adjacent field or ditch via a culvert. When we examined historical airborne imagery, we found that the majority of fields with visible signs of water erosion, that also had connectivity to the Nith River, were associated with artificial drainage issues from culvert and field tiles. Further complicating this, drainage patterns and flow connectivity changed considerably over a short-period of time due to new land management practices (e.g., Fig. 6.5). The implementation of a more complex environmental model in lieu of our SDR_f methodology will not provide more meaningful results unless field-scale features and their connectivity (e.g., location of drainage structures) are

empirically captured and their effects on overland flow explicitly modelled. Studies that couple the USLE with an SDR should generally be treated as qualitative due to the complexity of agricultural systems, the inability to validate model results, and since the application of an SDR is so far outside of the models intended design space.

Fig. 6.5. Example of land cover change that resulted in an artificial drainage issue. Flow drains from the northern field into a culvert under a roadway that, (a) in 2006 drained into a tree and grass cover filter strip before entering the Nith River, and (b) in 2019 drains over another agricultural field directly into the Nith River, forming a large ephemeral gully annually. Source: SWOOP 2015 imagery (left) and Google 2019, Maxar Technologies (right).

6.4.3. Conclusions

It is imperative that a standardized and accredited USLE setup is firmly established in the literature for model up-scaling that has results synonymous with Agricultural Handbook no. 537 (Wischmeier and Smith 1978) or Agricultural Handbook no. 703 (Renard et al. 1991) for revised USLE applications in a GIS. Cross-comparisons of USLE modelling results cannot be conducted without a standardized modelling approach. While we cannot provide guidelines for what constitutes an appropriate remote sensing dataset for estimating model input parameters or a methodology for up-scaling from the field to watershed scale, we provided a first step in this direction by demonstrating the impacts of different design choices and up-scaling methodologies on model outcomes. Pragmatism alone is not enough to justify a data source or modelling endeavour. The ideal model for large-scale environmental assessments of soil erosion will have a high intrinsic model error but low model input error; unfortunately, even with the simple parsimonious modelling structure of the USLE, poor results can be driven by model input error and user error. If the USLE continues to be used for large-scale environmental assessments of soil erosion, more rigor needs to be employed by model users to ensure that modelling results are not invalidated by poor design choices.

Chapter 7. Conclusions

Agricultural soil erosion continues to be an important area of environmental research. While there has been a large amount of scientific literature published in the last two decades on soil erosion, three key areas have been identified by Poesen (2018), among others, as being in need of further research: "(1) (an) improved understanding of both natural and anthropogenic soil erosion processes and their interactions, (2) scaling up soil erosion processes and rates in space and time, and (3) innovative techniques and strategies to prevent soil erosion or reduce erosion rates (Poesen, 2018)." The research presented in this dissertation was intended to meet these three key areas of research by fulfilling our five outlined research objectives.

7.1. Improving our understanding of soil erosion processes

Accurate and repeatable measurements of surface change are needed to better understand natural and anthropogenic soil erosion processes and their interactions. The majority of soil erosion research focusses on studying sheet and rill erosion processes at the plot scale (< 0.1 ha), ignoring anthropogenic process domains (e.g., tillage erosion) and other natural large-scale process domains (e.g., gully erosion). While the focus on plot-scale erosion processes is pragmatic for model development (e.g., 10,000 plot years of measurements; USLE, Wischmeier and Smith, 1978), it is important that measurements of soil erosion processes capture all process domains that contribute to soil movement at the field scale to better understand soil degradation from erosion processes. Capturing field-scale soil movement requires new measurement techniques and workflows.

In this dissertation, by meeting Research Objective 1 and 2, we provided a novel framework for using the UAV SfM-MVS workflow to model surface change-detection (i.e., erosion and deposition) in agricultural systems over the course of one year. As part of our experiential investigation into the accuracy of the SfM-MVS workflow, we identified the effects of UAV image orientation on the accuracy of camera self-calibration and the resultant SfM-MVS pointcloud by testing four different UAV image acquisition schemes that incorporated both nadir and oblique imagery of an agricultural field. The coupling of nadir and oblique imaging angles led to the highest surface model accuracy in the absence of ground control points (vertical RMSE: 0.047 m, horizontal RMSE: 0.019 m), while with a normative distribution of GCPs the nadir-only image sets had similar accuracy metrics (vertical RMSE 0.028 m, horizontal RMSE 0.017 m) to surface models generated with nadir and oblique imaging angles ([NC_{26}] vertical RMSE 0.028 m, horizontal RMSE 0.013 m). Homologous keypoint matching between nadir and oblique imagery was poor when the survey conditions were bright and the surface texture of the field was

homogeneous, leading to broad-scale vertical noise in the generated surface models. In agricultural systems, a nadir-only imaging scheme is recommended due to the low amount of image content (e.g., soil) and vegetated surfaces (e.g., rows of corn), and the comparable results between nadir and oblique imaging angles when a sufficiently dense deployment of GCPs was used. When we employed the UAV SfM-MVS workflow with nadir-only imagery in Chapters 2 and 3, we reported vertical checkpoint errors (i.e., RMSE) in our pointclouds of 0.021 – 0.039 m. Given a standard nadir UAV image acquisition, an RTK-GNSS ground control survey, and the use of a self-calibrating bundle adjustment in an SfM-MVS software application, we expect the vertical accuracy (RMSE) of pointclouds to be 2–3× the GSD with a practical upper limit of 0.01 m; the vertical accuracy will converge on 2× the GSD if the ground control network is sufficiently dense.

Based on these accuracy metrics, we recommend following our workflow from April 25, 2019, to recreate the topography of an agricultural field to quantify the development of erosion processes: a nadir image acquisition scheme, UAV height of 60 m AGL, 0.011 m GSD, 70% image overlap, 3 GCPs per hectare (expected vertical RMSE: 0.021 m). While small-scale process domains cannot be directly measured with this workflow, since we identified a threshold for topographic change at > 0.04 m in depth, we demonstrated in Chapter 4 that down-slope depositional zones can be used as a proxy for small-scale (i.e., sheet and rill) upslope erosion processes. This provides a comprehensive field-scale evaluation of erosion processes.

To improve upon our recommended workflow, it should be possible to directly measure sheet and rill erosion by using stable GCPs, i.e., permanently fixed throughout an entire study. The accuracy of our ground control survey constrained the maximum vertical accuracy of each surface model to the accuracy of the surveying technique (i.e., a maximum achievable vertical accuracy of 0.01 m with RTK-GNSS); sub-cm accuracies can only be achieved if the reference system is stable. Stable GCPs allow for both a precise co-registration of surface models and remove RTK-GNSS accuracy constraints. The GSD must also be commensurate with the accuracy desired, i.e., the GSD of the aerial survey will need to be increased to reach sub-cm accuracies. It is important to note that as the GSD increases, the field-of-view of the camera is constrained to a smaller area and a larger number of GCPs are required to avoid adverse surface deformation. Future research should be directed at refining the UAV SfM-MVS workflow for measuring sub-cm erosion processes following our recommendations of using a higher GSD, fixed GCPs, or exploring the application of RTK-GNSS enabled UAVs. Once an accredited workflow is established, future research can be directed towards long-term soil erosion monitoring

at the farm-field scale and quantifying the relative impacts of different natural and anthropogenic erosion processes.

7.2. Scaling up soil erosion processes in space and time: The necessity of field-scale studies

An important avenue of future agricultural research is differentiating between soil erosion and soil loss, and how landscape connectivity affects soil movement. High rates of water erosion in a disconnected system have a lower environmental impact that low rates of water erosion in a well-connected system. Since most erosion studies are limited by their size, i.e., constrained to experimental research plots, it can be difficult to scale up the results in both space and time to represent landscape connectivity and large-scale process domains. A key challenge in soil erosion studies is understanding the movement of soils from farm fields to waterways, the transport of eroded agricultural sediments in waterways, and the sediment yield at the outlet of a waterway. Poesen (2018) identifies that the accurate prediction of sediment yield is a major research need and “one of the main challenges in geomorphological research”. In order to better understand soil erosion and soil movement in agricultural systems, research needs to be conducted at the correct temporal and spatial timescale, i.e., on a storm-by-storm basis at the farm field scale.

In this dissertation, we used a UAV SfM-MVS workflow to model the topography of an agricultural farm field and monitor field-scale erosion processes over the course of one year. This novel workflow allowed us to directly quantify the seasonal distribution of soil erosion processes across an entire farm field, rather than trying to up-scale a plot-based study to the field scale. In conjunction with our field-scale erosion measurements, we used our surface models of the farm field as topographic inputs for a simple hydrology model to give us further insights into the hydrology and connectivity of our agricultural system. While the moldboard plow is usually associated with accelerated rates of soil erosion, our hillslope-scale hydrology simulations showcased that the moldboard plow hydrologically disconnected large areas of each hillslope, resulting in higher rates of surface ponding and a decrease in surface runoff relative to a cultivated surface. Conditions were more favorable for surface runoff and soil loss immediately following cultivation. This could explain the surprising temporal distribution of our erosion measurements; 86% of the total soil movement from upslope areas to catch basins occurred between May 17, 2018, and September 19, 2018, with the majority of water erosion happening from spring storm immediately following cultivation. While the field surface was barren over the winter fields following a moldboard plow, very little soil erosion occurred through the winter months. The rough

microtopography created with the moldboard plow played an important role in restricting the flow of surface runoff and subsequent soil movement. The complex interactions between microtopography and surface runoff were not visible at the plot scale, but only became evident at the hillslope scale.

An improved understanding of the interactions between land management practices and landscape connectivity is an important area of research for future soil erosion studies, since modelling the links in the landscape between systems is just as important as understanding absolute soil erosion rates. Since plot-based studies cannot model landscape connectivity, it is important that watershed-scale models be empirically informed from field-scale studies to better understand soil movement between systems. We demonstrated an approach for measuring field-scale erosion processes in Research Objective 1 – 3, demonstrated an approach for modelling landscape connectivity using very-high resolution DEMs in Objective 4, and we provided a workflow for estimating soil loss and modelling landscape connectivity by coupling the USLE with a field-scale SDR in Objective 5. The starting point of agricultural soil erosion studies needs to be at the scale of the agricultural decision maker, i.e., the individual farm field. This approach allows for an accurate representation of the connectivity of each agricultural system and facilitates a proper representation of the human dimension (i.e., cropping and management practices) in erosion estimates.

7.3. Strategies to prevent soil erosion or reduce erosion rates: Modelling

Modelling is often used to evaluate the implementation of new best management practices that can ameliorate high rates of soil erosion, but models must be evaluated to ensure they are behavioral for a proper evaluation of new best management practices. In this dissertation, we evaluated soil erosion estimates from the USLE and WEPP to fulfill Research Objective 3. The depositional plume in each of the six catch basins on our study site was used as a proxy for the upslope erosion rate of each basin. Our field-scale measurements showcased that the installation of catch basins were able to stop 159.52 t of sediment from entering the waterway adjacent to the study site over the course of one year, corresponding to an erosion rate of 18.83 t ha^{-1} yr^{-1} across the six measured basins. Modelling predictions of soil erosion rates were 26.23 t ha^{-1} yr^{-1} and 16.41 t ha^{-1} yr^{-1} for the USLE and WEPP, respectively. The WEPP was specifically designed to replace the USLE by improving short-term soil loss estimates by a process-based representation of climate and hydrology; our study corroborated that the WEPP outperforms the USLE at shorter timescales at the farm-field scale, most notably for sub-annual predictions. Both annual and sub-

annual erosion rates modelled with WEPP were within the upper limit of predictive accuracy, while the USLE tended to systematically overestimate soil erosion rates.

The accurate predictions of the WEPP, when validated with our field-scale measurements, allowed us to simulate long-term management practices across our study site which provided insights into the temporal distribution of erosion processes and the efficacy of new best management practices. Most notably, the WEPP estimated a 10-year average erosion rate for the full 15.9-ha study site at 8.12 t ha^{-1} yr^{-1} when using a fall moldboard plow, and a reduction in soil erosion rates for two different types of chisel plows: 4.65 t ha^{-1} yr^{-1} (chisel plow with coulters and shovels) and 2.91 t ha^{-1} yr^{-1} (chisel plow with coulters and sweeps). Modelling results showcased that the majority of soil erosion occurred during the early growing season on our study site, with an average of 6.4 days per year with soil erosion; winter events and snowmelt constituted 70% of the average long-term runoff with 14.1 days per year with runoff, but winter runoff events were rarely associated with soil loss. These modelling outcomes were consistent with our in-situ observations and field measurements.

Future research on the implementation of best management practices in agricultural systems that use a modelling approach should start with a model evaluation or validation. Our presented UAV SfM-MVS workflow can be used to provide detailed temporally-distributed data for model evaluations. While not presented in this thesis, the UAV SfM-MVS workflow can also provide a number of additional outputs that are useful for agricultural soil erosion research and model evaluation. We used our pointclouds for mapping crop heights (± 0.15 m accuracy on mature corn), qualitatively mapping erosion features (e.g., sheet, rill, ephemeral gully erosion), soil mapping (e.g., desiccated clays, sand), field management mapping (e.g., sub-surface tile drainage lines, surface inlets, soil berms), and crop health (e.g., NDVI). These additional datasets can be explored as additional points of a priori or qualitative model validation in future UAV-based research.

8. Bibliography

Abaci, O., & Papanicolaou, A. T. (2009). Long-term effects of management practices on water-driven soil erosion in an intense agricultural sub-watershed: Monitoring and modelling. *Hydrological Processes: An International Journal*, *23*(19), 2818-2837. Doi: 10.1002/hyp.7380

Abedini, M. J., Dickinson, W. T., & Rudra, R. P. (2006). On depressional storages: The effect of DEM spatial resolution. *Journal of Hydrology*, 318(1-4), 138-150. Doi: 10.1016/j.jhydrol.2005.06.010

Agricorp (2018). 2018 Corn Yields. https://www.agricorp.com/en-ca/News/2019/Pages/PI-MapShows2018CornYields.aspx

Agüera-Vega, F., Carvajal-Ramírez, F., & Martínez-Carricondo, P. (2017). Assessment of photogrammetric mapping accuracy based on variation ground control points number using unmanned aerial vehicle. *Measurement*, *98*, 221-227. Doi: 10.1016/j.measurement.2016.12.002

Alewell, C., Borrelli, P., Meusburger, K., & Panagos, P. (2019). Using the USLE: Chances, challenges and limitations of soil erosion modelling. *International soil and water conservation research*, *7*(3), 203-225. Doi: 10.1016/j.iswcr.2019.05.004

Amore, E., Modica, C., Nearing, M. A., & Santoro, V. C. (2004). Scale effect in USLE and WEPP application for soil erosion computation from three Sicilian basins. *Journal of Hydrology*, *293*(1-4), 100-114. Doi: 10.1016/j.jhydrol.2004.01.018

Appels, Willemijn M., Patrick W. Bogaart, and Sjoerd EATM van der Zee. "Influence of spatial variations of microtopography and infiltration on surface runoff and field scale hydrological connectivity." *Advances in Water Resources 34.2* (2011): 303-313. Doi: 10.1016/j.advwatres.2010.12.003

Arnold, J. (1994). SWAT-soil and water assessment tool.

Arnold, J. G., Srinivasan, R., Muttiah, R. S., & Williams, J. R. (1998). Large area hydrologic modeling and assessment part I: model development 1. *JAWRA Journal of the American Water Resources Association, 34*(1), 73-89. Doi: 10.1111/j.1752-1688.1998.tb05961.x

Barber, R. G. (1983). The magnitude and sources of soil erosion in some humid and semi-arid parts of Kenya and the significance of soil loss tolerance values in soil conservation in

Kenya. In *Soil and water conservation in Kenya. In: Proceedings of the Second National Workshop, Institute for Development Studies, University of Nairobi, Kenya*.

Barrow, C. J. (1991). *Land degradation: development and breakdown of terrestrial environments*. Cambridge University Press.

Bash, E. A., Moorman, B. J., & Gunther, A. (2018). Detecting short-term surface melt on an arctic glacier using uav surveys. *Remote Sensing*, *10*(10), 1547. Doi: 10.3390/rs10101547

Batista, P. V., Davies, J., Silva, M. L., & Quinton, J. N. (2019). On the evaluation of soil erosion models: Are we doing enough?. *Earth-Science Reviews*, *197*, 102898. Doi: 10.1016/j.earscirev.2019.102898

Beasley, D. B., Huggins, L. F., & Monke, A. (1980). ANSWERS: A model for watershed planning. *Transactions of the ASAE*, *23*(4), 938-0944. Doi: 10.13031/2013.34692

Belasri, A., & Lakhouili, A. (2016). Estimation of soil erosion risk using the Universal Soil Loss Equation (USLE) and geo-information technology in Oued El Makhazine watershed, Morocco. *Journal of Geographic Information System*, *8*(01), 98. Doi: 10.4236/jgis.2016.81010

Bennett, E. M., Carpenter, S. R., & Caraco, N. F. (2001). Human impact on erodable phosphorus and eutrophication: a global perspective: increasing accumulation of phosphorus in soil threatens rivers, lakes, and coastal oceans with eutrophication. *BioScience*, *51*(3), 227-234. Doi: 10.1641/0006-3568(2001)051[0227:HIOEPA]2.0.CO;2

Betrie, G. D., Mohamed, Y. A., Griensven, A. V., & Srinivasan, R. (2011). Sediment management modelling in the Blue Nile Basin using SWAT model. *Hydrology and Earth System Sciences*, *15*(3), 807-818. Doi: 10.5194/hess-15-807-2011

Beven, K. (2006). A manifesto for the equifinality thesis. *Journal of hydrology, 320*(1-2), 18-36. Doi: 10.1016/j.jhydrol.2005.07.007

Bicknell, B. R., Donigian Jr, A. S., & Barnwell, T. A. (1985). Modeling water quality and the effects of agricultural best management practices in the Iowa River Basin. *Water Science and Technology*, *17*(6-7), 1141-1153. Doi: 10.2166/wst.1985.0209

Bigelow, D., Claassen, R., Hellerstein, D., Breneman, V., Williams, R., & You, C. (2020). *The Fate of Land in Expiring Conservation Reserve Program Contracts, 2013-16* (No. 1476-2020-047).

Boardman, J. (1998). An average soil erosion rate for Europe: myth or reality?. *Journal of Soil and Water Conservation*, *53*(1), 46-50.

Boardman, J. (2006). Soil erosion science: Reflections on the limitations of current approaches. *Catena*, *68*(2-3), 73-86. Doi: 10.1016/j.catena.2006.03.007

Boardman, J., Vandaele, K., Evans, R., & Foster, I. D. (2019). Off-site impacts of soil erosion and runoff: Why connectivity is more important than erosion rates. *Soil Use and Management*, *35*(2), 245-256. Doi: 10.1111/sum.12496

Bollinne, A. (1982). *Etude et prévision de l'érosion des sols limoneux cultivés en moyenne Belgique* (Doctoral dissertation, Université de Liège).

Borrelli, P., Märker, M., Panagos, P., & Schütt, B. (2014). Modeling soil erosion and river sediment yield for an intermountain drainage basin of the Central Apennines, Italy. *Catena*, *114*, 45-58. Doi: 10.1016/j.catena.2013.10.007

Borrelli, P., Robinson, D. A., Fleischer, L. R., Lugato, E., Ballabio, C., Alewell, C., ... & Bagarello, V. (2017). An assessment of the global impact of 21st century land use change on soil erosion. *Nature communications*, *8*(1), 1-13. Doi: 10.1038/s41467-017-02142-7

Bracmort, K. S., Arabi, M., Frankenberger, J. R., Engel, B. A., & Arnold, J. G. (2006). Modeling long-term water quality impact of structural BMPs. *Transactions of the ASABE*, *49*(2), 367-374. Doi: 10.13031/2013.20411

Branton, C., & Robinson, D. T. (2020). Quantifying topographic characteristics of wetlandscapes. *Wetlands*, *40*(2), 433-449. Doi: 10.1007/s13157-019-01187-2

Briak, H., Mrabet, R., Moussadek, R., & Aboumaria, K. (2019). Use of a calibrated SWAT model to evaluate the effects of agricultural BMPs on sediments of the Kalaya river basin (North of Morocco). *International Soil and Water Conservation Research*, *7*(2), 176-183. Doi: 10.1016/j.iswcr.2019.02.002

Buhler, D. D. (1992). Population dynamics and control of annual weeds in corn (Zea mays) as influenced by tillage systems. *Weed Science*, 241-248.

Busari, M. A., Kukal, S. S., Kaur, A., Bhatt, R., & Dulazi, A. A. (2015). Conservation tillage impacts on soil, crop and the environment. *International Soil and Water Conservation Research*, 3(2), 119-129. Doi: 10.1016/j.iswcr.2015.05.002

Carrivick, J. L., Smith, M. W., & Quincey, D. J. (2016). *Structure from Motion in the Geosciences*. John Wiley & Sons.

Clearwater, R. L., T. Martin and T. Hoppe (eds.) 2016. Environmental sustainability of Canadian agriculture: Agri-environmental indicator report series – Report #4. Ottawa, ON: Agriculture and Agri-Food Canada.

Cook, K. L. (2017). An evaluation of the effectiveness of low-cost UAVs and structure from motion for geomorphic change detection. *Geomorphology*, *278*, 195-208. Doi: 10.1016/j.geomorph.2016.11.009

Cooke, S., (2006). Water quality in the Grand River: A summary of current conditions (2000-2004) and long term trends. https://www.grandriver.ca/en/our-watershed/resources/Documents/Water_Quality_Conditions_2006.pdf

Crosson, P., Pimentel, D., Harvey, C., Resosudarno, P., Sinclair, K., Kurz, D., ... & Blair, R. (1995). Soil erosion estimates and costs. *Science*, *269*(5223), 461-466.

Dabral, P. P., Baithuri, N., & Pandey, A. (2008). Soil erosion assessment in a hilly catchment of North Eastern India using USLE, GIS and remote sensing. *Water Resources Management*, *22*(12), 1783-1798. Doi: 10.1007/s11269-008-9253-9

Daniel, T. C., Sharpley, A. N., & Lemunyon, J. L. (1998). Agricultural phosphorus and eutrophication: A symposium overview. *Journal of environmental quality*, *27*(2), 251-257. Doi: 10.2134/jeq1998.00472425002700020002x

d'Amour, C. B., Reitsma, F., Baiocchi, G., Barthel, S., Güneralp, B., Erb, K. H., ... & Seto, K. C. (2017). Future urban land expansion and implications for global croplands. *Proceedings of the National Academy of Sciences*, *114*(34), 8939-8944. Doi: 10.1073/pnas.1606036114

d'Oleire-Oltmanns, S., Marzolff, I., Peter, K. D., & Ries, J. B. (2012). Unmanned aerial vehicle (UAV) for monitoring soil erosion in Morocco. *Remote Sensing*, *4*(11), 3390-3416. Doi: 10.3390/rs4113390

De Roo, A. P. J., Wesseling, C. G., & Ritsema, C. J. (1996). LISEM: a single-event physically based hydrological and soil erosion model for drainage basins. I: theory, input and output. *Hydrological processes*, *10*(8), 1107-1117. Doi: 10.1002/(SICI)1099-1085(199608)10:8<1107::AID-HYP415>3.0.CO;2-4.

Den Biggelaar, C., Lal, R., Wiebe, K., & Breneman, V. (2001). Impact of soil erosion on crop yields in North America. Doi: 10.1016/S0065-2113(01)72010-X

Derpsch, R., Friedrich, T., Kassam, A., & Li, H. (2010). Current status of adoption of no-till farming in the world and some of its main benefits. *International Journal of Agricultural and Biological Engineering*, *3*(1), 1-25. Doi: 10.3965/j.issn.1934-6344.2010.01.0-0

Desmet, P. J. J., & Govers, G. (1996). A GIS procedure for automatically calculating the USLE LS factor on topographically complex landscape units. *Journal of soil and water conservation*, *51*(5), 427-433.

Desprats, J. F., Raclot, D., Rousseau, M., Cerdan, O., Garcin, M. L. B. Y., Le Bissonnais, Y., ... & Monfort-Climent, D. (2013). Mapping linear erosion features using high and very high resolution satellite imagery. *Land Degradation & Development*, *24*(1), 22-32. Doi: 10.1002/ldr.1094

Devatha, C. P., Deshpande, V., & Renukaprasad, M. S. (2015). Estimation of soil loss using USLE model for Kulhan Watershed, Chattisgarh-A case study. *Aquatic Procedia*, *4*, 1429-1436. Doi: 10.1016/j.aqpro.2015.02.185

Dunne, T., Zhang, W., & Aubry, B. F. (1991). Effects of rainfall, vegetation, and microtopography on infiltration and runoff. *Water Resources Research*, *27*(9), 2271-2285. Doi: 10.1029/91WR01585

Eltner, A., Mulsow, C., & Maas, H. G. (2013). Quantitative measurement of soil erosion from TLS and UAV data. *Int. Arch. Photogramm. Remote Sens. Spat. Inf. Sci*, *40*, 4-6. Doi: 10.5194/isprsarchives-XL-1-W2-119-2013

Eltner, A., Baumgart, P., Maas, H. G., & Faust, D. (2015). Multi-temporal UAV data for automatic measurement of rill and interrill erosion on loess soil. *Earth Surface Processes and Landforms*, *40*(6), 741-755. Doi: 10.1002/esp.3673

ELD Initiative, (2015). The value of land: Prosperous lands and positive rewards through sustainable land management. www.eld-initiative.org.

Eltner, A., Mulsow, C., & Maas, H. G. (2013). Quantitative measurement of soil erosion from TLS and UAV data. *Int. Arch. Photogramm. Remote Sens. Spat. Inf. Sci, 40*, 4-6. Doi: 10.5194/isprsarchives-XL-1-W2-119-2013y

Eltner, A., Kaiser, A., Castillo, C., Rock, G., Neugirg, F., & Abellán, A. (2016). Image-based surface reconstruction in geomorphometry–merits, limits and developments. *Earth Surface Dynamics*, *4*(2), 359-389. Doi: 10.5194/esurf-4-359-2016

Environment Canada. (2004). Canadian guidance framework for the management of phosphorus in freshwater systems. Ecosystem Health: Science-based solutions report no. 1–8. Cat. No. En1–34/8–2004E.

Erdogan, E. H., Erpul, G., & Bayramin, İ. (2007). Use of USLE/GIS methodology for predicting soil loss in a semiarid agricultural watershed. *Environmental monitoring and assessment*, *131*(1-3), 153-161. Doi: 10.1007/s10661-006-9464-6

Evans, R., & Brazier, R. (2005). Evaluation of modelled spatially distributed predictions of soil erosion by water versus field-based assessments. *Environmental Science & Policy*, *8*(5), 493-501. Doi: 10.1016/j.envsci.2005.04.009

Evans, R. (2013). Assessment and monitoring of accelerated water erosion of cultivated land–when will reality be acknowledged?. *Soil use and management*, *29*(1), 105-118. Doi: 10.1111/sum.12010

FAO, I. (2015). Status of the world's soil resources (SWSR)–main report. *Food and agriculture organization of the United Nations and intergovernmental technical panel on soils,* Rome, Italy, 650.

Favis-Mortlock, D. (1998). Validation of field-scale soil erosion models using common datasets. In Modelling soil erosion by water (pp. 89-127). Springer, Berlin, Heidelberg. Doi: 10.1007/978-3-642-58913-3_9.

Favis-Mortlock, D., Boardman, J., & MacMillan, V. (2001). The limits of erosion modeling. In *Landscape erosion and evolution modeling* (pp. 477-516). Springer, Boston, MA. Doi: 10.1007/978-1-4615-0575-4_16

Ferro, V., & Porto, P. (2000). Sediment delivery distributed (SEDD) model. *Journal of hydrologic engineering*, *5*(4), 411-422.

Fischer, F. K., Kistler, M., Brandhuber, R., Maier, H., Treisch, M., & Auerswald, K. (2018). Validation of official erosion modelling based on high-resolution radar rain data by aerial photo erosion classification. *Earth Surface Processes and Landforms*, *43*(1), 187-194. Doi: 10.1002/esp.4216

Fisette, T., Rollin, P., Aly, Z., Campbell, L., Daneshfar, B., Filyer, P., ... & Jarvis, I. (2013, August). AAFC annual crop inventory. In 2013 Second International Conference on Agro-Geoinformatics (Agro-Geoinformatics) (pp. 270-274). IEEE.

Fistikoglu, O., & Harmancioglu, N. B. (2002). Integration of GIS with USLE in assessment of soil erosion. *Water Resources Management*, *16*(6), 447-467. Doi: 10.1023/A:1022282125760

Flanagan, D. C., & Nearing, M. A. (1995). USDA-Water Erosion Prediction Project: Hillslope profile and watershed model documentation. *Nserl Rep*, *10*, 1-123.

Flanagan, D. C., Ascough, J. C., Nearing, M. A., & Laflen, J. M. (2001). The water erosion prediction project (WEPP) model. In *Landscape erosion and evolution modeling* (pp. 145-199). Springer, Boston, MA. Doi: 10.1007/978-1-4615-0575-4_7

Foley, J. A. (2011). Can we feed the world sustain the planet?. *Scientific American*, *305*(5), 60-65.

Foley, J. A., Ramankutty, N., Brauman, K. A., Cassidy, E. S., Gerber, J. S., Johnston, M., ... & Zaks, D. P. (2011). Solutions for a cultivated planet. *Nature*, *478*(7369), 337-342. Doi: 10.1038/nature10452

Frei, S., & Fleckenstein, J. H. (2014). Representing effects of micro-topography on runoff generation and sub-surface flow patterns by using superficial rill/depression storage height variations. Environmental modelling & software, 52, 5-18. Doi: 10.1016/j.envsoft.2013.10.007

Fryirs, K. A., Brierley, G. J., Preston, N. J., & Kasai, M. (2007). Buffers, barriers and blankets: the (dis) connectivity of catchment-scale sediment cascades. *Catena*, *70*(1), 49-67. Doi: 10.1016/j.catena.2006.07.007

Fournier, F. (1967). Research on soil erosion and soil conservation in Africa. *African Soils*, *12*(1), 53-96.

Gilley, J. E., Kottwitz, E. R., & Simanton, J. R. (1990). Hydraulic characteristics of rills. *Transactions of the ASAE*, *33*(6), 1900-1906. Doi: 10.13031/2013.31556

Gonçalves, J. A., & Henriques, R. (2015). UAV photogrammetry for topographic monitoring of coastal areas. *ISPRS Journal of Photogrammetry and Remote Sensing*, *104*, 101-111. Doi: 10.1016/j.isprsjprs.2015.02.009

Graves, A. R., Morris, J., Deeks, L. K., Rickson, R. J., Kibblewhite, M. G., Harris, J. A., ... & Truckle, I. (2015). The total costs of soil degradation in England and Wales. *Ecological Economics, 119,* 399-413. Doi: 10.1016/j.ecolecon.2015.07.026

Green, W. H., & Ampt, G. A. (1911). Studies on Soil Phyics. *The Journal of Agricultural Science, 4*(1), 1-24.

Griffin, M. L., Beasley, D. B., Fletcher, J. J., & Foster, G. R. (1988). Estimating soil loss on topographically non-uniform field and farm units. Journal of Soil and Water Conservation, 43(4), 326-331.

Grimm, M., Jones, R. J., Rusco, E., & Montanarella, L. (2003). Soil erosion risk in Italy: a revised USLE approach. *European Soil Bureau Research Report*, *11*, 23.

Groisman, P. Y., Knight, R. W., Easterling, D. R., Karl, T. R., Hegerl, G. C., & Razuvaev, V. N. (2005). Trends in intense precipitation in the climate record. *Journal of climate, 18*(9), 1326-1350. Doi: 10.1175/JCLI3339.1

Harder, P., Schirmer, M., Pomeroy, J., & Helgason, W. (2016). Accuracy of snow depth estimation in mountain and prairie environments by an unmanned aerial vehicle. *The Cryosphere*, *10*(6), 2559-2571. Doi: 10.5194/tc-10-2559-2016

Harwin, S., Lucieer, A., & Osborn, J. (2015). The impact of the calibration method on the accuracy of point clouds derived using unmanned aerial vehicle multi-view stereopsis. *Remote Sensing*, *7*(9), 11933-11953. Doi: 10.3390/rs70911933

Henley, W. F., Patterson, M. A., Neves, R. J., & Lemly, A. D. (2000). Effects of sedimentation and turbidity on lotic food webs: a concise review for natural resource managers. *Reviews in Fisheries Science, 8*(2), 125-139. Doi: 10.1080/10641260091129198

Holeton, C. (2013). Sources of Nutrients and Sediments in the Grand River Watershed. Grand River Watershed Water Management Plan, 73.

Holmes, T. P. (1988). The offsite impact of soil erosion on the water treatment industry. *Land Economics, 64(*4), 356-366. Doi: 10.2307/3146308

Huang, M., Gallichand, J., Wang, Z., & Goulet, M. (2006). A modification to the Soil Conservation Service curve number method for steep slopes in the Loess Plateau of China. Hydrological Processes: An International Journal, 20(3), 579-589. Doi: 10.1002/hyp.5925

Hui, L., Xiaoling, C., Lim, K. J., Xiaobin, C., & Sagong, M. (2010). Assessment of soil erosion and sediment yield in Liao watershed, Jiangxi Province, China, Using USLE, GIS, and RS. *Journal of Earth Science*, *21*(6), 941-953. Doi: 10.1007/s12583-010-0147-4

Humphreys, G. S. (1984). *The environment and soils of Chimbu Province, Papua New Guinea, with particular reference to soil erosion* (No. 35). Research Bulletin No. 35, Department of Primary Industry.

Immerzeel, W. W., Kraaijenbrink, P. D., Shea, J. M., Shrestha, A. B., Pellicciotti, F., Bierkens, M. F., & de Jong, S. M. (2014). High-resolution monitoring of Himalayan glacier dynamics using unmanned aerial vehicles. *Remote Sensing of Environment*, *150*, 93-103. Doi: 10.1016/j.rse.2014.04.025

James, M. R., & Robson, S. (2012). Straightforward reconstruction of 3D surfaces and topography with a camera: Accuracy and geoscience application. *Journal of Geophysical Research: Earth Surface*, *117*(F3). Doi: 10.1029/2011JF002289

James, M. R., & Robson, S. (2014). Mitigating systematic error in topographic models derived from UAV and ground-based image networks. *Earth Surface Processes and Landforms*, *39*(10), 1413-1420. Doi: 10.1002/esp.3609

James, M. R., Robson, S., d'Oleire-Oltmanns, S., & Niethammer, U. (2017). Optimising UAV topographic surveys processed with structure-from-motion: Ground control quality, quantity and bundle adjustment. *Geomorphology*, *280*, 51-66. Doi: 10.1016/j.geomorph.2016.11.021

Jenson, S. K., & Domingue, J. O. (1988). Extracting topographic structure from digital elevation data for geographic information system analysis. *Photogrammetric engineering and remote sensing*, *54*(11), 1593-1600.

Jetten, V., De Roo, A. D., & Favis-Mortlock, D. (1999). Evaluation of field-scale and catchment-scale soil erosion models. *Catena*, *37*(3-4), 521-541. Doi: 10.1016/S0341-8162(99)00037-5

Jetten, V., Govers, G., & Hessel, R. (2003). Erosion models: quality of spatial predictions. *Hydrological processes*, *17*(5), 887-900. Doi: 10.1002/hyp.1168

Kaiser, A., Neugirg, F., Rock, G., Müller, C., Haas, F., Ries, J., & Schmidt, J. (2014). Small-scale surface reconstruction and volume calculation of soil erosion in complex Moroccan gully

morphology using structure from motion. *Remote Sensing*, *6*(8), 7050-7080. Doi: 10.3390/rs6087050

Kamphorst, E. C., Jetten, V., Guerif, J., Pitk a¨ nen, J., Iversen, B. V., Douglas, J. T., & Paz, A. (2000). Predicting depressional storage from soil surface roughness. *Soil Science Society of America Journal, 64*(5), 1749-1758. Doi: 10.2136/sssaj2000.6451749x

Kaspar, T. C., Radke, J. K., & Laflen, J. M. (2001). Small grain cover crops and wheel traffic effects on infiltration, runoff, and erosion. *Journal of Soil and Water Conservation*, *56*(2), 160-164.

Keay-Bright, J., & Boardman, J. (2009). Evidence from field-based studies of rates of soil erosion on degraded land in the central Karoo, South Africa. *Geomorphology*, *103*(3), 455-465. Doi: 10.1016/j.geomorph.2008.07.011

King, K. W., Williams, M. R., Macrae, M. L., Fausey, N. R., Frankenberger, J., Smith, D. R., ... & Brown, L. C. (2015). Phosphorus transport in agricultural subsurface drainage: A review. *Journal of environmental quality*, *44*(2), 467-485. Doi: 10.2134/jeq2014.04.0163

Knisel, W. G. (1980). *CREAMS: A field scale model for chemicals, runoff, and erosion from agricultural management systems* (No. 26). Department of Agriculture, Science and Education Administration.

Kronvang, B., Andersen, H. E., Larsen, S. E., & Audet, J. (2013). Importance of bank erosion for sediment input, storage and export at the catchment scale. *Journal of Soils and Sediments*, *13*(1), 230-241. Doi: 10.1007/s11368-012-0597-7

Laflen, J. M., Lane, L. J., & Foster, G. R. (1991). WEPP: A new generation of erosion prediction technology. *Journal of Soil and Water Conservation*, *46*(1), 34-38.

Laflen, J. M., Flanagan, D. C., & Engel, B. A. (2004). SOIL EROSION AND SEDIMENT YIELD PREDICTION ACCURACY USING WEPP 1. *JAWRA Journal of the American Water Resources Association*, *40*(2), 289-297. Doi: 10.1111/j.1752-1688.2004.tb01029.x

Lague, D., Brodu, N., & Leroux, J. (2013). Accurate 3D comparison of complex topography with terrestrial laser scanner: Application to the Rangitikei canyon (NZ). *ISPRS journal of photogrammetry and remote sensing*, *82*, 10-26. Doi: 10.1016/j.isprsjprs.2013.04.009

Lal, R. (1976a). Soil erosion problems on an alfisol in western Nigeria and their control: IITA monograph No. 1.

Lal, R. (1976b). Soil erosion on Alfisols in Western Nigeria. *Geoderma*, *16*(5), 363 – 431. Doi: 10.1016/0016-7061(76)90001-X

Lal, R., Hall, G. F., & Miller, F. P. (1989). Soil degradation: I. Basic processes. *Land Degradation & Development*, *1*(1), 51-69. Doi: 10.1002/ldr.3400010106

Lal, R. (1991). Tillage and agricultural sustainability. *Soil and Tillage Research*, *20*(2-4), 133-146. Doi: 10.1016/0167-1987(91)90036-W

Lal, R., Reicosky, D. C., & Hanson, J. D. (2007). Evolution of the plow over 10,000 years and the rationale for no-till farming. Doi: 10.1016/j.still.2006.11.004

Laflen, J. M., Lane, L. J., & Foster, G. R. (1991). WEPP: A new generation of erosion prediction technology. *Journal of Soil and Water Conservation*, *46*(1), 34-38.

Lane, S. N., Westaway, R. M., & Murray Hicks, D. (2003). Estimation of erosion and deposition volumes in a large, gravel-bed, braided river using synoptic remote sensing. *Earth Surface Processes and Landforms: The Journal of the British Geomorphological Research Group*, *28*(3), 249-271. Doi: 10.1002/esp.483

Lobb, D. A., Kachanoski, R. G., & Miller, M. H. (1995). Tillage translocation and tillage erosion on shoulder slope landscape positions measured using 137Cs as a tracer. *Canadian Journal of Soil Science*, *75*(2), 211-218. Doi: 10.4141/cjss95-029

Loomer, H., Cooke, S. (2011). Water Quality in the Grand River Watershed: Current Conditions & Trends. https://www.sourcewater.ca/en/source-protection-areas/resources/Documents/Grand/Grand_Reports_WaterQuality_2011.pdf

Lowe, D. G. (2004). Distinctive image features from scale-invariant keypoints. *International journal of computer vision*, *60*(2), 91-110. Doi: 10.1023/B:VISI.0000029664.99615.94

Lucieer, A., Jong, S. M. D., & Turner, D. (2014a). Mapping landslide displacements using Structure from Motion (SfM) and image correlation of multi-temporal UAV photography. *Progress in Physical Geography*, *38*(1), 97-116. Doi: 10.1177/0309133313515293

Lucieer, A., Turner, D., King, D. H., & Robinson, S. A. (2014b). Using an Unmanned Aerial Vehicle (UAV) to capture micro-topography of Antarctic moss beds. *International journal of applied earth observation and geoinformation*, *27*, 53-62. Doi: 10.1016/j.jag.2013.05.011

Macrae, M. L., English, M. C., Schiff, S. L., & Stone, M. (2007a). Capturing temporal variability for estimates of annual hydrochemical export from a first-order agricultural catchment in southern Ontario, Canada. *Hydrological Processes: An International Journal, 21*(13), 1651-1663. Doi: 10.1002/hyp.6361.

Macrae, M. L., English, M. C., Schiff, S. L., & Stone, M. (2007b). Intra-annual variability in the contribution of tile drains to basin discharge and phosphorus export in a first-order agricultural catchment. *Agricultural Water Management*, *92*(3), 171-182. Doi: 10.1016/j.agwat.2007.05.015

Martin, Y., Valeo, C., & Tait, M. (2008). Centimetre-scale digital representations of terrain and impacts on depression storage and runoff. *Catena, 75*(2), 223-233. Doi: 10.1016/j.catena.2008.07.005

McCuen, R. H., Johnson, P. A., & Ragan, R. M. (2002). Highway hydrology: Hydraulic design series number 2 (No. FHWA-NHI-02-001). National Highway Institute (US).

Mein, R. G., & Larson, C. L. (1973). Modeling infiltration during a steady rain. *Water resources research, 9*(2), 384-394. Doi: 10.1029/WR009i002p00384

Meinen, B. U., & Robinson, D. T. (2020a). Streambank topography: an accuracy assessment of UAV-based and traditional 3D reconstructions. *International Journal of Remote Sensing*, *41*(1), 1-18. Doi: 10.1080/01431161.2019.1597294

Meinen, B. U., & Robinson, D. T. (2020b). Mapping erosion and deposition in an agricultural landscape: Optimization of UAV image acquisition schemes for SfM-MVS. *Remote Sensing of Environment*, *239*, 111666. Doi: 10.1016/j.rse.2020.111666

Meinen, B. U., & Robinson, D. T. (2020c). Where did the soil go? Quantifying one year of soil erosion on a steep tile-drained agricultural field. *Science of The Total Environment*, *729*, 138320. Doi: 10.1016/j.scitotenv.2020.138320

Menzies-Pluer, E. M., Robinson, D. T., Meinen, B. U., & Macrae, M. L. (2020). Pairing soil sampling with very-high resolution UAV imagery: An examination of drivers of soil and nutrient movement and agricultural productivity in southern Ontario. *Geoderma*, *379*, 114630. Doi: 10.1016/j.geoderma.2020.114630

Meinen, B. U., & Robinson, D. T. (2021). Agricultural erosion modelling: evaluating USLE and WEPP field-scale erosion estimates using UAV time-series data. *Environmental Modelling & Software, 104962*. Doi: 10.1016/j.envsoft.2021.104962

Meyer, L. D., & Moldenhauer, W. C. (1985). Soil erosion by water: the research experience. *Agricultural History*, *59*(2), 192-204.

Michalak, A. M., Anderson, E. J., Beletsky, D., Boland, S., Bosch, N. S., Bridgeman, T. B., ... & Zagorski, M. A. (2013). Record-setting algal bloom in Lake Erie caused by agricultural and meteorological trends consistent with expected future conditions. *Proceedings of the National Academy of Sciences*, *110*(16), 6448-6452. Doi: 10.1073/pnas.1216006110

Mishra, S. K., Chaudhary, A., Shrestha, R. K., Pandey, A., & Lal, M. (2014). Experimental verification of the effect of slope and land use on SCS runoff curve number. *Water resources management, 28*(11), 3407-3416. Doi: 10.1007/s11269-014-0582-6

Mitasova, H., Hofierka, J., Zlocha, M., & Iverson, L. R. (1996). Modelling topographic potential for erosion and deposition using GIS. *International journal of geographical information systems, 10*(5), 629-641. Doi: 10.1080/02693799608902101

Montanarella, L. (2007). Trends in land degradation in Europe. In *Climate and land degradation* (pp. 83-104). Springer, Berlin, Heidelberg. Doi: 10.1007/978-3-540-72438-4_5

Montanarella, L. (2015). Agricultural policy: Govern our soils. *Nature News*, *528*(7580), 32. Doi: 10.1038/528032a

Montgomery, D. R. (2007). Soil erosion and agricultural sustainability. *Proceedings of the National Academy of Sciences*, *104*(33), 13268-13272. Doi: 10.1073/pnas.0611508104

Moore, L. W., Chew, C. Y., Smith, R. H., & Sahoo, S. (1992). Modeling of best management practices on North Reelfoot Creek, Tennessee. *Water Environment Research*, *64*(3), 241-247. Doi: 10.2175/WER.64.3.8

Moore, I. D., & Wilson, J. P. (1992). Length-slope factors for the Revised Universal Soil Loss Equation: Simplified method of estimation. *Journal of soil and water conservation, 47*(5), 423-428.

Morgan, R. P. C., Quinton, J. N., Smith, R. E., Govers, G., Poesen, J. W. A., Auerswald, K., ... & Styczen, M. E. (1998). The European Soil Erosion Model (EUROSEM): a dynamic

approach for predicting sediment transport from fields and small catchments. *Earth Surface Processes and Landforms: The Journal of the British Geomorphological Group*, *23*(6), 527-544. Doi: 10.1002/(SICI)1096-9837(199806)23:6<527::AID-ESP868>3.0.CO;2-5

Morgan, R. P. C., & Nearing, M. A. (Eds.). (2011). *Handbook of erosion modelling*. West Sussex: Wiley-Blackwell.

Musgrave, G. W. (1947). The quantitative evaluation of factors in water erosion: a first approximation. *Journal of soil and water conservation*, *2*, 133-138.

Nash, J. E., & Sutcliffe, J. V. (1970). River flow forecasting through conceptual models part I—A discussion of principles. *Journal of hydrology*, *10*(3), 282-290. Doi: 10.1016/0022-1694(70)90255-6

Napoli, M., Cecchi, S., Orlandini, S., Mugnai, G., & Zanchi, C. A. (2016). Simulation of field-measured soil loss in Mediterranean hilly areas (Chianti, Italy) with RUSLE. *Catena*, *145*, 246-256. Doi: 10.1016/j.catena.2016.06.018

Nearing, M. A., Govers, G., & Norton, L. D. (1999). Variability in soil erosion data from replicated plots. *Soil science society of America Journal*, *63*(6), 1829-1835. Doi: 10.2136/sssaj1999.6361829x

Neugirg, F., Stark, M., Kaiser, A., Vlacilova, M., Della Seta, M., Vergari, F., ... & Haas, F. (2016). Erosion processes in calanchi in the Upper Orcia Valley, Southern Tuscany, Italy based on multitemporal high-resolution terrestrial LiDAR and UAV surveys. *Geomorphology*, *269*, 8-22. Doi: 10.1016/j.geomorph.2016.06.027

Ngatunga, E. L. N., Lal, R., & Uriyo, A. P. (1984). Effects of surface management on runoff and soil erosion from some plots at Mlingano, Tanzania. *Geoderma*, *33*(1), 1-12. Doi: 10.1016/0016-7061(84)90086-7

Niethammer, U., James, M. R., Rothmund, S., Travelletti, J., & Joswig, M. (2012). UAV-based remote sensing of the Super-Sauze landslide: Evaluation and results. *Engineering Geology*, *128*, 2-11. Doi: 10.1016/j.enggeo.2011.03.012

Nolan, M., Larsen, C., & Sturm, M. (2015). Mapping snow depth from manned aircraft on landscape scales at centimeter resolution using structure-from-motion photogrammetry. *The Cryosphere*, *9*(4), 1445-1463. Doi: 10.5194/tcd-9-333-2015

Okoba, B. O., & De Graaff, J. (2005). Farmers' knowledge and perceptions of soil erosion and conservation measures in the Central Highlands, Kenya. *Land Degradation & Development*, *16*(5), 475-487. Doi: 10.1002/ldr.678

Panagos, P., Borrelli, P., Poesen, J., Ballabio, C., Lugato, E., Meusburger, K., ... & Alewell, C. (2015a). The new assessment of soil loss by water erosion in Europe. *Environmental science & policy*, *54*, 438-447. Doi: 10.1016/j.envsci.2015.08.012

Panagos, P., Ballabio, C., Borrelli, P., Meusburger, K., Klik, A., Rousseva, S., ... & Alewell, C. (2015b). Rainfall erosivity in Europe. *Science of the Total Environment*, *511*, 801-814. Doi: 10.1016/j.scitotenv.2015.01.008

Pandey, A., Chowdary, V. M., & Mal, B. C. (2007). Identification of critical erosion prone areas in the small agricultural watershed using USLE, GIS and remote sensing. *Water resources management*, *21*(4), 729-746. Doi: 10.1007/s11269-006-9061-z

Parry, R. (1998). Agricultural phosphorus and water quality: A US Environmental Protection Agency perspective. *Journal of Environmental Quality*, *27*(2), 258-261.

Pimentel, D., Harvey, C., Resosudarmo, P., Sinclair, K., Kurz, D., McNair, M., ... & Blair, R. (1995). Environmental and economic costs of soil erosion and conservation benefits. *Science*, *267*(5201), 1117-1123. Doi: 10.1126/science.267.5201.1117

Pimentel, D. (2006). Soil erosion: a food and environmental threat. *Environment, development and sustainability*, *8*(1), 119-137. Doi: 10.1007/s10668-005-1262-8

Peter, K. D., d'Oleire-Oltmanns, S., Ries, J. B., Marzolff, I., & Hssaine, A. A. (2014). Soil erosion in gully catchments affected by land-levelling measures in the Souss Basin, Morocco, analysed by rainfall simulation and UAV remote sensing data. *Catena*, *113*, 24-40. Doi: 10.1016/j.catena.2013.09.004

Pineux, N., Lisein, J., Swerts, G., Bielders, C. L., Lejeune, P., Colinet, G., & Degré, A. (2017). Can DEM time series produced by UAV be used to quantify diffuse erosion in an agricultural watershed?. *Geomorphology*, *280*, 122-136. Doi: 10.1016/j.geomorph.2016.12.003

Poesen, J. (2018). Soil erosion in the Anthropocene: Research needs. *Earth Surface Processes and Landforms, 43(*1), 64-84. Doi: 10.1002/esp.4250

Prasuhn, V., Liniger, H., Gisler, S., Herweg, K., Candinas, A., & Clément, J. P. (2013). A high-resolution soil erosion risk map of Switzerland as strategic policy support system. *Land use policy*, *32*, 281-291. Doi: 10.1016/j.landusepol.2012.11.006

Rao, N. S., Easton, Z. M., Schneiderman, E. M., Zion, M. S., Lee, D. R., & Steenhuis, T. S. (2009). Modeling watershed-scale effectiveness of agricultural best management practices to reduce phosphorus loading. *Journal of Environmental Management*, *90*(3), 1385-1395. Doi: 10.1016/j.jenvman.2008.08.011

Renard, K. G., Foster, G. R., Weesies, G. A., & Porter, J. P. (1991). RUSLE: Revised universal soil loss equation. *Journal of soil and Water Conservation*, *46*(1), 30-33.

Ricci, G. F., Jeong, J., De Girolamo, A. M., & Gentile, F. (2020). Effectiveness and feasibility of different management practices to reduce soil erosion in an agricultural watershed. *Land use policy*, *90*, 104306. Doi: 10.1016/j.landusepol.2019.104306

Richter, G. (1983). Aspects and problems of soil erosion hazard in the EEC countries.

Richter, B. D., Braun, D. P., Mendelson, M. A., & Master, L. L. (1997). Threats to imperiled freshwater fauna: amenazas a la fauna dulceacuicola en riesgo. *Conservation biology*, *11*(5), 1081-1093. Doi: 10.1046/j.1523-1739.1997.96236.x

Rizeei, H. M., Saharkhiz, M. A., Pradhan, B., & Ahmad, N. (2016). Soil erosion prediction based on land cover dynamics at the Semenyih watershed in Malaysia using LTM and USLE models. *Geocarto international*, *31*(10), 1158-1177. Doi: 10.1080/10106049.2015.1120354

Rodriguez, J. M., Molnar, J. J., Fazio, R. A., Sydnor, E., & Lowe, M. J. (2009). Barriers to adoption of sustainable agriculture practices: Change agent perspectives. *Renewable agriculture and food systems*, 60-71. Doi: 10.1017/S1742170508002421

Rompaey, A. J. V., & Govers, G. (2002). Data quality and model complexity for regional scale soil erosion prediction. *International Journal of Geographical Information Science*, *16*(7), 663-680. Doi: 10.1080/13658810210148561

Roose, E. J. (1977). Application of the USLE of Wischmeier and Smith in West Africa. *Greenland, D.J. and R. Lal. Soil conservation and management in the humid tropics. Chichester, Wiley*, 177-188.

Rousseau, A. N., Savary, S., Hallema, D. W., Gumiere, S. J., & Foulon, É. (2013). Modeling the effects of agricultural BMPs on sediments, nutrients, and water quality of the Beaurivage River watershed (Quebec, Canada). *Canadian Water Resources Journal*, *38*(2), 99-120. Doi: 10.1080/07011784.2013.780792

Ryan, P. A. (1991). Environmental effects of sediment on New Zealand streams: a review. *New Zealand journal of marine and freshwater research, 25*(2), 207-221. Doi: 10.1080/00288330.1991.9516472

Ryan, J. C., Hubbard, A. L., Box, J. E., Todd, J., Christoffersen, P., Carr, J. R., ... & Snooke, N. (2015). UAV photogrammetry and structure from motion to assess calving dynamics at Store Glacier, a large outlet draining the Greenland ice sheet. *The Cryosphere*, *9*(1), 1-11. Doi: 10.5194/tc-9-1-2015

Santhi, C., Srinivasan, R., Arnold, J. G., & Williams, J. R. (2006). A modeling approach to evaluate the impacts of water quality management plans implemented in a watershed in Texas. *Environmental modelling & software*, *21*(8), 1141-1157. Doi: 10.1016/j.envsoft.2005.05.013

Sanz-Ablanedo, E., Chandler, J. H., Rodríguez-Pérez, J. R., & Ordóñez, C. (2018). Accuracy of unmanned aerial vehicle (UAV) and SfM photogrammetry survey as a function of the number and location of ground control points used. *Remote Sensing*, *10*(10), 1606. Doi: 10.3390/rs10101606

Singer, J. W., Kohler, K. A., Liebman, M., Richard, T. L., Cambardella, C. A., & Buhler, D. D. (2004). Tillage and compost affect yield of corn, soybean, and wheat and soil fertility. *Agronomy Journal*, *96*(2), 531-537. Doi: 10.2134/agronj2004.5310

Singh, G., & Panda, R. K. (2017). Grid-cell based assessment of soil erosion potential for identification of critical erosion prone areas using USLE, GIS and remote sensing: A case study in the Kapgari watershed, India. *International Soil and Water Conservation Research*, *5*(3), 202-211. Doi: 10.1016/j.iswcr.2017.05.006

Smith, D. D. (1941). Interpretation of soil conservation data for field use. *Agric. Engg.*, *22*, 173-175.

Smith, C. M., Williams, J. R., Nejadhashemi, A., Woznicki, S. A., & Leatherman, J. C. (2014). Cost-effective targeting for reducing soil erosion in a large agricultural watershed. *Journal*

of Agricultural and Applied Economics, *46*(1379-2016-113913), 509-526. Doi: 10.22004/ag.econ.189140

Smith, M. W., & Vericat, D. (2015). From experimental plots to experimental landscapes: topography, erosion and deposition in sub-humid badlands from structure-from-motion photogrammetry. *Earth Surface Processes and Landforms*, *40*(12), 1656-1671. Doi: 10.1002/esp.3747

Smith, M. W., Carrivick, J. L., & Quincey, D. J. (2016). Structure from motion photogrammetry in physical geography. *Progress in Physical Geography*, *40*(2), 247-275. Doi: 10.1177/0309133315615805

Statistics Canada, (2011). Farm Environmental Management Survey. https://www150.statcan.gc.ca/n1/pub/21-023-x/21-023-x2013001-eng.pdf

Statistics Canada (2016). Table 32-10-0408-01 Tillage practices used to prepare land for seeding. https://doi.org/10.25318/3210040801-eng

Statistics Canada (2017). 2016 Census of Agriculture. https://www150.statcan.gc.ca/n1/daily-quotidien/170510/dq170510a-eng.htm.

Stöcker, C., Eltner, A., & Karrasch, P. (2015). Measuring gullies by synergetic application of UAV and close range photogrammetry—A case study from Andalusia, Spain. *Catena*, *132*, 1-11. Doi: 10.1016/j.catena.2015.04.004

Stroosnijder, L. (2005). Measurement of erosion: is it possible?. *Catena*, *64*(2-3), 162-173. Doi: 10.1016/j.catena.2005.08.004

Stumpf, A., Malet, J. P., Allemand, P., Pierrot-Deseilligny, M., & Skupinski, G. (2015). Ground-based multi-view photogrammetry for the monitoring of landslide deformation and erosion. *Geomorphology*, *231*, 130-145. Doi: 10.1016/j.geomorph.2014.10.039

Syvitski, J. P., Vörösmarty, C. J., Kettner, A. J., & Green, P. (2005). Impact of humans on the flux of terrestrial sediment to the global coastal ocean. *science*, *308*(5720), 376-380. Doi: 10.1126/science.1109454

Takken, I., Beuselinck, L., Nachtergaele, J., Govers, G., Poesen, J., & Degraer, G. (1999). Spatial evaluation of a physically-based distributed erosion model (LISEM). *Catena*, *37*(3-4), 431-447. Doi: 10.1016/S0341-8162(99)00031-4

Tamminga, A. D., Eaton, B. C., & Hugenholtz, C. H. (2015). UAS-based remote sensing of fluvial change following an extreme flood event. *Earth Surface Processes and Landforms*, *40*(11), 1464-1476. Doi: 10.1002/esp.3728

Thompson, S. E., Katul, G. G., & Porporato, A. (2010). Role of microtopography in rainfall-runoff partitioning: An analysis using idealized geometry. *Water Resources Research, 46*(7). Doi: 10.1029/2009WR008835

Tilman, D., Balzer, C., Hill, J., & Befort, B. L. (2011). Global food demand and the sustainable intensification of agriculture. *Proceedings of the national academy of sciences*, *108*(50), 20260-20264. Doi: 10.1073/pnas.1116437108

Tiwari, A. K., Risse, L. M., & Nearing, M. A. (2000). Evaluation of WEPP and its comparison with USLE and RUSLE. *Transactions of the ASAE*, *43*(5), 1129. Doi: 10.13031/2013.3005

Toy, T. J., Foster, G. R., & Renard, K. G. (2002). *Soil erosion: processes, prediction, measurement, and control*. John Wiley & Sons.

Triggs, B., McLauchlan, P. F., Hartley, R. I., & Fitzgibbon, A. W. (1999). Bundle adjustment—a modern synthesis. In *International workshop on vision algorithms* (pp. 298-372). Springer, Berlin, Heidelberg. Doi: 10.1007/3-540-44480-7_21

Trimble, S. W., & Crosson, P. (2000). US soil erosion rates--myth and reality. *Science*, *289*(5477), 248-250. Doi: 10.1126/science.289.5477.248

Troeh, F. R., & Thompson, L. M. (2005). *Soils and soil fertility* (Vol. 489). New York, USA: Blackwell.

Turner, D., Lucieer, A., & De Jong, S. M. (2015). Time series analysis of landslide dynamics using an unmanned aerial vehicle (UAV). *Remote Sensing*, *7*(2), 1736-1757. Doi: 10.3390/rs70201736

Uri, N. D. (2000). Agriculture and the environment–the problem of soil erosion. *Journal of Sustainable Agriculture*, *16*(4), 71-94. Doi: 10.1300/J064v16n04_07

USDA (1971). Sediment Sources, Yields, and Delivery Ratios, Section 3. National Engineering Handbook. United States Department of Agriculture and Soil Conservation Services.

Uusi-Kämppä, J., Yläranta, T., & Mulamoottil, G. (1996). Effect of buffer strips on controlling soil erosion and nutrient losses in southern Finland. *Wetlands: Environmental Gradients,*

Boundaries, and Buffers, G. Mulamoottil, BG Warner, and EA McBean (Editors). CRC Press, Lewis Publishers, Boca Raton, Florida, 221-235.

Uusitalo, R., Turtola, E., Kauppila, T., & Lilja, T. (2001). Particulate phosphorus and sediment in surface runoff and drainflow from clayey soils. *Journal of Environmental Quality*, *30*(2), 589-595. Doi: 10.2134/jeq2001.302589x

Van der Knijff, J. M. F., Jones, R. J. A., & Montanarella, L. (1999). *Soil erosion risk assessment in Italy*. European Soil Bureau, European Commission.

Van Oost, K., Govers, G., Cerdan, O., Thauré, D., Van Rompaey, A., Steegen, A., ... & Poesen, J. (2005). Spatially distributed data for erosion model calibration and validation: The Ganspoel and Kinderveld datasets. *Catena*, *61*(2-3), 105-121. Doi: 10.1016/j.catena.2005.03.001

Van Oost, K., Govers, G., De Alba, S., & Quine, T. A. (2006). Tillage erosion: a review of controlling factors and implications for soil quality. *Progress in Physical Geography*, *30*(4), 443-466. Doi: 10.1191/0309133306pp487ra

Van Rompaey, A. J., Verstraeten, G., Van Oost, K., Govers, G., & Poesen, J. (2001). Modelling mean annual sediment yield using a distributed approach. *Earth Surface Processes and Landforms*, *26*(11), 1221-1236. Doi: 10.1002/esp.275

Vanmaercke, M., Poesen, J., Govers, G., & Verstraeten, G. (2015). Quantifying human impacts on catchment sediment yield: A continental approach. *Global and Planetary Change*, *130*, 22-36. Doi: 10.1016/j.gloplacha.2015.04.001

Wakatsuki, T., & Rasyidin, A. (1992). Rates of weathering and soil formation. *Geoderma*, *52*(3-4), 251-263. Doi: 10.1016/0016-7061(92)90040-E

Wall, G. J., Coote, D. R., Pringle, E. A., & Shelton, I. J. (2002). RUSLEFAC—Revised universal soil loss equation for application in Canada: A handbook for estimating soil loss from water erosion in Canada. *Research Branch, Agriculture and Agri-Food Canada. Ottawa.*

Walling, D. E. (1983). The sediment delivery problem. *Journal of hydrology*, *65*(1-3), 209-237. Doi: 10.1016/0022-1694(83)90217-2

Walling, D. E., Russell, M. A., Hodgkinson, R. A., & Zhang, Y. (2002). Establishing sediment budgets for two small lowland agricultural catchments in the UK. *Catena*, *47*(4), 323-353. Doi: 10.1016/S0341-8162(01)00187-4

Walling, D. E., He, Q., & Whelan, P. A. (2003). Using 137Cs measurements to validate the application of the AGNPS and ANSWERS erosion and sediment yield models in two small Devon catchments. *Soil and Tillage Research*, *69*(1-2), 27-43. Doi: 10.1016/S0167-1987(02)00126-5

Wendt, R. C., Alberts, E. E., & Hjelmfelt Jr, A. T. (1986). Variability of runoff and soil loss from fallow experimental plots. *Soil Science Society of America Journal*, *50*(3), 730-736. Doi: 10.2136/sssaj1986.03615995005000030035x

Williams, J. R. (1975). Sediment-yield prediction with universal equation using runoff energy factor. *Present and prospective technology for predicting sediment yields and sources*, *40*, 244-252.

Williams, J. R. (1989). EPIC: The erosion-productivity impact calculator.

Wilson, G. V., Dabney, S. M., McGregor, K. C., & Barkoll, B. D. (2004). Tillage and residue effects on runoff and erosion dynamics. *Transactions of the ASAE*, *47*(1), 119. Doi: 10.13031/2013.15878

Wischmeier, W. H., & Smith, D. D. (1965). *Predicting rainfall-erosion losses from cropland east of the Rocky Mountains: Guide for selection of practices for soil and water conservation* (No. 282). Agricultural Research Service, US Department of Agriculture.

Wischmeier, W. H., & Smith, D. D. (1978). *Predicting rainfall erosion losses: a guide to conservation planning* (No. 537). Department of Agriculture, Science and Education Administration.

World Resources Institute. (1986). Annual Report, Washington, DC.

Young, R. A., Onstad, C. A., Bosch, D. D., & Anderson, W. P. (1989). AGNPS: A nonpoint-source pollution model for evaluating agricultural watersheds. *Journal of soil and water conservation*, *44*(2), 168-173.

Yuan, Y., Locke, M. A., & Bingner, R. L. (2008). Annualized agricultural non-point source model application for Mississippi Delta Beasley Lake watershed conservation practices assessment. *journal of soil and water conservation*, *63*(6), 542-551. Doi: 10.2489/jswc.63.6.542

Yuan, Y., Bingner, R. L., & Locke, M. A. (2009). A review of effectiveness of vegetative buffers on sediment trapping in agricultural areas. *Ecohydrology: Ecosystems, Land and Water Process Interactions, Ecohydrogeomorphology, 2*(3), 321-336. Doi: 10.1002/eco.82

Zingg, A. W. (1940). Degree and length of land slope as it affects soil loss in run-off. *Agric. Engng.*, *21*, 59-64.

Appendix A: Chapter 3 supplementary material

Fig. A1. Skyranger R60 UAV system used for all data acquisitions (left) and a ground control point (GCP; right).

Fig. A2. Aerial picture of the northern half of the study site on June 15, 2018 (left), and July 14, 2018 (right).

Fig. A3. Depositional plume in the catch basin of Basin B after multiple spring-time erosion events (left; June 15, 2018) and after a winter of erosion events (right; May 16, 2019).

Fig. A4. Depositional plume in the catch basin of Basin E after multiple spring-time erosion events (left; June 15, 2018) and after a winter of erosion events (right; May 16, 2019).

Fig. A5. Water erosion in Basin A after multiple spring-time erosion events (June 15, 2018).

Fig. A6. Tile outlets at the field edge.

Appendix B: Chapter 4 supplementary material

Table B1. 2018 – 2019 USLE R-derivation Table. R_s of 238.02 not included in R calculations.

Date	E (MJ ha^{-1})	I_{30} (mm h^{-1})	EI_{30} (MJ mm ha^{-1} h^{-1})
5/20/2018	3.11	15.29	47.59
5/31/2018	3.35	13.41	45.00
6/23/2018	1.96	5.93	11.61
6/24/2018	6.01	13.41	80.68
7/16/2018	8.11	49.60	402.11
7/21/2018	2.05	6.55	13.41
8/6/2018	4.09	27.76	113.68
8/8/2018	5.83	23.40	136.48
8/17/2018	13.18	40.55	534.44
8/21/2018	4.67	22.15	103.38
8/25/2018	2.69	11.54	31.03
10/1/2018	3.65	3.74	13.65
10/31/2018	4.78	10.92	52.22
11/2/2018	3.27	4.68	15.32
11/26/2018	2.81	4.68	13.14
12/21/2018	2.29	5.93	13.58
1/23/2019	4.68	15.60	73.05
3/30/2019	5.69	6.55	37.28
4/8/2019	2.41	7.49	18.07
4/14/2019	1.60	3.43	5.51
4/19/2019	2.92	5.61	16.41
4/20/2019	1.67	5.30	8.84
4/26/2019	4.19	8.42	35.32
5/1/2019	2.30	4.68	10.78
5/10/2019	3.72	13.10	48.68
		Total (R):	**1881.26**

Table B2. USLE crop-stage soil losses (t): Seedbed (SB), Establishment (1), Development (2), Maturing Crop (3), Stubble (4), Rough fallow (F).

Basin	Size (ha)	SB	1	2	3	4	F	Total
A-1	0.87	1.11	2.61	5.67	7.19	0.11	4.23	20.92
A-2	0.63	1.22	2.87	6.22	7.88	0.12	4.64	22.94
A-3	1.77	2.97	6.99	15.18	19.23	0.29	11.31	55.98
B-1	1.30	1.77	4.17	9.04	11.46	0.17	6.74	33.35
B-2	0.42	0.84	1.99	4.31	5.46	0.08	3.21	15.90
B-3	0.97	1.61	3.78	8.21	10.40	0.16	6.12	30.26
C	0.22	0.08	0.19	0.41	0.51	0.01	0.30	1.50
D	0.48	0.33	0.78	1.68	2.13	0.03	1.25	6.21
E	0.73	0.70	1.64	3.55	4.50	0.07	2.65	13.10
F	1.09	1.19	2.79	6.06	7.67	0.12	4.52	22.34
							Total:	**222.50**

Appendix C: Chapter 6 supplementary material

USLE recommend modelling approach

USLE calculations were conducted in ArcGIS 10.6.1 and the details of each processing step are included in this appendix. For the discretization of the upper-Nith Watershed, a fixed 1:4000 scale was used to draw each farm field boundary using SWOOP 2015 airborne imagery. Farm fields with no barriers between them were digitized as adjacent polygons, whereas farm fields with a windbreak or barrier that would block sediment flow were digitized with a gap between polygons where the barrier was. The accuracy of the farm field polygon layer is ± 2 m for identifying farm field edges. All the USLE factors were summarized as attributes for each farm-field polygon and calculated using the following methodology:

L-factor:

Data inputs: 2mDEM (2 m Digital Elevation Model), farm_fields (polygon of discretized farm fields)

(1) **Extract by mask** (Input raster = 2mDEM, feature mask data = farm_fields, output raster = clipped_DEM)

(2) **Fill** (input surface raster = clipped_DEM, output surface raster = filled_DEM, z limit = 0.4 m)

(3) **D8 flow direction** (input surface raster = filled_DEM, output flow direction raster = D8_flow)

(4) **D8 flow accumulation** (input flow direction raster = D8_flow, output accumulation raster = D8_accumulation)

(5) **Raster calculator**. Expression: (Power((“D8_accumulation” * [2] / 22.13),0.6)). Output raster = L_factor

Note: 22.13 refers to the length of a unit plot (meters), [2] is the spatial resolution of the data set, and 0.6 refers to the exponent (m = 0.6). The exponent m is most commonly set to a value of 0.4 in literature.

S-factor:

Date inputs: 2mDEM (2 m Digital Elevation Model), farm_fields (polygon of discretized farm fields), farm_basins_poly (polygon of basins; see the SDR Methodology for calculation of this layer)

(1) **Aggregate** (Input raster = 2mDEM, output raster = 4m_DEM, cell factor = 2, aggregation technique = mean)

(2) **Slope** (Input raster = 4m_DEM, output raster = deg_slope, output measurement = DEGREE)

(3) **Resample** (Input raster = deg_slope, output raster = deg_slope_2m, X = 2, Y = 2, resampling technique = NEAREST)

Note: resampling to the same spatial resolution as the L_factor.

(4) **Zonal Statistics** (Feature zone data = farm_basins_poly, zone field = FID, input value raster = deg_slope_2m, output raster = deg_basin_slope, statistics type = MEAN)

Note: we are calculating the average slope for each catchment area, not for each cell or field polygon.

(5) **Raster calculator**. Expression (Power(((Sin("deg_basin_slope"*0.01745))/0.0896), 1.3)). Output raster = S_factor.

Note: 0.01745 is a conversion factor for degrees to radians, and 1.3 refers to the exponent (n = 1.3).

LS-factor:

(1) **Raster calculator.** Expression (L_factor * S_factor * 1.6).

The LS-factor is based off Griffin et al. (1988; m= 0.6, n = 1.3) for calculating erosion at a point:

$$LS = (\frac{Specific\ Catchment\ Area}{22.13})^{0.6} * \left(\frac{\sin\theta}{0.0896}\right)^{1.3} * (1.6)$$

K-factor:

Data inputs: Soil_poly (Ontario Soil Survey Complex Polygon)

(1) Field calculator (Soil_poly):

$$100K = (2.1M^{1.14}\,(10^{-4})(12-a) + 3.25(b-2) + 2.5(c-3))\ \times 0.1317$$

a = 4% (organic matter content; estimated average)
b = 2 (fine granular)
c = 1, 2.5, 4.5, or 6 (profile permeability class)

c is calculated from the HYDRO1 attribute, whereby HYDRO1 “A”, c = 1, HYDRO1 “B”, c = 2.5, HYDRO1 “C”, c = 4.5, HYDRO1 “D”, c = 6.

M is calculated from the ATEXTURE1 attribute, whereby the textural class is assigned as clay loam, fine sandy loam, loam, silty clay loam, silt loam, sandy loam, or organic.

R-factor:

Data inputs: Precipitation.xls (Wellesley Dam meteorological station hourly precipitation data)

(1) Calculated using the methodology outlined in Agricultural Handbook no. 537 (p. 5 - 7, p. 50 – 51; Wischmeier and Smith 1978) using hourly rainfall data with the conversion of Panagos et al. (2015b) to convert from 60-minute intensities to 30-minute intensities. This correction will introduce some amount of uncertainty and is only recommended if 30-minute rainfall data is not available.

Table C1. R-factor (MJ mm ha^{-1} hr^{-1} yr^{-1}) for each year. Average annual R-value: 1923.

	2010	**2011**	**2012**	**2013**	**2014**
R-factor	1336	1438	870	2763	3210

C-factor:

Data inputs: census.xls (Canadian 2016 Census of Agriculture)

(1) Calculated using the methodology outlined Agricultural Handbook no. 537 (see p. 22-26 and Table 8, p.30; Wischmeier and Smith 1978) using land use and management data from the 2016 Canadian Census of Agriculture.

Table C2. USLE C-factor derivation table. Assuming a 40% cover after plant for chisel system, 70% disked residue for wheat, and 10% residue left on field for an alfalfa plant in a moldboard system. Alfalfa has a spring seeding with no nurse crop and is cut in September. Alfalfa stands are 4-years long. Wheat has a fall seeding after soybeans are harvested and is cut in July of the following year. Plowing implement abbreviations: moldboard [M], chisel [C], and no-till [NT]. All crop stages and planting and harvest dates are estimated based on precipitation patterns and local knowledge.

Corn [M]	2010	C	2011	C	2012	C	2013	C	2014	C
Fallow		0.106		0.067		0.000		0.035		0.043
Seedbed	20-May	0.045	12-May	0.082	24-May	0.062	17-May	0.133	27-May	0.010
Establishment	10-Jun	0.053	2-Jun	0.203	14-Jun	0.042	7-Jun	0.053	17-Jun	0.303
Development	11-Jul	0.126	3-Jul	0.000	15-Jul	0.117	8-Jul	0.020	18-Jul	0.067
Mature	10-Aug	0.037	2-Aug	0.047	14-Aug	0.082	7-Aug	0.049	17-Aug	0.016
Fallow	11-Nov	0.095	6-Nov	0.116	10-Nov	0.220	15-Oct	0.142	14-Oct	0.040
Total:		**0.462**		**0.516**		**0.523**		**0.431**		**0.479**
Corn [C]	2010	C	2011	C	2012	C	2013	C	2014	C
Fallow		0.046		0.029		0.000		0.015		0.019
Seedbed	20-May	0.010	12-May	0.019	24-May	0.014	17-May	0.031	27-May	0.002
Establishment	10-Jun	0.013	2-Jun	0.050	14-Jun	0.010	7-Jun	0.013	17-Jun	0.074
Development	11-Jul	0.036	3-Jul	0.000	15-Jul	0.034	8-Jul	0.006	18-Jul	0.020
Mature	10-Aug	0.019	2-Aug	0.024	14-Aug	0.041	7-Aug	0.024	17-Aug	0.008
Fallow	11-Nov	0.041	6-Nov	0.050	10-Nov	0.095	15-Oct	0.061	14-Oct	0.017
Total:		**0.165**		**0.172**		**0.194**		**0.150**		**0.140**
Alfalfa [M]	2010	C	2011	C	2012	C	2013	C	2014	C
Fallow		0.108		0.069		0.000		0.036		0.044
Seedbed	20-May	0.039	12-May	0.071	24-May	0.054	17-May	0.115	27-May	0.009
Establishment	10-Jun	0.043	2-Jun	0.165	14-Jun	0.034	7-Jun	0.043	17-Jun	0.246
Development	11-Jul	0.099	3-Jul	0.000	15-Jul	0.092	8-Jul	0.016	18-Jul	0.053
Mature	10-Aug	0.004	2-Aug	0.005	14-Aug	0.008	7-Aug	0.005	17-Aug	0.002
Fall cut	21-Sep	0.004	9-Oct	0.005	29-Sep	0.010	29-Sep	0.006	29-Sep	0.002
Total:		**0.297**		**0.314**		**0.198**		**0.220**		**0.355**
Soybean [M], wheat [NT]	2010	C	2011	C	2012	C	2013	C	2014	C
Fallow		0.108		0.069		0.000		0.036		0.044
Seedbed (soy)	20-May	0.048	12-May	0.087	24-May	0.066	17-May	0.141	27-May	0.011
Establishment	10-Jun	0.057	2-Jun	0.219	14-Jun	0.046	7-Jun	0.057	17-Jun	0.326

Development	11-Jul	0.126	3-Jul	0.000	15-Jul	0.117	8-Jul	0.020	18-Jul	0.067
Mature	10-Aug	0.032	2-Aug	0.040	14-Aug	0.070	7-Aug	0.041	17-Aug	0.014
Seedbed (wheat)	21-Sep	0.003	9-Oct	0.011	29-Sep	0.005	29-Sep	0.009	29-Sep	0.002
Establishment	12-Oct	0.001	30-Oct	0.000	20-Oct	0.006	20-Oct	0.028	20-Oct	0.005
Development	12-Nov	0.004	30-Nov	0.001	20-Nov	0.002	20-Nov	0.001	20-Nov	0.000
Total:		**0.379**		**0.427**		**0.311**		**0.334**		**0.469**
Soybean [C], wheat [NT]	2010	C	2011	C	2012	C	2013	C	2014	C
Fallow		0.041		0.026		0.000		0.014		0.017
Seedbed (soy)	20-May	0.012	12-May	0.022	24-May	0.016	17-May	0.035	27-May	0.003
Establishment	10-Jun	0.017	2-Jun	0.065	14-Jun	0.014	7-Jun	0.017	17-Jun	0.097
Development	11-Jul	0.056	3-Jul	0.000	15-Jul	0.052	8-Jul	0.009	18-Jul	0.030
Mature	10-Aug	0.032	2-Aug	0.040	14-Aug	0.070	7-Aug	0.041	17-Aug	0.014
Seedbed (wheat)	21-Sep	0.003	9-Oct	0.011	29-Sep	0.005	29-Sep	0.009	29-Sep	0.002
Establishment	12-Oct	0.001	30-Oct	0.000	20-Oct	0.006	20-Oct	0.028	20-Oct	0.005
Development	12-Nov	0.004	30-Nov	0.001	20-Nov	0.002	20-Nov	0.001	20-Nov	0.000
Total:		**0.166**		**0.165**		**0.164**		**0.154**		**0.167**
Wheat [NT]	2010	C	2011	C	2012	C	2013	C	2014	C
Development		0.026		0.019		0.000		0.011		0.011
Mature	11-Apr	0.010	29-Apr	0.010	19-Apr	0.004	19-Apr	0.006	19-Apr	0.012
Cut	26-Jul	0.052	20-Jul	0.068	31-Jul	0.165	23-Jul	0.119	24-Jul	0.063
Total:		**0.088**		**0.096**		**0.168**		**0.136**		**0.085**
Pasture [established]	2010	C	2011	C	2012	C	2013	C	2014	C
Total:		**0.011**		**0.011**		**0.011**		**0.011**		**0.011**
Alfalfa [established]	2010	C	2011	C	2012	C	2013	C	2014	C
Total:		**0.020**		**0.020**		**0.020**		**0.020**		**0.020**

Recommended SDR methodology:

Date inputs: 2mDEM (2 m Digital Elevation Model), farm_fields (polygon of discretized farm fields), Nith_River (polygon)

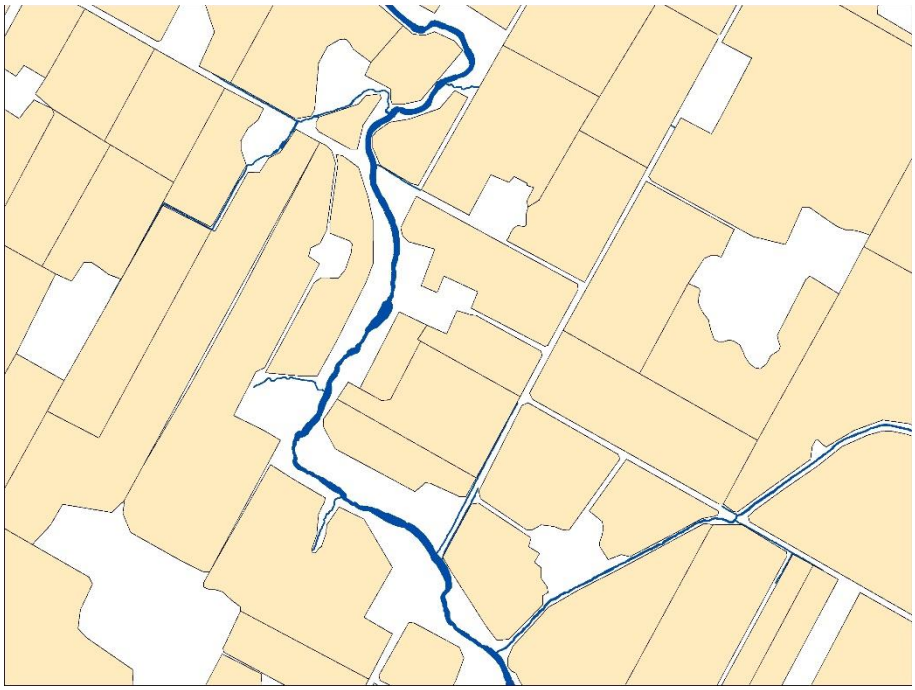

Fig. C1. SDR workflow: farm_fields polygons and Nith_River polygon.

(1) Create flow accumulation and basin rasters.

   a. **Extract by mask** (Input raster = 2mDEM, feature mask data = farm_fields, output raster = clipped_DEM)

   b. **Fill** (input surface raster = clipped_DEM, output surface raster = filled_DEM, z limit = 0.4 m)

   c. **Flow direction** (input surface raster = filled_DEM, output flow direction raster = D8_flow, flow direction type = D8)

   d. **Flow accumulation** (input flow direction raster = D8_flow, output accumulation raster = D8_accumulation, flow direction type = D8)

   e. **Basin** (input flow direction raster = D8 flow, output raster = farm_basins)

(2) Create a polygon (points) of all the locations where flow leaves farm fields.

   a. **Reclassify** (Input raster = D8_accumulation, reclass field = VALUE, “0 – 400” -> NoData”, output raster = flow_paths)

      Note: this step is filtering out very small flow paths that are unlikely to convey sediment; the value used of ‘400’ is subjective and should be altered to a lower or higher number indicative of the conditions of your watershed.

b. **Zonal statistics** (Input raster = farm_basins, zone field = VALUE, input value raster = flow paths, output raster = maxVal, statistic type = MAXIMUM)

c. **Raster calculato**r. Map Algebra Expression: (Con("flow_paths" == "maxVal","flow_paths")). Output raster = flow_outlet_ras

d. **Raster to point** (Input raster = flow_outlet_ras, Field = VALUE, output point features = flow_outlets)

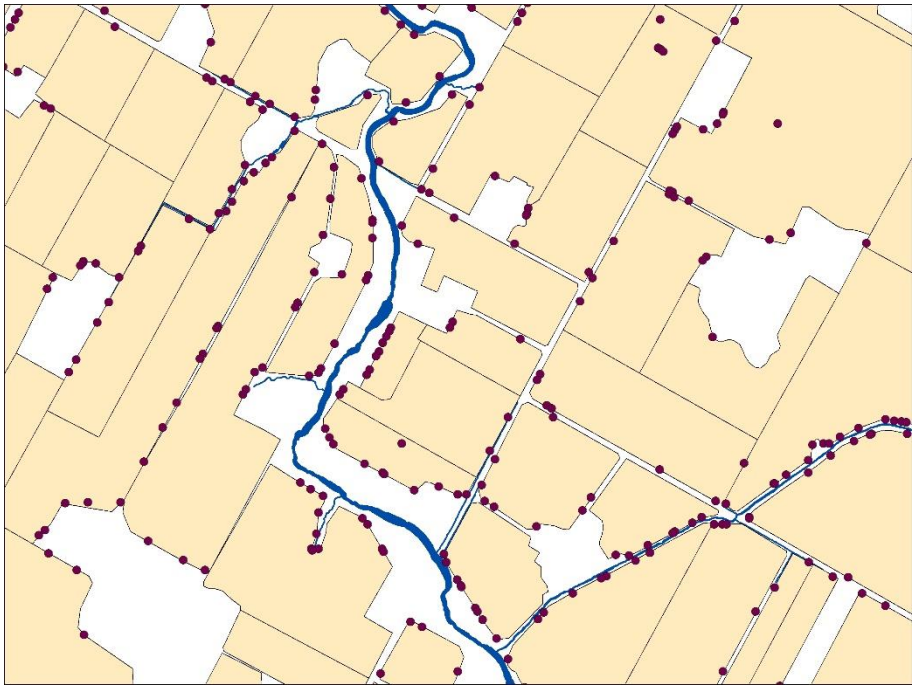

Fig. C2. SDR workflow: flow_outlets.

(3) Calculate the width of riparian zones at the point where flow leaves the field for each basin. Filter out all locations where flow outlets are not within 50 m of a waterway.

a. **Select Layer by location** (Input feature layer = flow_outlets, relationship = WITHIN A DISTANCE, selecting features = Nith_River, search distance = 50 m, selection type = NEW_SELECTION)

Note: 50 m search distance is used to indicate that riparian zones with a width of 50 m or greater will filter out 100% of sediments.

b. Flow_outlets, Data -> Export Data (Export: selected features, output feature class = sedConnectivity)

c. **Near** (Input features = sedConnectivity, near features = Nith_River, method = PLANAR)

Note: this is calculating the distance from each flow path leaving the field to a waterway.

d. **Raster to polygon** (Input raster = farm_basins, Field = Value, output polygon features = farm_basins_poly, create multipart features)

Note: Do not simplify polygons

e. **Select layer by location** (Input feature layer = farm basins poly, relationship = INTERSECT, selecting features = sedConnectivity, selection type = NEW_SELECTION)

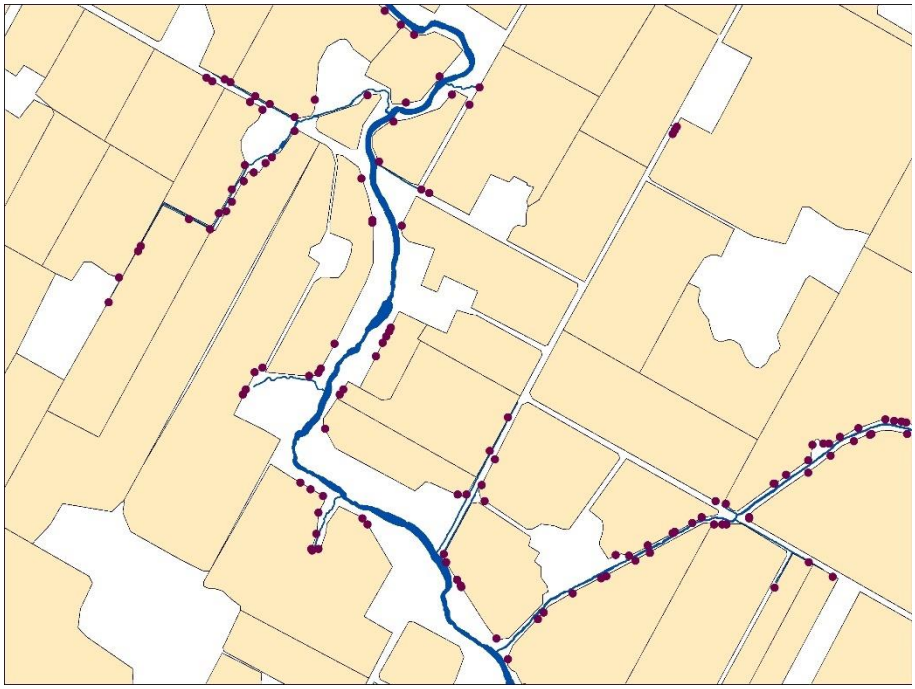

Fig. C3. SDR workflow: sedConnectivity.

f. Farm_basins_poly, Data -> Export Data (Export: selected features, output feature class = contributingBasins)

g. **Spatial join** (Target features = contributingBasins, Join features = sedConnectivity, output feature class = contributingBasins2, match option = INTERSECT)

Fig. C4. SDR workflow: contributingBasins2 polygon.

(4) Calculate the SDR specific to each basin as a function of the width of the riparian zone.

a. Create a new field in the attribute table of contributingBasins2 called “SDR” with type “DOUBLE”.

b. ContributingBasins2, NEAR_DIST -> Field Calculator, Parser = Python

```
def reclass(x):
    if (x < 1.0):
        x = 1.0
    return x


NEAR_DIST = reclass(!NEAR_DIST!)
```

Note: setting the minimum width of each riparian zone to 1 m so the equation of Yuan et al. (2009) does not return a negative value.

c. ContributingBasins2, SDR -> Field Calculator. SDR = 1 – (0.0714 * ln ([NEAR_DIST]) + 0.6774)

Note: we are calculating the filtering efficiency of the riparian zone and the SDR of each basin using a simple regression relationship developed by Yuan et al. (2009). NEAR_DIST represents the width of the riparian zone. A more accurate sediment filtering equation based on the vegetation of the riparian zones will yield more accurate results and should be used if the type of vegetation is known.

Reference:

Yuan, Y., Bingner, R. L., & Locke, M. A. (2009). A review of effectiveness of vegetative buffers on sediment trapping in agricultural areas. Ecohydrology: Ecosystems, Land and Water Process Interactions, Ecohydrogeomorphology, 2(3), 321-336. Doi: 10.1002/eco.82

(5) Calculate contributing area and SDR of each farm field using the ContributingBasins2 polygon.

a. **Polygon to Raster** (Input features = contributingBasins2, value field = SDR, cellsize = 10, output raster dataset = contributingBasins2ras)

b. **Raster to Point** (Input raster = contributingBasins2ras, field = VALUE, output point features = SDRpoints)

c. **Spatial join** (Target features = farm_fields, join features = SDRpoints, output feature class = farm_fields2, grid_code [right click on layer] merge rule = MEAN, Match option = INTERSECT)

d. Create two new fields in the attribute table of farm_fields2:

i. Name = SDR, type = DOUBLE

Field Calculator (SDR = [grid_code])

ii. Name = ContributingArea, type = DOUBLE

Field Calculator (ContributingArea = ([Join_Count] * 0.01)

Note: 0.01 is in hectares, representing the area of a 10x10m cell

Note: we are calculating the SDR and contributing area of each farm field based on the contributing basins found within each field.

e. Delete all extra fields in the attribute table of farm_fields2. This is your final polygon representing the SDR and contributing area of each farm field.

FID	Shape	Farm_Size	Slope_deg	K_Value	SDR	ContArea	LS_Value
141	Polygon	1.457011	2.92115	0.137679	0	0	0.622078
142	Polygon	0.577816	3.989	0.164324	0	0	0.985725
143	Polygon	0.409259	2.02658	0.158074	0	0	0.549739
144	Polygon	3.147584	4.04389	0.156355	0	0	1.468275
145	Polygon	6.246564	3.21877	0.144293	0.077334	5.77	1.214502
146	Polygon	7.495422	3.84905	0.127026	0.074573	2.45	1.319633
147	Polygon	2.789661	3.89315	0.296314	0	0	1.093801
148	Polygon	7.000069	1.73914	0.168373	0.146431	4.51	0.536894
149	Polygon	2.175898	1.8733	0.174856	0.185981	1.81	0.450049
150	Polygon	12.075927	1.41363	0.200128	0.173859	8.48	0.398451
151	Polygon	16.71942	2.23376	0.154114	0.150052	1.77	0.620274
152	Polygon	12.686885	1.6169	0.147565	0.150052	3.14	0.611714
153	Polygon	10.32261	1.9114	0.15058	0.150052	7.8	0.580671
154	Polygon	8.680557	1.74525	0.136429	0.150052	6.23	0.717105
155	Polygon	10.795258	1.89614	0.168009	0	0	0.468156
156	Polygon	7.151667	2.13994	0.167397	0	0	0.679424
157	Polygon	9.098586	2.68039	0.166484	0.264418	2.41	0.749563
158	Polygon	16.409473	2.92973	0.116423	0	0	0.867788

Fig. C5. SDR workflow: example attribute table of farm_fields2. SDR represents the percentage of soil lost from the field to a waterway (e.g., SDR = 0.07 indicates that 7% of total soil erosion from ContArea will become soil loss). Note: USLE factor values are imperial in this table.

Additional Figures and Data

Sediment Yield

Input Data: Sediment yield samples (2010 – 2014, n = 41; Environment Canada New Hamburg Station 16018403202), discharge measurements (2010- 2014; Environment Canada Nith River at New Hamburg 02GA018). To calculate the average annual sediment yield, we did a simple linear regression relating discharge (Y; $m^3\ s^{-1}$) to particulate concentration (x; mg L^{-1}); Y = 1.9158x + 28.198 (R^2 = 0.47). The concentration of particulates linearly increases as discharge increases.

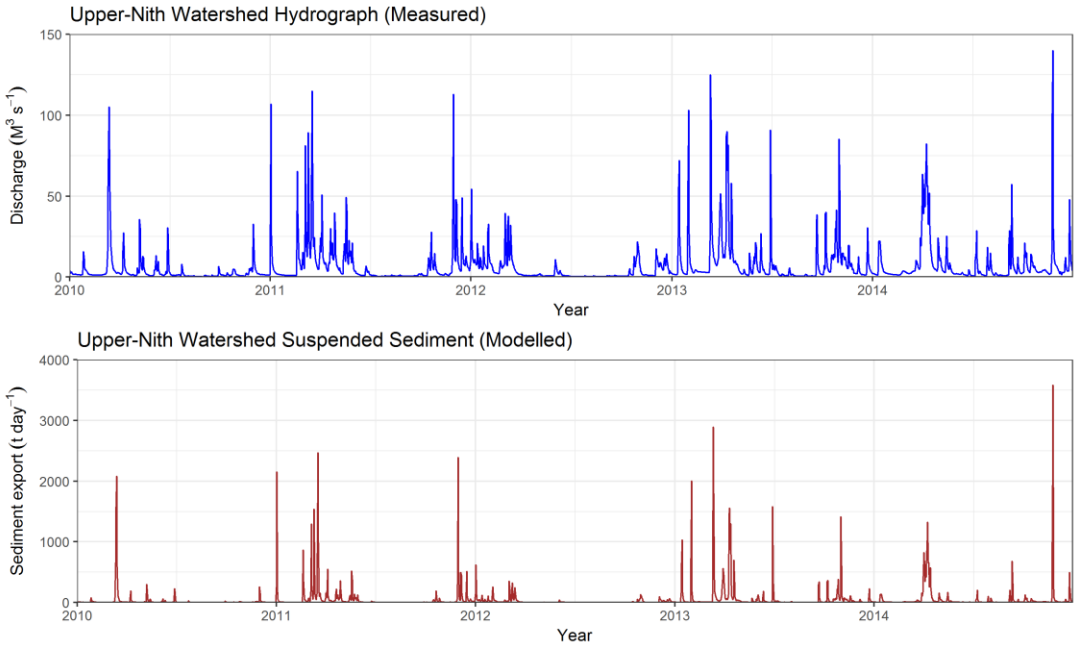

Fig. C6. Measured hydrograph and modelled sedigraph (R^2 = 0.47) at the outlet of the upper-Nith watershed. Average annual sediment yield (2010 – 2014): 19,943.07 t yr^{-1} (0.37 t ha^{-1} yr^{-1}).

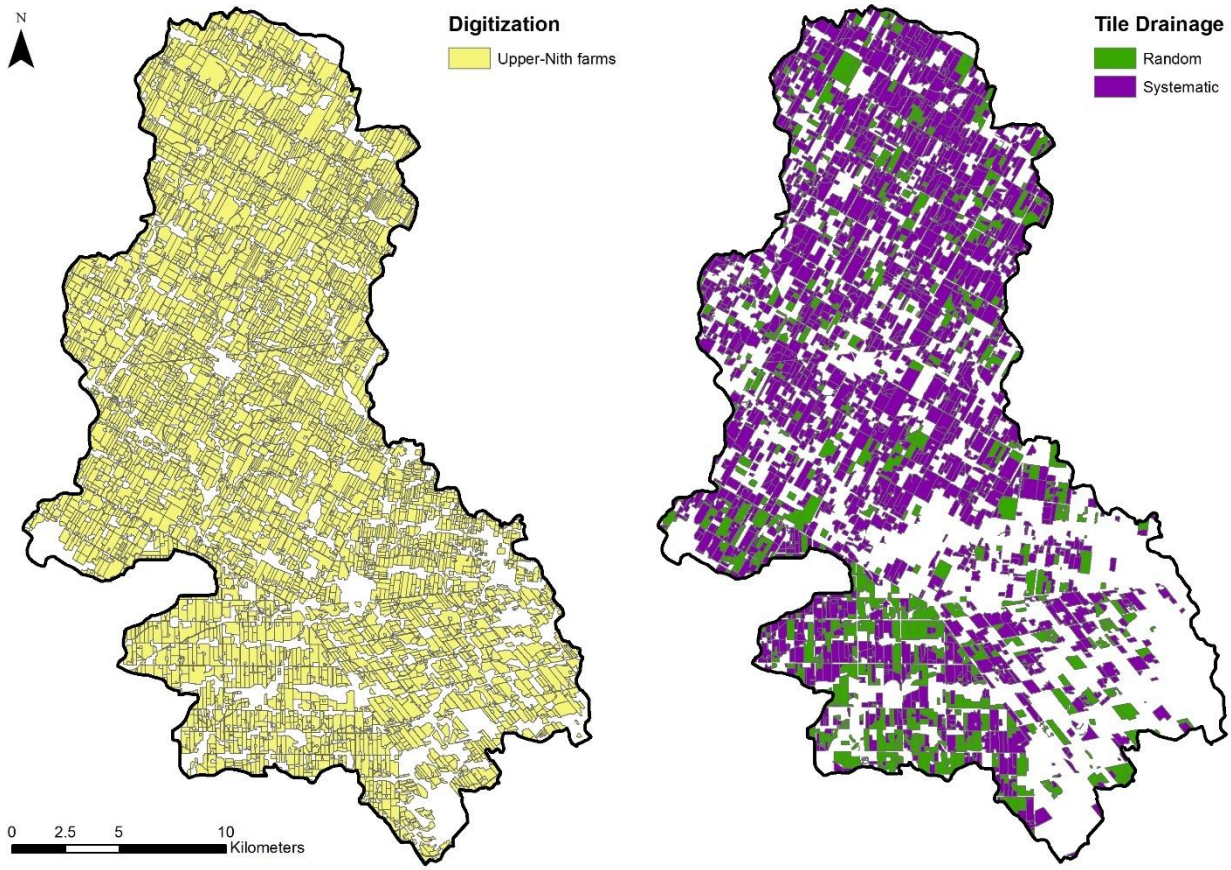

Fig. C7. Tile-drainage in the upper-Nith Watershed. Source: Ontario Ministry of Agriculture, Food, and Rural Affairs (OMAFRA) tile-drainage shapefile.